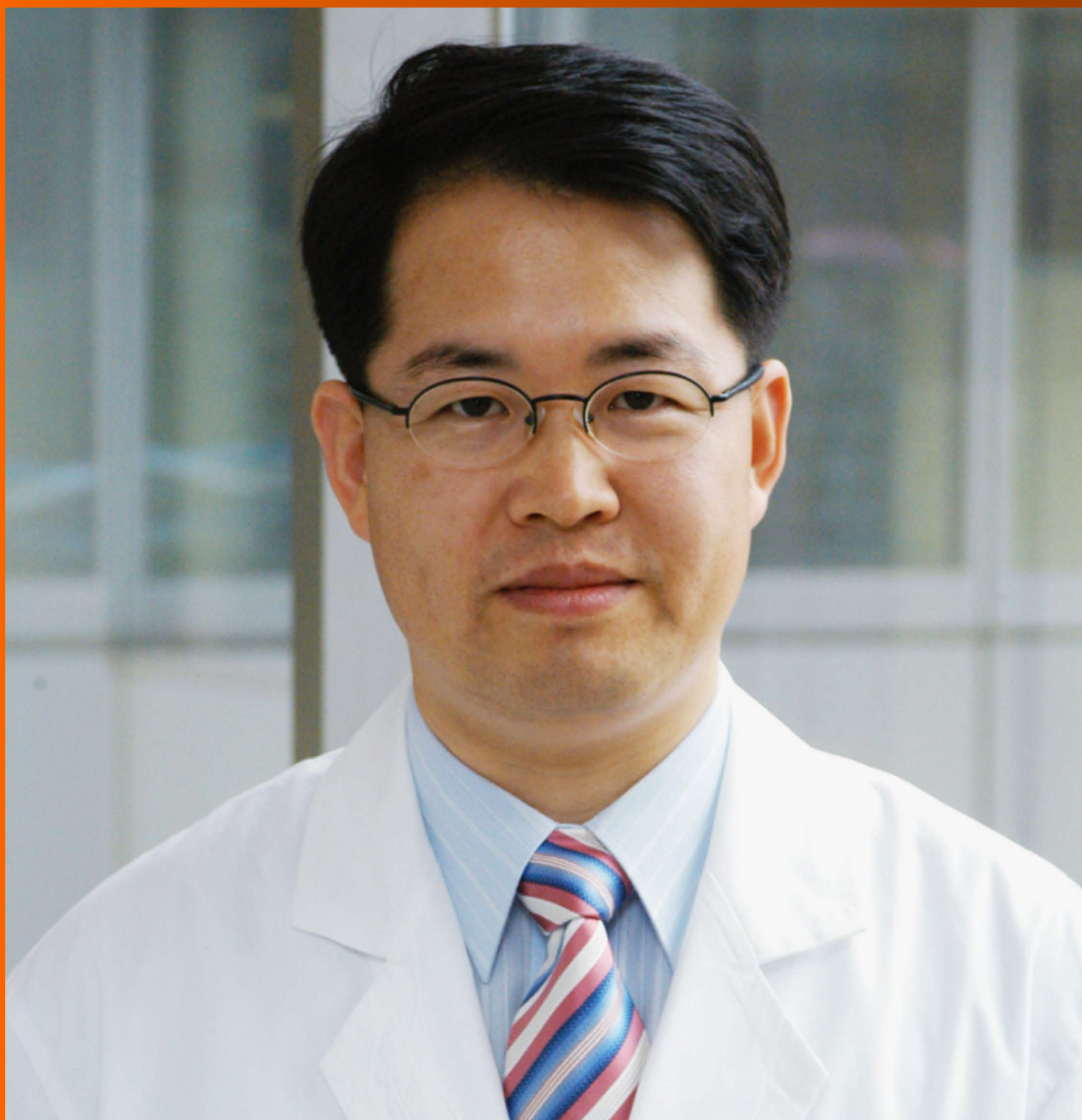


# World Journal of *Radiology*

*World J Radiol* 2016 November 28; 8(11): 851-901



## Editorial Board

2014-2017

The *World Journal of Radiology* Editorial Board consists of 365 members, representing a team of worldwide experts in radiology. They are from 36 countries, including Afghanistan (1), Argentina (2), Australia (5), Austria (7), Belgium (2), Brazil (8), Canada (6), Chile (1), China (43), Croatia (1), Denmark (4), Egypt (6), France (5), Germany (22), Greece (10), India (12), Iran (6), Ireland (2), Israel (3), Italy (47), Japan (13), Netherlands (1), New Zealand (1), Pakistan (1), Poland (2), Portugal (1), Serbia (1), Singapore (3), Slovakia (1), South Korea (18), Spain (4), Sweden (2), Switzerland (4), Thailand (1), Turkey (26), United Kingdom (11), and United States (82).

### EDITORS-IN-CHIEF

Kai U Juergens, *Bremen*  
Edwin JR van Beek, *Edinburgh*  
Thomas J Vogl, *Frankfurt*

### GUEST EDITORIAL BOARD MEMBERS

Wing P Chan, *Taipei*  
Chung-Huei Hsu, *Taipei*  
Chin-Chang Huang, *Taipei*  
Tsong-Long Hwang, *Taoyuan*  
Jung-Lung Hsu, *Taipei*  
Chia-Hung Kao, *Taichung*  
Yu-Ting Kuo, *Tainan*  
Hon-Man Liu, *Taipei*  
Hui-Lung Liang, *Kaohsiung*  
Chun Chung Lui, *Kaohsiung*  
Sen-Wen Teng, *Taipei*  
Yung-Liang (William) Wan, *Taoyuan*

### MEMBERS OF THE EDITORIAL BOARD



#### Afghanistan

Takao Hiraki, *Okayama*



#### Argentina

Patricia Carrascosa, *Vicente Lopez*  
Maria C Ziadi, *Rosario*



#### Australia

Lourens Bester, *Sydney*  
Gemma A Figtree, *Sydney*



#### Austria

Herwig R Cerwenka, *Graz*  
Gudrun M Feuchtnner, *Innsbruck*  
Benjamin Henninger, *Innsbruck*  
Rupert Lanzenberger, *Vienna*  
Shu-Ren Li, *Vienna*  
Veronika Schopf, *Vienna*  
Tobias De Zordo, *Innsbruck*



#### Belgium

Steve Majerus, *Liege*  
Kathelijne Peremans, *Merelbeke*



#### Brazil

Clerio F Azevedo, *Rio de Janeiro*  
Patrícia P Alfredo, *São Paulo*  
Eduardo FC Fleury, *São Paulo*  
Edward Araujo Júnior, *São Paulo*  
Wellington P Martins, *Ribeirao Preto*  
Ricardo A Mesquita, *Belo Horizonte*  
Vera MC Salemi, *São Paulo*  
Claudia Szobot, *Porto Alegre*  
Lilian YI Yamaga, *São Paulo*



#### Canada

Marie Arsalidou, *Toronto*  
Otman A Basir, *Waterloo*

Tarik Zine Belhocine, *Toronto*  
James Chow, *Toronto*  
Tae K Kim, *Toronto*  
Anastasia Oikonomou, *Toronto*



#### China

Hong-Wei Chen, *Wuxi*  
Feng Chen, *Hangzhou*  
Jian-Ping Chu, *Guangzhou*  
Guo-Guang Fan, *Shenyang*  
Bu-Lang Gao, *Shijiazhuang*  
Qi-Yong Gong, *Chengdu*  
Ying Han, *Beijing*  
Xian-Li Lv, *Beijing*  
Yi-Zhuo Li, *Guangzhou*  
Xiang-Xi Meng, *Harbin*  
Yun Peng, *Beijing*  
Jun Shen, *Guangzhou*  
Ze-Zhou Song, *Hangzhou*  
Wai Kwong Tang, *Hong Kong*  
Gang-Hua Tang, *Guangzhou*  
Jie Tian, *Beijing*  
Lu-Hua Wang, *Beijing*  
Xiao-bing Wang, *Xi'an*  
Yi-Gen Wu, *Nanjing*  
Kai Wu, *Guangzhou*  
Hui-Xiong Xu, *Shanghai*  
Zuo-Zhang Yang, *Kunming*  
Xiao-Dan Ye, *Shanghai*  
David T Yew, *Hong Kong*  
Ting-He Yu, *Chongqing*  
Zheng Yuan, *Shanghai*  
Min-Ming Zhang, *Hangzhou*  
Yudong Zhang, *Nanjing*  
Dong Zhang, *Chongqing*  
Wen-Bin Zeng, *Changsha*

Yue-Qi Zhu, *Shanghai*



**Croatia**

Goran Kusec, *Osijek*



**Denmark**

Poul E Andersen, *Odense*  
Lars J Petersen, *Aalborg*  
Thomas Z Ramsøy, *Frederiksberg*  
Morten Ziebell, *Copenhagen*



**Egypt**

Mohamed F Bazeed, *Mansoura*  
Mohamed Abou El-Ghar, *Mansoura*  
Reem HA Mohamed, *Cairo*  
Mohamed R Nouh, *Alexandria*  
Ahmed AKA Razek, *Mansoura*  
Ashraf A Zytoon, *Shebin El-Koom*



**France**

Sabine F Bensamoun, *Compiègne*  
Romaric Loffroy, *Dijon*  
Stephanie Nougaret, *Montpellier*  
Hassane Oudadesse, *Rennes*  
Vincent Vinh-Hung, *Fort-de-France*



**Germany**

Henryk Barthel, *Leipzig*  
Peter Bannas, *Hamburg*  
Martin Beeres, *Frankfurt*  
Ilja F Ciernik, *Dessau*  
A Dimitrakopoulou-Strauss, *Heidelberg*  
Peter A Fasching, *Erlangen*  
Andreas G Schreyer, *Regensburg*  
Philipp Heusch, *Duesseldorf*  
Sonja M Kirchhoff, *Munich*  
Sebastian Ley, *Munich*  
Adel Maataoui, *Frankfurt am Main*  
Stephan M Meckel, *Freiburg*  
Hans W Muller, *Duesseldorf*  
Kay Raum, *Berlin*  
Dirk Rades, *Luebeck*  
Marc-Ulrich Regier, *Hamburg*  
Alexey Surov, *Halle*  
Martin Walter, *Magdeburg*  
Axel Wetter, *Essen*  
Christoph Zilkens, *Düsseldorf*



**Greece**

Panagiotis Antoniou, *Thessaloniki*  
Nikos Efthimiou, *Athens*  
Dimitris Karnabatidis, *Patras*  
George Latsios, *Athens*  
Stylianios Megremis, *Iraklion*

Alexander D Rapidis, *Athens*  
Kiki Theodorou, *Larissa*  
Ioannis A Tsalafoutas, *Athens*  
Evanthia E Tripoliti, *Ioannina*  
Athina C Tsili, *Ioannina*



**India**

Ritesh Agarwal, *Chandigarh*  
Chandan J Das, *New Delhi*  
Prathamesh V Joshi, *Mumbai*  
Naveen Kalra, *Chandigarh*  
Chandrasekharan Kesavadas, *Trivandrum*  
Jyoti Kumar, *New Delhi*  
Atin Kumar, *New Delhi*  
Kaushala P Mishra, *Allahabad*  
Daya N Sharma, *New Delhi*  
Binit Sureka, *New Delhi*  
Sanjay Sharma, *New Delhi*  
Raja R Yadav, *Allahabad*



**Iran**

Majid Assadi, *Bushehr*  
SeyedReza Najafizadeh, *Tehran*  
Mohammad Ali Oghabian, *Tehran*  
Amir Reza Radmard, *Tehran*  
Ramin Sadeghi, *Mashhad*  
Hadi Rokni Yazdi, *Tehran*



**Ireland**

Tadhg Gleeson, *Wexford*  
Frederik JAI Vernimmen, *Cork*



**Israel**

Dafna Ben Bashat, *Tel Aviv*  
Amit Gefen, *Tel Aviv*  
Tamar Sella, *Jerusalem*



**Italy**

Adriano Alippi, *Rome*  
Dante Amelio, *Trento*  
Michele Anzidei, *Rome*  
Filippo F Angileri, *Messinas*  
Stefano Arcangeli, *Rome*  
Roberto Azzoni, *San Donato milanese*  
Tommaso V Bartolotta, *Palermo*  
Tommaso Bartalena, *Imola*  
Livia Bernardin, *San Bonifacio*  
Federico Boschi, *Verona*  
Sergio Casciaro, *Lecce*  
Emanuele Casciani, *Rome*  
Musa M Can, *Napoli*  
Alberto Cuocolo, *Napoli*  
Michele Ferrara, *Coppito*  
Mauro Feola, *Fossano*  
Giampiero Francica, *Castel Volturno*  
Luigi De Gennaro, *Rome*  
Giulio Giovannetti, *Pisa*

Francesca Iacobellis, *Napoli*  
Formato Invernizzi, *Monza Brianza*  
Francesco Lassandro, *Naples*  
Lorenzo Livi, *Florence*  
Pier P Mainenti, *Napoli*  
Laura Marzetti, *Chieti*  
Giuseppe Malinverni, *Crescentino*  
Enrica Milanese, *Turin*  
Giovanni Morana, *Treviso*  
Lorenzo Monti, *Milan*  
Silvia D Morbelli, *Genoa*  
Barbara Palumbo, *Perugia*  
Cecilia Parazzini, *Milan*  
Stefano Pergolizzi, *Messina*  
Antonio Pinto, *Naples*  
Camillo Porcaro, *Rome*  
Carlo C Quattrocchi, *Rome*  
Alberto Rebonato, *Perugia*  
Giuseppe Rizzo, *Rome*  
Roberto De Rosa, *Naples*  
Domenico Rubello, *Rovigo*  
Andrea Salvati, *Bari*  
Sergio Sartori, *Ferrara*  
Luca M Sconfienza, *Milano*  
Giovanni Storto, *Rionero*  
Nicola Sverzellati, *Parma*  
Alberto S Tagliafico, *Genova*  
Nicola Troisi, *Florence*



**Japan**

Yasuhiko Hori, *Chiba*  
Hidetoshi Ikeda, *Koriyama*  
Masahito Kawabori, *Sapporo*  
Tamotsu Kamishima, *Sapporo*  
Hiro Kiyosue, *Yufu*  
Yasunori Minami, *Osaka-sayama*  
Yasuhiro Morimoto, *Kitakyushu*  
Satoru Murata, *Tokyo*  
Shigeki Nagamachi, *Miyazaki*  
Hiroshi Onishi, *Yamanashi*  
Morio Sato, *Wakayama Shi*  
Yoshito Tsushima, *Maebashi*  
Masahiro Yanagawa, *Suita*



**Netherlands**

Willem Jan van Rooij, *Tilburg*



**New Zealand**

W Howell Round, *Hamilton*



**Pakistan**

Wazir Muhammad, *Abbottabad*



**Poland**

Maciej S Baglaj, *Wroclaw*

Piotr Czauderna, *Gdansk*



**Portugal**

Joao Manuel RS Tavares, *Porto*



**Serbia**

Olivera Ciraj-Bjelac, *Belgrade*



**Singapore**

Gopinathan Anil, *Singapore*  
Terence KB Teo, *Singapore*  
Cher Heng Tan, *Singapore*



**Slovakia**

Stefan Sivak, *Martin*



**South Korea**

Ki Seok Choo, *Busan*  
Seung Hong Choi, *Seoul*  
Dae-Seob Choi, *Jinju*  
Hong-Seok Jang, *Seoul*  
Yong Jeong, *Daejeon*  
Chan Kyo Kim, *Seoul*  
Se Hyung Kim, *Seoul*  
Joong-Seok Kim, *Seoul*  
Sang Eun Kim, *Seongnam*  
Sung Joon Kwon, *Seoul*  
Jeong Min Lee, *Seoul*  
In Sook Lee, *Busan*  
Noh Park, *Goyang*  
Chang Min Park, *Seoul*  
Sung Bin Park, *Seoul*  
Deuk Jae Sung, *Seoul*  
Choongsoo Shin, *Seoul*  
Kwon-Ha Yoon, *Iksan*



**Spain**

Miguel A De Gregorio, *Zaragoza*  
Antonio Luna, *Jaén*  
Enrique Marco de Lucas, *Santander*  
Fernando Ruiz Santiago, *Granada*



**Sweden**

Dmitry Grishenkov, *Stockholm*  
Tie-Qiang Li, *Stockholm*



**Switzerland**

Nicolau Beckmann, *Basel*  
Christian Boy, *Bern*  
Giorgio Treglia, *Bellinzona*

Stephan Ulmer, *Kiel*



**Thailand**

Sirianong Namwongprom, *Chiang Mai*



**Turkey**

Kubilay Aydin, *Istanbul*  
Ramazan Akdemir, *Sakarya*  
Serhat Avcu, *Ankara*  
Ayse Aralasmak, *Istanbul*  
Oktay Algin, *Ankara*  
Nevbahar Akcar, *Meselik*  
Bilal Battal, *Ankara*  
Zulkif Bozgeyik, *Elazig*  
Nazan Ciledag, *Aakara*  
Fuldem Y Donmez, *Ankara*  
Gulgun Engin, *Istanbul*  
Ahmet Y Goktay, *Izmir*  
Oguzhan G Gumustas, *Bursa*  
Kaan Gunduz, *Ankara*  
Pelin Ozcan Kara, *Mersin*  
Kivanc Kamburoglu, *Ankara*  
Ozgur Kilickesmez, *Istanbul*  
Furuzan Numan, *Istanbul*  
Cem Onal, *Adana*  
Ozgur Oztekin, *Izmir*  
Seda Ozbek (Boruban), *Konya*  
Selda Sarikaya, *Zonguldak*  
Figen Taser, *Kutahya*  
Baran Tokar, *Eskisehir*  
Ender Uysal, *Istanbul*  
Ensar Yekeler, *Istanbul*



**United Kingdom**

Indran Davagnanam, *London*  
M DC Valdés Hernández, *Edinburgh*  
Alan Jackson, *Manchester*  
Suneil Jain, *Belfast*  
Long R Jiao, *London*  
Miltiadis Krokidis, *Cambridge*  
Pradesh Kumar, *Liverpool*  
Peter D Kuzmich, *Derby*  
Georgios Plataniotis, *Brighton*  
Vanessa Sluming, *Liverpool*



**United States**

Garima Agrawal, *Saint Louis*  
James R Brasic, *Baltimore*  
Rajendra D Badgaiyan, *Buffalo*  
Ulas Bagci, *Bethesda*  
Anat Biegon, *Stony Brook*  
Ramon Casanova, *Winston Salem*  
Wenli Cai, *Boston*  
Zheng Chang, *Durham*  
Corey J Chakarun, *Long Beach*  
Kai Chen, *Los Angeles*  
Hyun-Soon Chong, *Chicago*  
Marco Cura, *Dallas*  
Ravi R Desai, *Bensalem*  
Delia DeBuc, *Miami*  
Carlo N De Cecco, *Charleston*

Timm-Michael L Dickfeld, *Baltimore*  
Subba R Digumarthy, *Boston*  
Huy M Do, *Stanford*  
Todd A Faasse, *Grand Rapids*  
Salomao Faintuch, *Boston*  
Girish M Fatterpekar, *New York*  
Dhakshinamoorthy Ganeshan, *Houston*  
Robert J Griffin, *Little Rock*  
Andrew J Gunn, *Boston*  
Sandeep S Hedgire, *Boston*  
Timothy J Hoffman, *Columbia*  
Mai-Lan Ho, *San Francisco*  
Juebin Huang, *Jackson*  
Abid Irshad, *Charleston*  
Matilde Inglese, *New York*  
El-Sayed H Ibrahim, *Jacksonville*  
Paul R Julsrud, *Rochester*  
Pamela T Johnson, *Baltimore*  
Ming-Hung Kao, *Tempe*  
Sunil Krishnan, *Houston*  
Richard A Komoroski, *Cincinnati*  
Sandi A Kwee, *Honolulu*  
King Kim, *Ft. Lauderdale*  
Guozheng Liu, *Worcester*  
Yiyan Liu, *Newark*  
Venkatesh Mani, *New York*  
Lian-Sheng Ma, *Pleasanton*  
Rachna Madan, *Boston*  
Zeyad A Metwalli, *Houston*  
Yilong Ma, *Manhasset*  
Hui Mao, *Atlanta*  
Feroze B Mohamed, *Philadelphia*  
Gul Moonis, *Boston*  
John L Noshier, *New Brunswick*  
Rahmi Oklu, *Boston*  
Aytekin Oto, *Chicago*  
Bishnuhari Paudyal, *Philadelphia*  
Rajul Pandya, *Youngstown*  
Chong-Xian Pan, *Sacramento*  
Jay J Pillai, *Baltimore*  
Neal Prakash, *Duarte*  
Reza Rahbar, *Boston*  
Ali S Raja, *Boston*  
Gustavo J Rodriguez, *El Paso*  
David J Sahn, *Portland*  
Steven Schild, *Scottsdale*  
Ali R Sepahdari, *Los Angeles*  
Li Shen, *Indianapolis*  
JP Sheehan, *Charlottesville*  
Atul B Shinagare, *Boston*  
Sarabjeet Singh, *Boston*  
Charles J Smith, *Columbia*  
Kenji Suzuki, *Chicago*  
Monvadi Srichai-Parsia, *Washington*  
Sree H Tirumani, *Boston*  
Hebert A Vargas, *New York*  
Sachit Verma, *Philadelphia*  
Yoichi Watanabe, *Minneapolis*  
Li Wang, *Chapel Hill*  
Carol C Wu, *Boston*  
Shoujun Xu, *Houston*  
Min Yao, *Cleveland*  
Xiaofeng Yang, *Atlanta*  
Qingbao Yu, *Albuquerque*  
Aifeng Zhang, *Chicago*  
Chao Zhou, *Bethlehem*  
Hongming Zhuang, *Philadelphia*

**EDITORIAL**

- 851 Metabolic positron emission tomography imaging of cancer: Pairing lipid metabolism with glycolysis  
*Kwee SA, Lim J*

**REVIEW**

- 857 Diffusion-weighted imaging of the liver: Current applications  
*Saito K, Tajima Y, Harada TL*

**MINIREVIEWS**

- 868 Sonoelastography in the musculoskeletal system: Current role and future directions  
*Winn N, Lalam R, Cassar-Pullicino V*
- 880 Mechanisms underlying <sup>18</sup>F-fluorodeoxyglucose accumulation in colorectal cancer  
*Kawada K, Iwamoto M, Sakai Y*

**ORIGINAL ARTICLE****Retrospective Study**

- 887 CO<sub>2</sub>BOLD assessment of moyamoya syndrome: Validation with single photon emission computed tomography and positron emission tomography imaging  
*Pellaton A, Bijlenga P, Bouchez L, Cuvinciuc V, Barnaure I, Garibotto V, Lövblad KO, Haller S*
- 895 Radiological imaging findings of scheuermann disease  
*Gokce E, Beyhan M*

**ABOUT COVER**

Editorial Board Member of *World Journal of Radiology*, Chan Kyo Kim, MD, PhD, Assistant Professor, Department of Radiology, Samsung Medical Center, Sungkyunkwan University School of Medicine, Gangnam-gu Seoul 135-710, South Korea

**AIM AND SCOPE**

*World Journal of Radiology* (*World J Radiol*, *WJR*, online ISSN 1949-8470, DOI: 10.4329) is a peer-reviewed open access academic journal that aims to guide clinical practice and improve diagnostic and therapeutic skills of clinicians.

*WJR* covers topics concerning diagnostic radiology, radiation oncology, radiologic physics, neuroradiology, nuclear radiology, pediatric radiology, vascular/interventional radiology, medical imaging achieved by various modalities and related methods analysis. The current columns of *WJR* include editorial, frontier, diagnostic advances, therapeutics advances, field of vision, mini-reviews, review, topic highlight, medical ethics, original articles, case report, clinical case conference (clinicopathological conference), and autobiography.

We encourage authors to submit their manuscripts to *WJR*. We will give priority to manuscripts that are supported by major national and international foundations and those that are of great basic and clinical significance.

**INDEXING/ABSTRACTING**

*World Journal of Radiology* is now indexed in PubMed, PubMed Central.

**FLYLEAF**

I-III Editorial Board

**EDITORS FOR THIS ISSUE**

Responsible Assistant Editor: *Xiang Li*  
Responsible Electronic Editor: *Ya-Jing Lu*  
Proofing Editor-in-Chief: *Lian-Sheng Ma*

Responsible Science Editor: *Fang-Fang Ji*  
Proofing Editorial Office Director: *Xiu-Xia Song*

NAME OF JOURNAL  
*World Journal of Radiology*

ISSN  
ISSN 1949-8470 (online)

LAUNCH DATE  
January 31, 2009

FREQUENCY  
Monthly

EDITORS-IN-CHIEF  
**Kai U Juergens, MD, Associate Professor**, MRT und PET/CT, Nuklearmedizin Bremen Mitte, ZEMODI - Zentrum für morphologische und molekulare Diagnostik, Bremen 28177, Germany

**Edwin JR van Beek, MD, PhD, Professor**, Clinical Research Imaging Centre and Department of Medical Radiology, University of Edinburgh, Edinburgh EH16 4TJ, United Kingdom

**Thomas J Vogl, MD, Professor, Reader in Health Technology Assessment**, Department of Diagnostic and Interventional Radiology, Johann Wolfgang Goethe University of Frankfurt, Frankfurt 60590,

Germany

EDITORIAL BOARD MEMBERS  
All editorial board members resources online at <http://www.wjnet.com/1949-8470/editorialboard.htm>

EDITORIAL OFFICE  
Xiu-Xia Song, Director  
Fang-Fang Ji, Vice Director  
*World Journal of Radiology*  
Baishideng Publishing Group Inc  
8226 Regency Drive, Pleasanton, CA 94588, USA  
Telephone: +1-925-2238242  
Fax: +1-925-2238243  
E-mail: [editorialoffice@wjnet.com](mailto:editorialoffice@wjnet.com)  
Help Desk: <http://www.wjnet.com/esps/helpdesk.aspx>  
<http://www.wjnet.com>

PUBLISHER  
Baishideng Publishing Group Inc  
8226 Regency Drive,  
Pleasanton, CA 94588, USA  
Telephone: +1-925-2238242  
Fax: +1-925-2238243  
E-mail: [bpgoffice@wjnet.com](mailto:bpgoffice@wjnet.com)  
Help Desk: <http://www.wjnet.com/esps/helpdesk.aspx>  
<http://www.wjnet.com>

PUBLICATION DATE  
November 28, 2016

COPYRIGHT  
© 2016 Baishideng Publishing Group Inc. Articles published by this Open-Access journal are distributed under the terms of the Creative Commons Attribution Non-commercial License, which permits use, distribution, and reproduction in any medium, provided the original work is properly cited, the use is non commercial and is otherwise in compliance with the license.

SPECIAL STATEMENT  
All articles published in journals owned by the Baishideng Publishing Group (BPG) represent the views and opinions of their authors, and not the views, opinions or policies of the BPG, except where otherwise explicitly indicated.

INSTRUCTIONS TO AUTHORS  
<http://www.wjnet.com/bpg/gerinfo/204>

ONLINE SUBMISSION  
<http://www.wjnet.com/esps/>

## Metabolic positron emission tomography imaging of cancer: Pairing lipid metabolism with glycolysis

Sandi A Kwee, John Lim

Sandi A Kwee, John A. Burns School of Medicine, University of Hawaii at Manoa, Honolulu, HI 96822, United States

Sandi A Kwee, John Lim, Hamamatsu/Queen's PET Imaging Center, the Queen's Medical Center, Honolulu, HI 96813, United States

**Author contributions:** Kwee SA and Lim J contributed to conception, data gathering, analysis, writing, and final approval of the manuscript.

**Conflict-of-interest statement:** The authors declare that they have no conflicts of interest.

**Open-Access:** This article is an open-access article which was selected by an in-house editor and fully peer-reviewed by external reviewers. It is distributed in accordance with the Creative Commons Attribution Non Commercial (CC BY-NC 4.0) license, which permits others to distribute, remix, adapt, build upon this work non-commercially, and license their derivative works on different terms, provided the original work is properly cited and the use is non-commercial. See: <http://creativecommons.org/licenses/by-nc/4.0/>

**Manuscript source:** Invited manuscript

**Correspondence to:** Sandi A Kwee, MD, PhD, Hamamatsu/Queen's PET Imaging Center, the Queen's Medical Center, 1301 Punchbowl St., Honolulu, HI 96813, United States. [kwee@hawaii.edu](mailto:kwee@hawaii.edu)  
Telephone: +1-808-6915466  
Fax: +1-808-6917813

Received: August 18, 2016  
Peer-review started: August 22, 2016  
First decision: September 6, 2016  
Revised: September 20, 2016  
Accepted: October 17, 2016  
Article in press: October 18, 2016  
Published online: November 28, 2016

### Abstract

The limitations of fluorine-18 fluorodeoxy-D-glucose (FDG)

in detecting some cancers has prompted a longstanding search for other positron emission tomography (PET) tracers to complement the imaging of glycolysis in oncology, with much attention paid to lipogenesis based on observations that the production of various lipid and lipid-containing compounds is increased in most cancers. Radiolabeled analogs of choline and acetate have now been used as oncologic PET probes for over a decade, showing convincingly improved detection sensitivity over FDG for certain cancers. However, neither choline nor acetate have been thoroughly validated as lipogenic biomarkers, and while acetyl-CoA produced from acetate is used in de-novo lipogenesis to synthesize fatty acids, acetate is also consumed by various other synthetic and metabolic pathways, with recent experimental observations challenging the assumption that lipogenesis is its predominant role in all cancers. Since tumors detected by acetate PET are also frequently detected by choline PET, imaging of choline metabolism might serve as an alternative albeit indirect marker of lipogenesis, particularly if the fatty acids produced in cancer cells are mainly destined for membrane synthesis through incorporation into phosphatidylcholines. Aerobic glycolysis may or may not coincide with changes in lipid metabolism, resulting in combinatorial metabolic phenotypes that may have different prognostic or therapeutic implications. Consequently, PET imaging using dual metabolic tracers, in addition to being diagnostically superior to imaging with individual tracers, could eventually play a greater role in supporting precision medicine, as efforts to develop small-molecule metabolic pathway inhibitors are coming to fruition. To prepare for this advent, clinical and translational studies of metabolic PET tracers must go beyond simply estimating tracer diagnostic utility, and aim to uncover potential therapeutic avenues associated with these metabolic alterations.

**Key words:** Glycolysis; Lipogenesis; Fatty acid metabolism; Positron emission tomography; Choline; Acetate; Cancer; Prostate cancer; Hepatocellular carcinoma

© The Author(s) 2016. Published by Baishideng Publishing

Group Inc. All rights reserved.

**Core tip:** Positron emission tomography (PET) imaging using multiple distinct metabolic tracers could eventually play a greater role in supporting precision medicine as efforts to develop small-molecule metabolic pathway inhibitors are coming to fruition. To prepare for this advent, clinical and translational studies of metabolic PET tracers must go beyond simply estimating tracer diagnostic utility, and aim to uncover potential therapeutic avenues associated with metabolic alterations in cancer.

Kwee SA, Lim J. Metabolic positron emission tomography imaging of cancer: Pairing lipid metabolism with glycolysis. *World J Radiol* 2016; 8(11): 851-856 Available from: URL: <http://www.wjgnet.com/1949-8470/full/v8/i11/851.htm> DOI: <http://dx.doi.org/10.4329/wjr.v8.i11.851>

## INTRODUCTION

The clinical success of positron emission tomography (PET) can be attributed largely to the broad and robust diagnostic utility of the imaging radiopharmaceutical fluorine-18 fluorodeoxy-D-glucose (FDG). In oncology, FDG PET/CT has no less than revolutionized cancer diagnosis, staging, and assessment of inter-treatment response<sup>[1]</sup>. As a fluorinated analog of glucose, FDG behaves as a terminal substrate for hexokinase (HK), the initiating enzyme of glycolysis. The observation that glycolytic metabolism is frequently activated in malignant tumors under conditions otherwise suitable for oxidative metabolism, a phenomenon known as the Warburg effect<sup>[1]</sup>, forms the primary rationale for imaging cancer with FDG. However, aerobic glycolysis is not a universal feature of all malignancies, and low FDG avidity may predominate in common malignancies such as hepatocellular carcinoma (HCC) and prostate cancer, with rates for detecting the primary tumor with FDG PET/CT falling as low as 55% and 4%, respectively<sup>[2,3]</sup>.

Because FDG has these limitations, there is demand for other PET tracers to complement the imaging of glycolysis in oncology, with a significant amount of attention paid to lipogenesis given that lipid-related pathways are also frequently upregulated in cancer<sup>[4]</sup>. Radiolabeled acetate and choline are two prototypes for imaging lipid synthesis using small molecule PET radiopharmaceuticals. Labeled with carbon-11, both have shown clinical utility for detecting tumors elusive to detection with FDG<sup>[5-7]</sup>. Fluorine-18 labeled analogs of choline and acetate have also been developed in an attempt to take clinical advantage of a longer-lived positron-emitting isotope label. However, while fluorine-18 labeled choline analogs have proven useful as biomarkers of choline metabolism<sup>[8,9]</sup>, <sup>18</sup>F-fluoroacetate does not appear to behave as a functional analog of acetate for the purpose of cancer imaging<sup>[10]</sup>. A list of published clinical studies involving 15 or more patients comparing radiolabeled choline and/or acetate to FDG for

specific cancer applications is shown in Table 1.

## METABOLIC PATHWAYS COMBINE TO SUPPORT MEMBRANE SYNTHESIS

At face value, acetate metabolism may be viewed as a more direct biomarker of *de-novo* lipogenesis compared to choline metabolism. The authentic tracer <sup>11</sup>C-acetate is a substrate for acetyl CoA synthetase to produce acetyl-CoA which is then carboxylated to form malonyl-CoA as the first committed step in *de-novo* lipogenesis mediated by fatty acid synthase (FAS). Upregulated FAS expression is a frequently observed phenomenon in many tumor types<sup>[4]</sup>. However, while the constitutive role of FAS in liver and adipose tissue is to create stored energy in the form of triglycerides, the primary role for FAS in cancer cells appears to be to supply fatty acids for phospholipid membrane synthesis<sup>[11,12]</sup>. Glycolysis, which is also frequently upregulated in cancer<sup>[1]</sup>, can not only fuel this process by providing ATP, but also contribute substrate for *de-novo* lipogenesis by producing acetyl-CoA. This underscores a close biochemical relationship between lipogenesis, phospholipid synthesis, and glycolysis, as illustrated in Figure 1, with fatty acids produced by FAS undergoing esterification with glycerol to produce diglycerides which then react with CDP-choline to produce phosphatidylcholine (PtC) for cell membrane synthesis ostensibly in support of tumor cell proliferation.

## IMAGING PHOSPHOLIPID SYNTHESIS WITH CHOLINE

PtC is composed of a glycerol backbone esterified with two fatty acids and phosphocholine. PtC structurally resembles triglycerides, which are composed of a glycerol backbone esterified to three fatty acids (Figure 2). The major synthetic route for PtC in most cells follows the Kennedy pathway, starting with the production of phosphocholine by choline kinase (CK). The activity of CK is upregulated in many types of cancer<sup>[13]</sup>, to the point that increased choline metabolism has been considered a metabolic hallmark of cancer<sup>[14]</sup>.

While there are subtle biochemical differences between carbon-11 and fluorine-18 labeled cholines, both are avid substrates for CK<sup>[15]</sup>. On the basis of this mechanism, fluorine-18 fluorocholine PET/CT was tested in HCC, and found to be significantly more sensitive than FDG PET/CT, with a sensitivity of 84% vs 67%, respectively ( $P = 0.01$ )<sup>[16]</sup>. As the most abundant membrane phospholipid, PtC is believed to be the primary metabolic destination of most fatty acids synthesized *de-novo* by cancer cells<sup>[11,12]</sup>. Fatty acids produced by FAS may be distinguished by their relatively high saturation, and while humans lack the desaturase enzymes required to produce certain unsaturated fatty acids (*i.e.*, essential fatty acids), *de-novo* synthesized fatty acids undergo sufficient modification by elongase and desaturase enzymes to still give rise to broad structural and functional variations among phospholipids

**Table 1** Results of PubMed query for clinical studies comparing <sup>11</sup>C-choline, fluorocholine, or <sup>11</sup>C-acetate over fluorodeoxy-D-glucose in 15 or more patients

Disease	Clinical role	First author	Publish year	No. of patients	Tracer(s) compared to FDG	Primary results
Prostate cancer	Diagnosis	Liu	2016	Meta-analysis 56 trials 3586 patients	<sup>11</sup> C-choline <sup>18</sup> F-choline, <sup>11</sup> C-acetate	<sup>18</sup> F-choline AUC 0.94, 95%CI: 0.92-0.96; <sup>11</sup> C-choline AUC 0.89, 95%CI: 0.86-0.91; <sup>11</sup> C-acetate AUC 0.78, 95%CI: 0.74-0.81; FDG AUC 0.73, 95%CI: 0.69-0.77
	Detection	Wata-nabe	2010	43	<sup>11</sup> C-choline	Sensitivity 73%, 88%, and 31% for <sup>11</sup> C-choline, MRI, and FDG, respectively
Hepato-cellular carcinoma	Re-staging	Richter	2010	73	<sup>11</sup> C-choline	Sensitivity was 60.6% for <sup>11</sup> C-choline and 31% for FDG
	Detection, metastatic	Ho	2007	121	<sup>11</sup> C-acetate	Patient-based sensitivity for metastasis was 64% and 79% for <sup>11</sup> C-cetate and FDG, respectively
	Detection, primary	Ho	2003	57	<sup>11</sup> C-acetate	Sensitivity was 87% and 47% for <sup>11</sup> C-acetate and FDG respectively
	Detection, primary/metastatic	Park	2008	112	<sup>11</sup> C-acetate	Sensitivity was 75%, 61%, and 83% for <sup>11</sup> C-acetate, FDG, and dual-tracer PET,CT, respectively
	Detection, primary	Larsson	2012	44	<sup>11</sup> C-acetate	Detection rate was 34/44 for <sup>11</sup> C-acetate and 13/44 for FDG ( <i>P</i> < 0.001)
Malignant glioma	Detection, primary	Talbot	2010	81	<sup>18</sup> F-choline	Sensitivity was 88% for <sup>18</sup> F-choline <i>vs</i> 68% for FDG
	Detection, primary	Wu	2011	76	<sup>11</sup> C-choline	<sup>11</sup> C-choline PET was positive in 28 patients with negative FDG PET
	Diagnosis	Castilla-Lievre	2016	28	<sup>11</sup> C-choline	Sensitivity was 75%, 36%, and 93% for <sup>11</sup> C-holine, FDG, and dual tracers, respectively
Nasopha-ryngeal cancer	Diagnosis	Yama-moto	2008	15	<sup>11</sup> C-acetate, <sup>11</sup> C-methi-onine	Sensitivity was 90%, 100%, and 40% for <sup>11</sup> C-acetate, <sup>11</sup> C-methionine, and FDG, respectively
	Re-staging	Tan	2011	55	<sup>11</sup> C-choline	Sensitivity/specificity was 92%/88%, 87%/81%, and 77%/63% for <sup>11</sup> C-choline, MRI, and FDG, respectively
Multiple myeloma	Staging	Wu	2011	15	<sup>11</sup> C-choline	Sensitivity for detecting locally advanced nasopharyngeal cancer was 100% <i>vs</i> 86% percent for <sup>11</sup> C-choline and FDG, respectively
	Re-staging	Lin	2014	15	<sup>11</sup> C-acetate	Diffuse infiltration was detected in 100% of patients with <sup>11</sup> C-acetate <i>vs</i> 40% with FDG
Renal cell carcinoma	Staging	Cassou-Mounat	2016	21	<sup>18</sup> F-choline	<sup>18</sup> F-fluorocholine detected 75% more lesions, and with higher intra-observer agreement than FDG (kappa score 0.89 <i>vs</i> 0.81)
	Diagnosis	Oyama	2014	29	<sup>11</sup> C-acetate	Detection rate was 72% for <sup>11</sup> C-acetate <i>vs</i> 22% for FDG

AUC: Area under the curve; CI: Confidence interval; FDG: Fluorodeoxy-D-glucose; PET: Positron emission tomography.

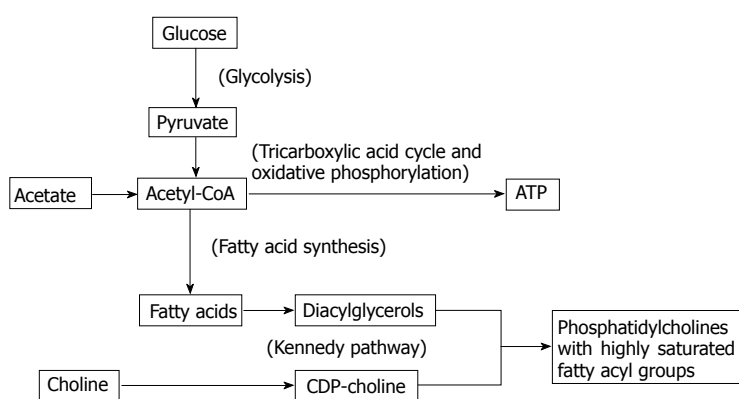


**Figure 1** The interplay between glucose, acetate, and choline metabolism. By providing substrate for *de-novo* fatty acid synthesis, acetate metabolism may feed into phosphatidylcholine synthesis, explaining why tumors showing high uptake of <sup>11</sup>C-acetate may also show increased uptake of radiolabeled choline on PET. Because acetyl-CoA produced from acetate may also serve as a substrate for the citric acid cycle and other pathways, it is possible that, for some cancers, <sup>11</sup>C-acetate uptake may not always provide a consistent readout of tumor lipogenesis. The Kennedy pathway is an ATP-dependent pathway that may rely to varying degrees on glycolysis as a source of ATP. ATP: Adenosine triphosphate.

such as phosphatidylcholine (PtC)<sup>[17]</sup>.

## DO WE NEED TO FURTHER VALIDATE IMAGING BIOMARKERS OF LIPOGENESIS?

Upregulated PtC synthesis may be coupled to lipogenesis

in cancer, since treatment by the FAS inhibitor Orlistat can reduce the activity of CK and lower PtC levels in breast, prostate, and ovarian cancer cells<sup>[18]</sup>. This and other observations support speculation that imaging of choline metabolism can be used to monitor tumor lipogenesis<sup>[12,18]</sup>. The reason why choline-based tracers may be needed to assess tumor lipogenic activity despite <sup>11</sup>C-acetate being available is that acetyl-CoA formed from acetate can also

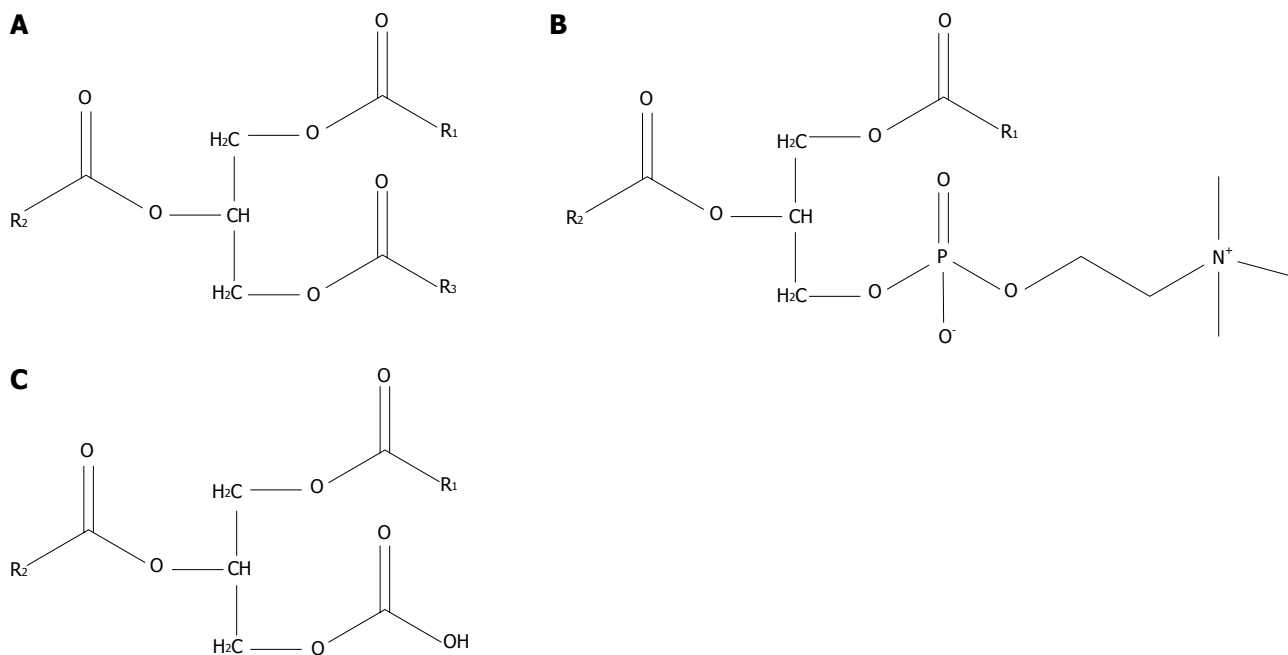


**Figure 2** Lipid molecules composed of glycerol esterified to fatty acids. Triglycerides (A), phosphatidylcholines (B), and diglycerides (C) resemble each other because of their common glycerol backbone. Molecular species of these compounds, particular phosphatidylcholines, can have broad functional variations based on the length and saturation of their fatty acyl components, R<sub>1</sub>, R<sub>2</sub>, and R<sub>3</sub>.

serve as a metabolic substrate for a variety of metabolic processes, including oxidative metabolism, histone modification, and cholesterol biosynthesis<sup>[19]</sup>. Thus, uncertainty is raised about the biochemical specificity of acetate as a PET imaging biomarker of lipogenesis. Case in point, uptake of <sup>11</sup>C-acetate by xenograft human prostate cancers was found to be correlated with FAS expression, but FAS inhibition did not completely abrogate acetate uptake, raising the possibility of acetate participating in multiple metabolic pathways<sup>[5]</sup>. Furthermore, low <sup>11</sup>C-acetate uptake has been observed in the PI3K/Met overexpressing mouse model of HCC, despite elevated expression of FAS in the tumors<sup>[19]</sup>. Therefore, acetate and choline-based tracers do need to be further validated as PET biomarkers of lipogenesis before they are deployed to the clinic for this purpose.

## EFFECT OF TUMOR DIFFERENTIATION ON METABOLIC PET IMAGING

Increases in lipid metabolism and glucose metabolism can be observed to coincide in the same tumor. Among several clinical comparisons between acetate PET and FDG PET, over 90% of poorly differentiated or metastatic HCC tumors demonstrated increased uptake of both <sup>11</sup>C-acetate and FDG, leading to the conclusion that the diagnostic advantage of acetate PET over FDG PET stems from its ability to detect more well-differentiated tumors<sup>[20-22]</sup>. In a study involving earlier stage HCC, the overall sensitivity of <sup>11</sup>C-acetate PET for all grades of tumor was 87.3%, while the sensitivity of <sup>18</sup>F-FDG was 47.3% in the same group of patients<sup>[6]</sup>. A similar pattern of dual tracer uptake in well- vs

poorly-differentiated tumors was noted in a clinical trial that compared <sup>18</sup>F-fluorocholine against FDG, with <sup>18</sup>F-fluorocholine showing higher sensitivity for well-differentiated HCC, and both tracers showing similar sensitivity for less-differentiated HCC<sup>[16]</sup>. The detection by <sup>18</sup>F-fluorocholine PET/CT of a well-differentiated HCC tumor that was not found by FDG PET is illustrated in Figure 3. Along these lines, in a tissue microarray of 157 HCC tumors, we found associations with overall survival for both CK expression and HK expression, but only HK expression correlated with tumor differentiation<sup>[23]</sup>. Thus, while choline and acetate affords PET with better overall sensitivity for HCC, only FDG PET shows promise for assessing tumor differentiation in HCC.

Biochemical insight on the relationship between choline metabolism and glycolysis can be garnered from studies involving metabolic profiling. In one pre-clinical study of ICL-CCIC-0019, a novel small molecule CK inhibitor, inhibition of choline metabolism resulted in increased glucose and acetate metabolism (without reactive oxygen species formation), ostensibly as a response to metabolic stress induced by the CK inhibitor<sup>[9]</sup>. There is also the possibility that glycolysis increases in cancer cells to sustain the metabolic demands of lipogenesis. By producing acetyl-CoA and ATP, glycolysis produces both the substrate (*i.e.*, acetyl-CoA) and energy (*i.e.*, ATP) required for *de-novo* lipogenesis. However, it does not appear that glycolysis directly drives lipogenesis, as anoxia-induced increases in glycolysis have not been shown to increase the rate of lipogenesis in cultured human breast cancer cells<sup>[24]</sup>. In cholangiocarcinoma, the second most common form of liver cancer, tumors may demonstrate high uptake on FDG PET/CT and low uptake on <sup>18</sup>F-choline PET/CT, a

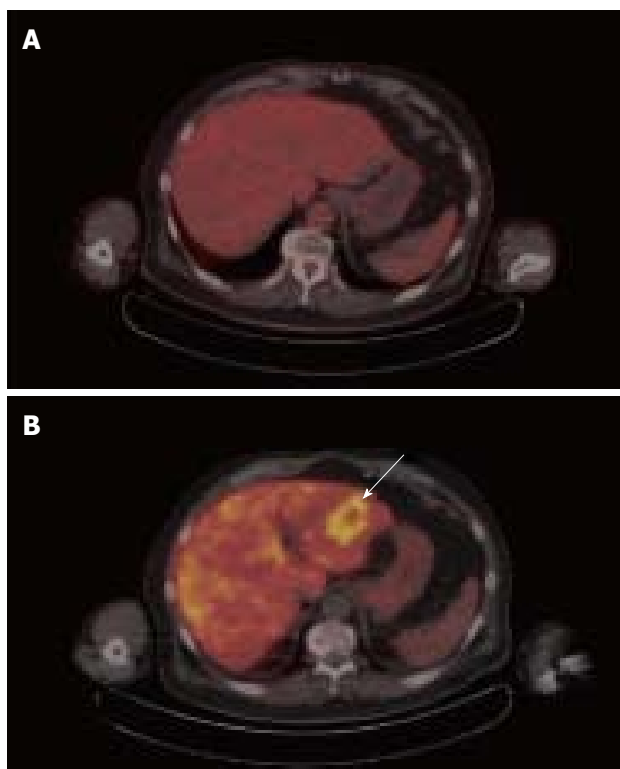


**Figure 3** Corresponding  $^{18}\text{F}$ -fluorodeoxy-D-glucose positron emission tomography/computed tomography (A) and  $^{18}\text{F}$ -fluorocholeline positron emission tomography/computed tomography (B) images of hepatocellular carcinoma obtained from the same patient on different days. The tumor is not at all evident on transaxial images of the liver from FDG PET/CT (A). Corresponding transaxial images of the liver from  $^{18}\text{F}$ -fluorocholeline PET/CT (B) shows a 5-cm diameter circumscribed area of increased uptake in the left hepatic lobe (B). This tumor contained within the left hepatic lobe was histopathologically confirmed to be a well-differentiated HCC. FDG:  $^{18}\text{F}$ -fluorodeoxy-D-glucose; PET: Positron emission tomography; CT: Computed tomography; HCC: Hepatocellular carcinoma.

metabolic phenotype that may differ from both well- and poorly-differentiated HCC<sup>[16,25]</sup>. We globally analyzed the gene expression from such tumors, predicting increased glucose transport and inhibited lipid metabolism based on a gene expression signature that distinguishes ICC from HCC<sup>[25]</sup>. Consistent with these findings, cholangiocarcinomas have also been shown to uniformly demonstrate low  $^{11}\text{C}$ -acetate uptake<sup>[6]</sup>. The application of both FDG and choline/acetate-based PET imaging in liver tumors may therefore inform on both potential metabolic vulnerabilities as well as the tumorigenic pathways driving an individual patient's cancer.

## CONCLUSION

Relationships between glycolysis, fatty acid synthesis, and choline metabolism, in terms of pathways and metabolic substrates, have been described biochemically, but this has not led to absolute clarity about what these pathways and substrates reflect as molecular imaging biomarkers in cancer. Acetate, as a precursor to acetyl-CoA, may have value as an imaging biomarker of cancer lipogenesis, however, choline biomarkers may complement or even

supplant acetate as a cancer imaging biomarker for lipogenic activity given that acetate is also a substrate for aerobic respiration and other pathways which may become abnormal in cancer. Phosphatidylcholine synthesis is reliant on *de-novo* fatty acid synthesis for its supply of diglycerides, and FAS inhibition may down-regulate CK activity and PtC production, further raising the possibility that radiolabeled cholines can indirectly serve as PET biomarkers of lipogenic activity. However, CK inhibition may cause concomitant increases in glucose and acetate metabolism, underscoring the need to further validate these metabolic PET biomarkers for specific clinical applications. With better understanding of these metabolic interactions, multi-tracer metabolic PET, in addition to affording higher sensitivity than single-tracer PET for cancer detection, is likely to provide valuable information on the metabolic vulnerabilities associated with cancer.

## REFERENCES

- Kelloff GJ**, Hoffman JM, Johnson B, Scher HI, Siegel BA, Cheng EY, Cheson BD, O'shaughnessy J, Guyton KZ, Mankoff DA, Shankar L, Larson SM, Sigman CC, Schilsky RL, Sullivan DC. Progress and promise of FDG-PET imaging for cancer patient management and oncologic drug development. *Clin Cancer Res* 2005; **11**: 2785-2808 [PMID: 15837727 DOI: 10.1158/1078-0432.CCR-04-2626]
- Khan MA**, Combs CS, Brunt EM, Lowe VJ, Wolverson MK, Solomon H, Collins BT, Di Bisceglie AM. Positron emission tomography scanning in the evaluation of hepatocellular carcinoma. *J Hepatol* 2000; **32**: 792-797 [PMID: 10845666 DOI: 10.1016/S0168-8278(00)80248-2]
- Liu IJ**, Zafar MB, Lai YH, Segall GM, Terris MK. Fluorodeoxyglucose positron emission tomography studies in diagnosis and staging of clinically organ-confined prostate cancer. *Urology* 2001; **57**: 108-111 [PMID: 11164153 DOI: 10.1016/S0090-4295(00)00896-7]
- Menendez JA**, Lupu R. Fatty acid synthase and the lipogenic phenotype in cancer pathogenesis. *Nat Rev Cancer* 2007; **7**: 763-777 [PMID: 17882277 DOI: 10.1038/nrc2222]
- Vävere AL**, Kridel SJ, Wheeler FB, Lewis JS. 1-11C-acetate as a PET radiopharmaceutical for imaging fatty acid synthase expression in prostate cancer. *J Nucl Med* 2008; **49**: 327-334 [PMID: 18199615 DOI: 10.2967/jnumed.107.046672]
- Ho CL**, Yu SC, Yeung DW. 11C-acetate PET imaging in hepatocellular carcinoma and other liver masses. *J Nucl Med* 2003; **44**: 213-221 [PMID: 12571212]
- Kwee SA**, DeGrado TR, Talbot JN, Gutman F, Coel MN. Cancer imaging with fluorine-18-labeled choline derivatives. *Semin Nucl Med* 2007; **37**: 420-428 [PMID: 17920349 DOI: 10.1053/j.semnuclmed.2007.07.003]
- Salem N**, Kuang Y, Wang F, MacLennan GT, Lee Z. PET imaging of hepatocellular carcinoma with 2-deoxy-2-[18F]fluoro-D-glucose, 6-deoxy-6-[18F] fluoro-D-glucose, [1-11C]-acetate and [N-methyl-11C]-choline. *Q J Nucl Med Mol Imaging* 2009; **53**: 144-156 [PMID: 19039303]
- Trousil S**, Kaliszczak M, Schug Z, Nguyen Q, Tomasi G, Favicchio R, Brickute D, Fortt R, Twyman FJ, Carroll L, Kalusa A, Navaratnam N, Adejumo T, Carling D, Gottlieb E, Aboagye EO. The novel choline kinase inhibitor ICL-CCIC-0019 reprograms cellular metabolism and inhibits cancer cell growth. *Oncotarget* 2016; **7**: 37103-37120 [PMID: 27206796 DOI: 10.18632/oncotarget.9466]
- Lindhe O**, Sun A, Ulin J, Rahman O, Långström B, Sörensen J. [(18F)Fluoroacetate is not a functional analogue of [(11C)acetate in normal physiology. *Eur J Nucl Med Mol Imaging* 2009; **36**: 1453-1459 [PMID: 19387639 DOI: 10.1007/s00259-009-1128-7]
- Swinnen JV**, Van Veldhoven PP, Timmermans L, De Schrijver E, Brusselmans K, Vanderhoydonc F, Van de Sande T, Heemers H, Heyns W, Verhoeven G. Fatty acid synthase drives the synthesis

- of phospholipids partitioning into detergent-resistant membrane microdomains. *Biochem Biophys Res Commun* 2003; **302**: 898-903 [PMID: 12646257 DOI: 10.1016/S0006-291X(03)00265-1]
- 12 **Salem N**, Kuang Y, Corn D, Erokwu B, Kolthammer JA, Tian H, Wu C, Wang F, Wang Y, Lee Z. [(Methyl)-<sup>11</sup>C]-acetate metabolism in hepatocellular carcinoma. *Mol Imaging Biol* 2011; **13**: 140-151 [PMID: 20401538 DOI: 10.1007/s11307-010-0308-y]
  - 13 **Ramírez de Molina A**, Rodríguez-González A, Gutiérrez R, Martínez-Piñero L, Sánchez J, Bonilla F, Rosell R, Lacal J. Overexpression of choline kinase is a frequent feature in human tumor-derived cell lines and in lung, prostate, and colorectal human cancers. *Biochem Biophys Res Commun* 2002; **296**: 580-583 [PMID: 12176020 DOI: 10.1016/S0006-291X(02)00920-8]
  - 14 **Glunde K**, Bhujwalla ZM, Ronen SM. Choline metabolism in malignant transformation. *Nat Rev Cancer* 2011; **11**: 835-848 [PMID: 22089420 DOI: 10.1038/nrc3162]
  - 15 **Bansal A**, Shuyan W, Hara T, Harris RA, Degrado TR. Biodisposition and metabolism of [(18F)]fluorocholine in 9L glioma cells and 9L glioma-bearing fisher rats. *Eur J Nucl Med Mol Imaging* 2008; **35**: 1192-1203 [PMID: 18264706 DOI: 10.1007/s00259-008-0736-y]
  - 16 **Talbot JN**, Fartoux L, Balogova S, Nataf V, Kerrou K, Gutman F, Huchet V, Ancel D, Grange JD, Rosmorduc O. Detection of hepatocellular carcinoma with PET/CT: a prospective comparison of 18F-fluorocholine and 18F-FDG in patients with cirrhosis or chronic liver disease. *J Nucl Med* 2010; **51**: 1699-1706 [PMID: 20956466 DOI: 10.2967/jnumed.110.075507]
  - 17 **Stubbs CD**, Smith AD. The modification of mammalian membrane polyunsaturated fatty acid composition in relation to membrane fluidity and function. *Biochim Biophys Acta* 1984; **779**: 89-137 [PMID: 6229284 DOI: 10.1016/0304-4157(84)90005-4]
  - 18 **Ross J**, Najjar AM, Sankaranarayananpillai M, Tong WP, Kaluarachchi K, Ronen SM. Fatty acid synthase inhibition results in a magnetic resonance-detectable drop in phosphocholine. *Mol Cancer Ther* 2008; **7**: 2556-2565 [PMID: 18723500 DOI: 10.1158/1535-7163.MCT-08-0015]
  - 19 **Li L**, Che L, Wang C, Blecha JE, Li X, VanBrocklin HF, Calvisi DF, Puchowicz M, Chen X, Seo Y. [(11C)]acetate PET Imaging is not Always Associated with Increased Lipogenesis in Hepatocellular Carcinoma in Mice. *Mol Imaging Biol* 2016; **18**: 360-367 [PMID: 26567114 DOI: 10.1007/s11307-015-0915-8]
  - 20 **Ho CL**, Chen S, Yeung DW, Cheng TK. Dual-tracer PET/CT imaging in evaluation of metastatic hepatocellular carcinoma. *J Nucl Med* 2007; **48**: 902-909 [PMID: 17504862 DOI: 10.2967/jnumed.106.036673]
  - 21 **Park JW**, Kim JH, Kim SK, Kang KW, Park KW, Choi JI, Lee WJ, Kim CM, Nam BH. A prospective evaluation of 18F-FDG and 11C-acetate PET/CT for detection of primary and metastatic hepatocellular carcinoma. *J Nucl Med* 2008; **49**: 1912-1921 [PMID: 18997056 DOI: 10.2967/jnumed.108.055087]
  - 22 **Cheung TT**, Chan SC, Ho CL, Chok KS, Chan AC, Sharr WW, Ng KK, Poon RT, Lo CM, Fan ST. Can positron emission tomography with the dual tracers [11 C]acetate and [18 F]fludeoxyglucose predict microvascular invasion in hepatocellular carcinoma? *Liver Transpl* 2011; **17**: 1218-1225 [PMID: 21688383 DOI: 10.1002/lt.22362]
  - 23 **Kwee SA**, Hernandez B, Chan O, Wong L. Choline kinase alpha and hexokinase-2 protein expression in hepatocellular carcinoma: association with survival. *PLoS One* 2012; **7**: e46591 [PMID: 23071593 DOI: 10.1371/journal.pone.0046591]
  - 24 **Hopperton KE**, Duncan RE, Bazinet RP, Archer MC. Fatty acid synthase plays a role in cancer metabolism beyond providing fatty acids for phospholipid synthesis or sustaining elevations in glycolytic activity. *Exp Cell Res* 2014; **320**: 302-310 [PMID: 24200503 DOI: 10.1016/j.yexcr.2013.10.016]
  - 25 **Kwee SA**, Okimoto GS, Chan OT, Tiirikainen M, Wong LL. Metabolic characteristics distinguishing intrahepatic cholangiocarcinoma: a negative pilot study of (18F)-fluorocholine PET/CT clarified by transcriptomic analysis. *Am J Nucl Med Mol Imaging* 2016; **6**: 73-83 [PMID: 27069767]

**P- Reviewer:** Kim SS, Rubello D, Soreide K **S- Editor:** Ji FF  
**L- Editor:** A **E- Editor:** Lu YJ



## Diffusion-weighted imaging of the liver: Current applications

Kazuhiro Saito, Yu Tajima, Taiyo L Harada

Kazuhiro Saito, Yu Tajima, Taiyo L Harada, Department of Radiology, Tokyo Medical University, Tokyo 160-0023, Japan

**Author contributions:** All authors contributed equally to this work; wrote and reviewed the paper.

**Conflict-of-interest statement:** Authors declare no conflict of interests for this article.

**Open-Access:** This article is an open-access article which was selected by an in-house editor and fully peer-reviewed by external reviewers. It is distributed in accordance with the Creative Commons Attribution Non Commercial (CC BY-NC 4.0) license, which permits others to distribute, remix, adapt, build upon this work non-commercially, and license their derivative works on different terms, provided the original work is properly cited and the use is non-commercial. See: <http://creativecommons.org/licenses/by-nc/4.0/>

**Manuscript source:** Invited manuscript

**Correspondence to:** Kazuhiro Saito, MD, Department of Radiology, Tokyo Medical University, 6-7-1 Nishishinjuku, Shinjuku-ku, Tokyo 160-0023, Japan. [saito-k@tokyo-med.ac.jp](mailto:saito-k@tokyo-med.ac.jp)  
Telephone: +81-3-33426111

Received: June 3, 2016  
Peer-review started: June 6, 2016  
First decision: July 26, 2016  
Revised: October 11, 2016  
Accepted: October 22, 2016  
Article in press: October 23, 2016  
Published online: November 28, 2016

### Abstract

Diffusion-weighted imaging (DWI) of the liver can be performed using most commercially available machines and is currently accepted in routine sequence. This sequence has some potential as an imaging biomarker for fibrosis, tumor detection/characterization, and following/predicting therapy. To improve reliability including accuracy

and reproducibility, researchers have validated this new technique in terms of image acquisition, data sampling, and analysis. The added value of DWI in contrast-enhanced magnetic resonance imaging was established in the detection of malignant liver lesions. However, some limitations remain in terms of lesion characterization and fibrosis detection. Furthermore, the methodologies of image acquisition and data analysis have been inconsistent. Therefore, researchers should make every effort to not only improve accuracy and reproducibility but also standardize imaging parameters.

**Key words:** Diffusion weighted imaging; Liver; Fibrosis; Lesion characterization

© **The Author(s) 2016.** Published by Baishideng Publishing Group Inc. All rights reserved.

**Core tip:** The current application of diffusion-weighted imaging (DWI) is reviewed. DWI has some potential as an imaging biomarker for fibrosis, tumor detection/characterization, and following/predicting therapy. However, some limitations remain in terms of lesion characterization and fibrosis detection. To improve reliability including accuracy and reproducibility, researchers have validated this new technique in terms of image acquisition, data sampling, and analysis.

Saito K, Tajima Y, Harada TL. Diffusion-weighted imaging of the liver: Current applications. *World J Radiol* 2016; 8(11): 857-867 Available from: URL: <http://www.wjgnet.com/1949-8470/full/v8/i11/857.htm> DOI: <http://dx.doi.org/10.4329/wjr.v8.i11.857>

### INTRODUCTION

Diffusion-weighted imaging (DWI) is an imaging method that allows the mapping of the free diffusion of water molecules which reflects the structural differences in

disease by restricting diffusion. DWI can be added to the routine examination easily using recently available machines. This imaging method has a good ability to detect liver lesions, and quantitative evaluation can be achieved without contrast media. Therefore, DWI does not require considerations for patients having contrast media allergy and the risk of nephrogenic systemic fibrosis due to renal dysfunction<sup>[1]</sup>.

## FUNDAMENTALS AND TECHNIQUES

### Theory

When assuming free water, water molecules spread three-dimensionally with time and temperature dependence by Brownian motion. It is represented by the Einstein-Smoluchowski formula:  $\langle r^2 \rangle = 6Dt$ ,  $D = \mu K_B T$ , where  $r$  is the average distance,  $D$  is the diffusion coefficient,  $t$  is time,  $\mu$  is mobility,  $K_B$  is Boltzmann's constant, and  $T$  is the absolute temperature. This spread follows the Gaussian distribution called free diffusion.

Stejskal and Tanner previously measured the diffusion coefficient along with their theory using a binary magnetic field gradient by the spin-echo method<sup>[2]</sup>. At present, DWI acquisition is commonly performed with a Spin-Echo echo planar imaging (EPI) sequence. Water molecule movement was impeded by the cell membrane, interstitial space, and macromolecules. The movement did not follow the Gaussian probability distribution. When  $D$  (diffusion coefficient) is small or time " $t$ " is short, the measured  $D$  is the same as that of free diffusion because water molecules rarely interact with barrier structures. On the other hand, there is a high probability of the movement being affected by a barrier structure when time " $t$ " is greater, which causes the measured  $D$  to become smaller than that of free diffusion. This state is referred to as restricted diffusion.

High cellularity, distortion of the extracellular space, and density of the hydrophobic cell membrane within the tissue restrict diffusion. In contrast, an intravoxel microvessel which travels disorderly behaves similarly to a diffusion phenomenon. As mentioned above, DWI enables not only pure diffusion but also microvessel perfusion. Therefore, the diffusion coefficient is designated comprehensively as apparent diffusion coefficient (ADC).

As the  $b$ -value increases on DWI, the signal decreases in tissues composed chiefly of large diffusion components such as free water owing to phase dispersion, and thus the contrast to tissues that restrict diffusion becomes more clear.  $b$ -value is defined by the following equation<sup>[2]</sup>:  $b \text{ (s/mm}^2\text{)} = -\gamma^2 \cdot G^2 \cdot \delta^2 (\Delta - \delta/3)$ , where  $\gamma$  is the gyromagnetic ratio,  $G$  is the diffusion gradient amplitude,  $\delta$  is the gradient diffusion length, and  $\Delta$  is the diffusion time.

ADC is calculated using the following formula:  $S_b/S_0 = \exp(-b \cdot \text{ADC})$ , where  $S_b$  and  $S_0$  are the signal intensity with and without the application of the diffusion gradient, respectively. This formula is a monoexponential model which does not fit with actual measurement. This is the

reason why the signal intensity in the voxel is affected by blood microcirculation. Le Bihan *et al.*<sup>[3]</sup> have proposed the theory of intravoxel incoherent motion (IVIM). They considered blood microcirculation as rapid diffusion, and defined pure molecular diffusion coefficient ( $D$ ) and pseudodiffusion coefficient ( $D^*$ ). This biexponential model was defined using the following formula when multiple  $b$ -values are obtained, from low  $b$ -values ( $< 200 \text{ s/mm}^2$ ) to high  $b$ -values ( $> 200 \text{ s/mm}^2$ ):  $S_b/S_0 = f \times \exp[-(D^* + D) \times b] + (1 - f) \times \exp(-D \times b)$ , where  $D$  is the true diffusion coefficient,  $D^*$  is the pseudodiffusion coefficient, and  $f$  is the perfusion fraction. The IVIM model has been applied to the evaluation of liver fibrosis and tumor characterization<sup>[4,5]</sup>. However, some controversial issues about IVIM have remained. The poor reproducibility of  $D^*$  has been reported<sup>[6,7]</sup>. Selection of a fitting model is also crucial for IVIM parameters, because the choice of the  $b$ -value and reproducibility may be closely related to the fitting models<sup>[8]</sup>.

### Advance of technology

DWI using parallel imaging allows for a shorter echo time, and it facilitates improvement of the signal-to-noise (SNR) ratio and thus decreasing susceptibility to artifact<sup>[9]</sup>. Furthermore, distortion, blurring, and off-resonance artifact diminish, and this increases the spatial resolution<sup>[10]</sup>. ADC measurement using parallel imaging is reliable except for ADC measurement in the left lobe of the liver<sup>[11]</sup>. The SNR increases at a high field strength system, but there are some concerns about the inferiority of image quality owing to artifact or signal decay by  $B_0/B_1$  inhomogeneity,  $T_2/T_2^*$  shortening, and increasing acoustic gradient noise. However, using parallel imaging offsets these disadvantages<sup>[12]</sup>.

Single shot spin echo planar sequence is sensitized to not only the motion of diffusion but also bulk motion. Therefore, the consideration of respiration and pulsation is important in case of the acquisition of liver images. In image acquisition during breath holding, it is unnecessary to consider respiratory artifact, in contrast to some disadvantages such as low spatial resolution, low SNR, distortion, and ghost artifact. On the other hand, the free breathing (FB) method usually takes a few minutes because of the many acquisition times, and as a result the SNR increases. Moreover, a high spatial resolution can be achieved and thin slices can be obtained<sup>[13]</sup>. However, the disadvantage of the FB method is that it is less reliable if there is heterogeneity in the lesion owing to the averaging and blurring of the image. The navigator-triggered (NT) acquisition is a method for running the image sequence in accordance with the expiratory phase monitoring the movement of the diaphragm on high-speed imaging systems such as FLASH during FB. The NT technique improves image quality and lesion contrast, and increases SNR. Moreover, it enables accurate ADC measurement<sup>[14,15]</sup>. Artifact also becomes stronger as  $b$ -value increases<sup>[15]</sup>. In addition, a specific artifact reported as hepatic pseudoanisotropy attributed to performing DWI

in the respiratory gating (RT) has been reported<sup>[16]</sup>.

ADC was reported to be affected by SNR, susceptibility artifact, or artifact derived from heart beating or liver motion due to respiration. Although FB tends to scatter signals compared with RT, the ADC does not differ<sup>[17]</sup>. The SNR on RT is higher than that on BH. The ADC is also slightly higher on RT than on BH<sup>[14]</sup>. In a comparison between NT and FB, both are reportedly similar in terms of the ADC and IVIM parameters<sup>[18]</sup>.

For ADC reproducibility, RT is superior to BH but inferior to FB in healthy liver parenchyma<sup>[19]</sup>. Similarly, in a comparison study among multiple breath-hold (MBH), FB, RT, and NT, FB showed the best ADC reproducibility<sup>[20]</sup>. It should be noted that there were differences in the signal acquisition times among those techniques in these comparison studies<sup>[20]</sup>.

### **Effects of contrast agent administration**

Currently, Gd-EOB-DTPA-enhanced MRI has been widely used for the detection of liver lesions. However, it is necessary to wait for about 20 min for optimal liver parenchymal enhancement<sup>[21]</sup>. To improve the examination throughput, DWI is undertaken after Gd-EOB-DTPA injection. Gd-EOB-DTPA does not have an effect on ADC<sup>[22]</sup>. Furthermore, considering the biexponential IVIM model, there were also no effects on  $D$ ,  $D^*$ , and  $PF$ <sup>[23]</sup>. Based on these facts, even if DWI is not successful prior to contrast administration, the lesion can be evaluated on the images acquired during the waiting time until the hepatobiliary phase.

### **Weak feature of DWI**

Cardiac motion causes negligible artifact (signal loss) on DWI of the liver. This artifact tends to become emphasized with a higher  $b$ -value and is closer to the heart. Thus, the artifact in the left lobe around the lower surface of the heart in particular can make an image particularly obscure<sup>[19,24]</sup>. The liver-to-background contrast is also changed by the cardiac phase of acquisition; it decreases more at the systolic phase and signal loss is larger in the left lobe<sup>[25]</sup>. The ADC of the left lobe is higher and its reproducibility is worse compared with the right lobe<sup>[26]</sup>. Some solutions to reduce the effects of cardiac motion have been proposed. These include the postprocessing method<sup>[24]</sup> or filtering<sup>[27]</sup> which corrects the image after signal acquisition or cardiac triggering synchronized with the heart cycle<sup>[27,28]</sup>. ADC reproducibility was reportedly improved using these methods.

Moreover, susceptibility artifact occurs at the boundary surfaces between the lungs and the liver parenchyma because of magnetic field inhomogeneity<sup>[29]</sup>. The artifact is observed as a signal loss in the diaphragm or liver.

Peristaltic movement can produce ghost artifact or blurring on abdominal MRI in the pancreas and liver near the intestinal tract<sup>[30]</sup>. Hyoscine butylbromide suppresses contraction of the smooth muscles in the intestines and it can reduce ghost artifact (peristaltic artifact). Moreover,

it can similarly improve the image quality<sup>[31]</sup>. As hyoscine butylbromide administration can increase the heart rate, it has also been pointed out that the image quality of the subcardiac area in the hepatic left lobe is reduced on visual evaluation. However, there is no observed significant change in ADC<sup>[32]</sup>. Thus, it is necessary to address all of the challenges associated with DWI of the liver to achieve higher levels of quantitative and qualitative outcomes and to obtain precise assessments.

## **EVALUATION OF LIVER FIBROSIS**

### **Clinical application**

Liver fibrosis is the accumulation of scar tissue resulting from hepatocyte response to chronic inflammation caused by the hepatitis B or C virus and alcohol consumption, among many other causes<sup>[33]</sup>. Chronic inflammation activates the stellate cells and induces fibrosis of the extracellular matrix (ECM). In this process, molecules such as glycogen, proteoglycan, and other macromolecules accumulate in the ECM, restricting ECM diffusion<sup>[34,35]</sup>. Fibrosis leads to cirrhosis, portal hypertension after many years, and possibly eventual death. Liver biopsy is a widely accepted procedure for diagnosing and grading liver fibrosis. However, this procedure is associated with major complications in 0.3% and with mortality in 0.018% of patients<sup>[36]</sup>. Furthermore, because of the heterogeneity of liver fibrosis, sampling errors can also arise<sup>[37,38]</sup>. Therefore, alternative noninvasive diagnostic methods that can precisely evaluate liver fibrosis are desirable. Because of convenience and repeatability, the usefulness of some diffusion-weighted MRI parameters (*e.g.*, ADC) and IVIM parameters has been evaluated in several studies. DWI enables the evaluation of restricted diffusion caused by collagen fibers accumulated in the ECM in cirrhotic liver<sup>[39-41]</sup>. In relation to this, it is important to distinguish METAVIR fibrosis stage 3 or 4 from stages 0 to 2 because patients in the F0-2 grades can be cured by treating the underlying liver disease<sup>[42]</sup>.

### **Evaluating liver fibrosis using ADC**

Several studies have shown that ADC decreases as the liver fibrosis grade progresses<sup>[40,41,43,44]</sup>. Specifically, the diagnostic performance of detecting METAVIR fibrosis grade 3 or 4 was variable and the area under the ROC curve (AUC) was 0.54-0.92. Some studies have concluded that MR elastography was more reliable than DWI<sup>[44,45]</sup>. Do *et al.*<sup>[46]</sup> proposed normalized ADC to improve the diagnostic accuracy of DWI. They calculated normalized ADC as the ratio of liver ADC to spleen ADC and reported that the AUC increased from 0.689 to 0.805 using their methods (Table 1).

### **Evaluating liver fibrosis using IVIM parameters**

The efficacy of diagnosing liver fibrosis has been reported by Luciani *et al.*<sup>[5]</sup>. They found that perfusion-related diffusion parameters ( $D^*$ : Fast component of diffusion,  $f$ : Fraction of the diffusion linked to microcirculation) were

**Table 1** Detection of fibrosis using diffusion-weighted imaging

	Tesla	Respiratory	Staging	ROI setting	<i>b</i> -value	Diagnostic accuracy of fibrosis F3 or grater		
						AUC	Sensitivity	Specificity
Cece <i>et al</i> <sup>[91]</sup>	1.5	BH	MTAVIR	5 ROIs, Both	0, 500, 1000	0.888	92.9	79.4
Taouli <i>et al</i> <sup>[92]</sup>	1.5	BH	MTAVIR	4 ROIs, Both	0, 50	0.717	40	100
					0, 300	0.716	50	94.7
					0, 500	0.835	70	85
					0, 700	0.901	66.7	100
					0, 1000	0.832	80	90
					0, 50, 300, 500, 700, 1000	0.896	88.9	80
Kocakoc <i>et al</i> <sup>[93]</sup>	1.5	BH	Ishak	3 ROIs, Both	100, 600, 1000	0.759	56.5	99.3
Wu <i>et al</i> <sup>[47]</sup>	3	RT	MTAVIR	5 ROIs, Right	0, 10, 20, 30, 40, 50, 60, 70, 80, 90,	0.684		
					100, 200, 300, 400, 500, 1000			
Chung <i>et al</i> <sup>[48]</sup>	1.5	RT	MTAVIR	6 ROIs, Right	0, 100, 200, 900	0.768	65.5	82.1
					0, 30, 60, 100, 150, 200, 900	0.764		
					0, 30, 60, 100, 150, 200, 400, 600,	0.754		
					900			
Ding <i>et al</i> <sup>[94]</sup>	1.5	FB	New Inuyama	Whole right lobe	0, 500	0.61	30.4	90.6
Feier <i>et al</i> <sup>[43]</sup>	3	NA	MTAVIR	1 ROI, Right	50, 300, 600	0.77	81.08	72.5
Fujimoto <i>et al</i> <sup>[95]</sup>	1.5	NA	MTAVIR	4 ROIs, Right	0, 1000 (entropy ADC)	0.926	87	84
Do <i>et al</i> <sup>[46]</sup>	1.5	BT	Ludwig	4 ROIs, Right	0, 50, 500 (normalized ADC)	0.689	56	71
Bonekamp <i>et al</i> <sup>[96]</sup>	1.5	BT	MTAVIR	9 ROIs, Both	0, 750	0.8	83.9	68.5
Wang <i>et al</i> <sup>[44]</sup>	1.5	NA	MTAVIR	3 ROIs, Right	50, 500, 1000	0.84	88	76
Lewin <i>et al</i> <sup>[41]</sup>	1.5	RT	MTAVIR	3 ROIs, Right	0, 200, 400, 800	0.92	87	87
Sandrosegaran <i>et al</i> <sup>[40]</sup>	1.5	BH		2 ROIs, Both	50, 400	0.656	51.7	71.4

BH: Breath-hold; RT: Respiratory gating.

significantly related to restricted diffusion in a cirrhotic liver, whereas diffusion-related parameters (D: Slow component of diffusion) were not significantly related. Several studies followed after this study<sup>[5,45,47-53]</sup>. Including the study of Luciani *et al*<sup>[5]</sup>, 3 studies<sup>[49,52,53]</sup> only compared cirrhotic liver with healthy volunteer liver but did not evaluate the fibrosis grade. D\* was found to be significantly lower in the cirrhotic liver in all studies and D showed a significantly lower value in 2 studies<sup>[52,53]</sup>. In these 2 studies, the authors adopted relatively more of high *b*-values and less of low *b*-values. On the other hand, Chung *et al*<sup>[48]</sup> calculated IVIM parameters using 3 patterns of *b*-value selection to diagnose high-grade liver fibrosis: *b* = 0, 30, 60, 100, 150, 200, 400, 600, 900 s/mm<sup>2</sup>; *b* = 0, 30, 60, 100, 150, 200, 900 s/mm<sup>2</sup>; and *b* = 0, 100, 200, 900 s/mm<sup>2</sup>. They suggested that the number of lower *b*-values was not crucial for diagnosing high-grade liver fibrosis. Girometti *et al*<sup>[50]</sup> have suggested that higher *b*-values may not be necessary for diagnosing liver fibrosis. Supporting these hypotheses, Wu *et al*<sup>[47]</sup> suggested that favorable results were given by *b*-values 0, 20, 40, 60, 80, 100, 150, 200, 400, and 800 s/mm<sup>2</sup>.

### Effects of steatosis

Steatosis has been reported to have possible effects on ADC. Poyraz *et al* have suggested that steatosis decreases ADC because the increased fat content of hepatocytes and the extracellular fat accumulation reduce the interstitial space and restrict water diffusion<sup>[39,54]</sup>. Other studies have evaluated the effects of fat deposition by DWI using other methods. These studies estimated that fat has several components that broaden the spectrum and mimic

T2\* decay at short TE ranges; however, the accurate mechanism is unknown<sup>[55,56]</sup>. Another study mentioned that IVIM parameters, such as diffusion coefficient and perfusion fraction, are not affected by the fat fraction and have the possibility of evaluating liver fibrosis regardless of the fat deposition<sup>[57]</sup>.

### Effects of iron deposition

The most widely used sequence for DWI is EPI, which allows acquisition of a full slice in a single shot. However, the EPI readout is also subject to ghosting and susceptibility artifacts, and may decrease ADC as a result of the T2\* shortening effect<sup>[8,58]</sup>. Chronic liver disease may often have iron overload. Therefore, if extremely low ADCs are obtained, iron overload should be considered<sup>[59-63]</sup>.

## DETECTION AND CHARACTERIZATION OF LIVER TUMORS

### Detection of liver tumors

DWI has a better contrast-to-noise ratio and better conspicuity by suppression of background vessels in low *b*-values<sup>[64]</sup>. DWI has a higher detection rate of liver tumors than T2WI<sup>[64,65]</sup>, particularly in detecting malignant lesions<sup>[66]</sup>. However, the ADC of benign solid lesions has been reported to be similar to that of the liver parenchyma<sup>[67]</sup>. Therefore, benign solid lesions may be difficult to detect on DWI.

Many studies have reported that DWI has an additional value for detecting liver metastasis in combination with Gd-EOB-DTPA (Table 2); however, this remains controversial in hepatocellular carcinoma (HCC). Some

**Table 2** Detection of liver tumor in combination with Gd-EOB-DTPA- enhanced magnetic resonance imaging

	Tesla	Respiratory	<i>b</i> -value ( $\times 10^{-3}$ s/mm <sup>2</sup> )	Tumor	Results
Kim <i>et al</i> <sup>[97]</sup>	3	RT	0, 100, 800	Mets (Various)	Combined EOB-MRI and DWI yielded better accuracy and sensitivity
Chung <i>et al</i> <sup>[98]</sup>	3	FB	50, 400, 800	Mets (colorectal)	Combined EOB-MRI and DWI yielded better accuracy and sensitivity
Koh <i>et al</i> <sup>[99]</sup>	1.5	FB	0, 50, 100, 250, 500, 750	Mets (colorectal)	Combined EOB-MRI and DWI improved detection
Löwenthal <i>et al</i> <sup>[100]</sup>	1.5	BH	0, 500	Mets (colorectal)	DWI can detect small lesions
Shimada <i>et al</i> <sup>[101]</sup>	3	RT	0, 500	Mets (Various)	EOB-MRI showed higher accuracy
Donati <i>et al</i> <sup>[102]</sup>	1.5	BH	0, 150, 500	Mets (Various)	No added value of DWI
Kim <i>et al</i> <sup>[103]</sup>	1.5	RT	0, 50, 600	Mets, HCC	DWI increases sensitivity for detecting Mets No added value of DWI for HCC detection

DWI: Diffusion-weighted imaging; BH: Breath-hold; RT: Respiratory gating; FB: Free breathing; HCC: Hepatocellular carcinoma.

**Table 3** Characteristic differentiation of liver tumors

	Tesla	<i>b</i> -value	ADC ( $\times 10^{-3}$ mm <sup>2</sup> )					
			Benign			Malignant		
			Cyst	Hemangioma	All	HCC	Mets	All
Goshima <i>et al</i> <sup>[104]</sup>	1.5	0, 100, 200, 400, 800	3.70 ± 0.9	1.23 ± 0.2		1.08 ± 0.3	0.99 ± 0.5	
Battal <i>et al</i> <sup>[105]</sup>	1.5	0, 800			1.94 ± 0.61			0.86 ± 0.13
Gurtosoyianni <i>et al</i> <sup>[106]</sup>	1.5	0, 50, 500, 1000	2.55	1.9	2.55	1.38	0.99	1.04
Testa <i>et al</i> <sup>[71]</sup>	1.5	0, 600	2.4				1	
Miller <i>et al</i> <sup>[73]</sup>	1.5	0, 500	3.40 ± 0.48	2.26 ± 0.70	2.50 ± 0.86	1.54 ± 0.44	1.50 ± 0.65	1.52 ± 0.55
Namimoto <i>et al</i> <sup>[107]</sup>	1.5	30, 1200	3.05	1.95		0.99	1.15	1.04
Kim <i>et al</i> <sup>[108]</sup>	1.5	3, 57, 192, 408, 517, 705, 846	2.91 ± 1.51	2.04 ± 1.01	2.49 ± 1.39	0.97 ± 0.31	1.06 ± 0.50	1.01 ± 0.38
Taouli <i>et al</i> <sup>[67]</sup>	1.5	0, 500	3.63 ± 0.56	2.95 ± 0.67		1.33 ± 0.13	0.94 ± 0.60	
Cieszanowsk <i>et al</i> <sup>[109]</sup>	1.5	50, 400, 800	2.45	1.55	1.86	0.94	1.05	1.07
Bruegel <i>et al</i> <sup>[72]</sup>	1.5	50, 300, 600	3.02 ± 0.31	1.92 ± 0.34		1.05 ± 0.09	1.22 ± 0.31	
Kandpal <i>et al</i> <sup>[13]</sup>	1.5	0, 500	2.90 ± 0.51	2.36 ± 0.48		1.27 ± 0.42	1.13 ± 0.41	
Demir <i>et al</i> <sup>[110]</sup>	1.5	0, 1000	3.05 ± 0.26	2.46 ± 0.21	2.57 ± 0.26	0.90 ± 0.10	0.79 ± 0.11	0.86 ± 0.11
Oner <i>et al</i> <sup>[111]</sup>	1.5	0, 500	2.34 ± 0.36	1.72 ± 0.30			1.03 ± 0.24	
Holzzapfel <i>et al</i> <sup>[112]</sup>	1.5	50, 300, 600	2.61 ± 0.57	1.69 ± 0.34	2.36 ± 0.62	1.12 ± 0.28	1.08 ± 0.32	1.09 ± 0.30

ADC: Apparent diffusion coefficient; HCC: Hepatocellular carcinoma.

authors have reported no additional value because some well-differentiated HCCs could not be detected on DWI as the major reason<sup>[68]</sup>. Well-differentiated HCCs include variable pathological characteristics like as early HCCs whose pathology is very similar to the surrounding liver parenchyma, steatosis contained lesion and a hypervascular lesion. Kim *et al*<sup>[69]</sup> reported that early HCCs showed hyperintensity on DWI which was strongly associated with their progression to hypervascular HCCs.

### Characteristic differentiation of liver tumors (benign vs malignant)

In hypercellular tissue, extracellular water cannot diffuse and this results in a reduction in ADC. A cystic component has few structures to restrict diffusion and this result in a high ADC. Cysts can be distinguished from solid lesions easily. The cut-off ADC was reported to be approximately  $2.5 \times 10^{-3}$  mm<sup>2</sup>/s for distinguishing cysts from other solid liver tumors<sup>[70]</sup>. Hemangioma

is also relatively easy to distinguish from malignant lesions. The ADC of hemangioma was reported to be approximately  $1.4 \times 10^{-3}$  mm<sup>2</sup>/s. However, some overlaps have been recognized which reduce accuracy in distinguishing metastatic lesions<sup>[71]</sup>. This is particularly true for mucinous carcinoma from the ovary which mimics colorectal carcinoma (Figure 1). However, tumor characterization was reportedly not dependent on size<sup>[72]</sup> (Table 3).

DWI is reportedly not helpful in differentiating focal nodular hyperplasia and adenoma from solid malignant lesions. The mean ADCs of these benign solid lesions were reported as  $1.40$ - $1.79 \times 10^{-3}$  mm<sup>2</sup>/s<sup>[72,73]</sup>. Notably, the ADCs of these benign solid lesions and those of malignant lesions such as HCCs and metastatic tumors overlap (Figure 2).

### Histological differentiation of HCC

Preoperative prediction of the histological grade of HCC

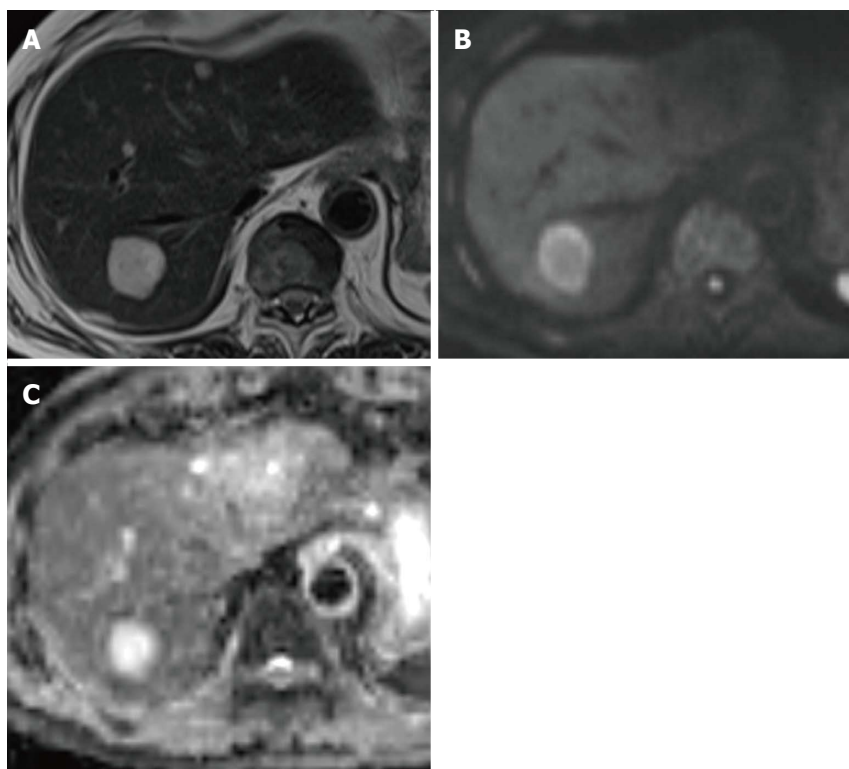


**Figure 1** A 65-year-old man with metastatic tumor in the liver from colorectal carcinoma. A: T2-weighted imaging shows an obvious hyperintense lesion on segment VII (arrow); B: DWI (*b*-value of 800 s/mm<sup>2</sup>) shows hyperintensity; C: Apparent diffusion coefficient map also shows hyperintensity. This finding mimics that for hemangioma. DWI: Diffusion-weighted imaging.

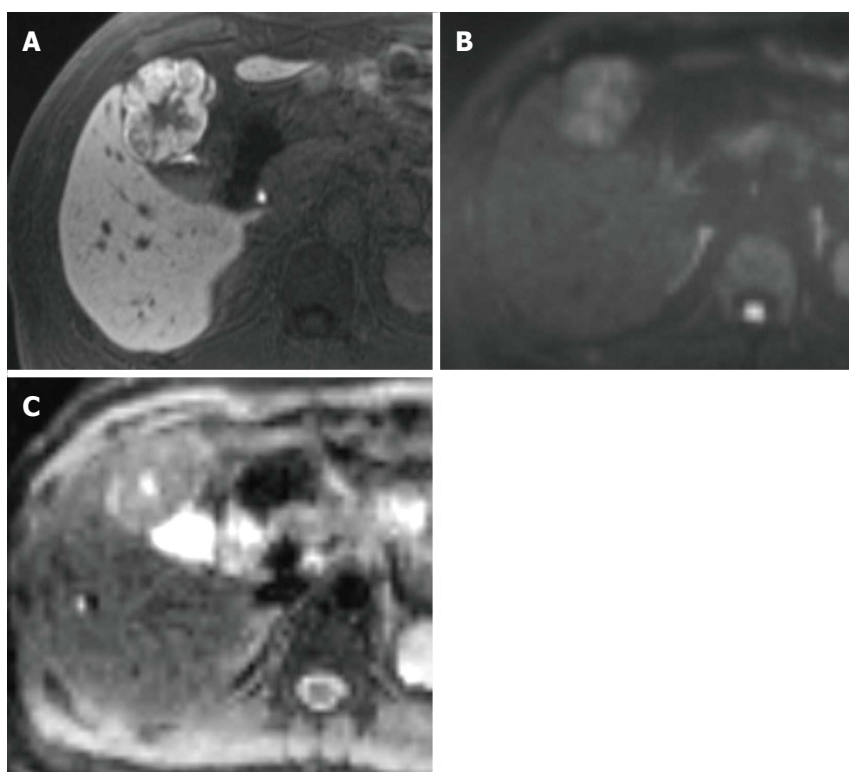


**Figure 2** A 45-year-old man with focal nodular hyperplasia. A: Hepatobiliary phase on Gd-EOB-DTPA-enhanced MRI shows mainly hyperintensity on the outer layer and hypointensity on the inner layer. These enhancement patterns are typical radiologic findings of focal nodular hyperplasia; B: DWI (*b*-value of 800 s/mm<sup>2</sup>) shows hyperintensity; C: ADC map shows heterogeneous hyperintensity. The ADC is  $1.40 \times 10^{-3}$  mm<sup>2</sup>/s. Gd-EOB-DTPA-enhanced MRI is more useful for obtaining a precise diagnosis than DWI alone. MRI: Magnetic resonance imaging; DWI: Diffusion-weighted imaging; ADC: Apparent diffusion coefficient.

can facilitate the estimation of prognosis and contribute to the choice of therapy. There is also a higher incidence of recurrence in poorly differentiated HCCs than in well-differentiated and moderately differentiated HCCs<sup>[74,75]</sup>.

Histological grade correlates with cellularity and structural atypia which includes trabecular, pseudoglandular, solid, and scirrhous. As HCC progresses to poorly differentiated HCC, there is increased cellular density, nuclear/

cytoplasmic ratio and intracellular organelles; thickened cellular plates; and shrinkage of the extracellular and intracellular spaces. This may lead to restricted diffusion in poorly differentiated HCC. However, the results have been inconsistent<sup>[75-79]</sup> (Table 4). One of the main reasons for this inconsistency is the region of interest (ROI) setting. Previous studies showed no significant differences in the ROI setting for each histological grade on whole lesions<sup>[76,77]</sup>. On the

**Table 4** Histological differentiation of hepatocellular carcinoma using apparent diffusion coefficient

	Tesla	Respiratory	b-value (s/mm <sup>2</sup> )	Well-diff HCC ( $\times 10^{-3}$ mm <sup>2</sup> /s)	Mod diff HCC ( $\times 10^{-3}$ mm <sup>2</sup> /s)	Poorly diff HCC ( $\times 10^{-3}$ mm <sup>2</sup> /s)	Difference
Saito <i>et al</i> <sup>[113]</sup>	1.5	RT	100, 800	1.25 $\pm$ 0.25	1.12 $\pm$ 0.22	1.13 $\pm$ 0.23	NS
Nasu <i>et al</i> <sup>[114]</sup>	1.5	RT	0, 500	1.45 $\pm$ 0.35	1.46 $\pm$ 0.32	1.36 $\pm$ 0.29	NS
Heo <i>et al</i> <sup>[77]</sup>	1.5	FB	0, 1000	1.2 $\pm$ 0.22	1.1 $\pm$ 0.10	0.9 $\pm$ 0.13	p < w, m
Nakanishi <i>et al</i> <sup>[80]</sup>	1.5	RT	50, 1000	NA	1.29 $\pm$ 0.21	1.07 $\pm$ 0.15	p < m
Nishie <i>et al</i> <sup>[75]</sup>	1.5	RT	0, 500, 1000	1.21 $\pm$ 0.11	1.14 $\pm$ 0.26	0.76 $\pm$ 0.10	p < w, m
Guo <i>et al</i> <sup>[79]</sup>	3.0	BH	0, 600	1.43 $\pm$ 0.09	1.34 $\pm$ 0.19	1.16 $\pm$ 0.16	p < w, m

RT: Respiratory trigger; BH: Breath holding; FB: Free breathing; ADC: Apparent diffusion coefficient. p < w, m: ADC in poorly differentiated HCC was significantly lower than ADC in well-differentiated HCC and moderately differentiated HCC; p < m: ADC in poorly differentiated HCC was significantly lower than ADC in moderately differentiated HCC; NS: No significant difference in ADC was observed for each histological grade; NA: Not applicable.

other hand, in cases of the ROI set at the lowest ADC and the ROI set to avoid a necrotic or cystic area, a lower ADC was obtained in poorly differentiated HCC<sup>[75,78,79]</sup>.

The current applications are IVIM and ADC minimum. D shows a better diagnostic performance than ADC in distinguishing high-grade HCC from low-grade HCC<sup>[80]</sup>. ADC contains combined information on cell density (D) and perfusion (f) (microcirculation). Minimum-spot ADC was reported to be significantly lower in poorly differentiated HCC than in well-differentiated HCC and moderately differentiated HCC<sup>[75]</sup>.

## MONITORING OF THERAPY

### Transarterial chemoembolization in HCC

Tumor necrosis shows a high intensity on the ADC map, representing free diffusion of water molecules<sup>[81]</sup>. Therefore, DWI can evaluate the therapeutic outcome of transarterial chemoembolization (TACE). In case of a hypervascular lesion without a definite venous washout, DWI has an advantage compared with dynamic MRI and improves the detection of marginal tumor recurrence<sup>[14]</sup>, although dynamic MRI has a more accurate correlation with histopathological findings in necrosis. TACE-induced perilesional parenchymal changes negatively affect DWI in terms of overall accuracy. On the other hand, Kokabi *et al*<sup>[82]</sup> reported that an ADC change 3 h after TACE is an accurate predictor of treatment response and survival.

IVIM and diffusion kurtosis imaging (DKI) are current imaging biomarkers. Specifically, D\* predicts lipiodol uptake<sup>[83]</sup>. DKI is reportedly a more reliable imaging biomarker than ADC<sup>[84]</sup>.

### Chemotherapy in liver metastasis

Some studies have reported that ADC could predict the response to chemotherapy in liver metastasis<sup>[85,86]</sup>. Liang *et al* reported that pretreatment ADC is significantly lower in responders<sup>[87]</sup>. In contrast, Koh *et al*<sup>[85]</sup> reported that a high pretreatment ADC predicted a poor response. Furthermore, ADC increases 3 or 7 d after chemotherapy in responders. Recently, ADC histogram analysis has shown that the mean, 1<sup>st</sup> percentile, 10<sup>th</sup> percentile, 50<sup>th</sup> percentile, 90<sup>th</sup> percentile, and 99<sup>th</sup> percentile were significantly lower in the responding group than

in the nonresponding group. The reason why ADC in responders is lower is that high cell density tumors are well perfused, resulting in the high delivery and retention of chemotherapeutic drugs.

### Sorafenib in HCC

IVIM has been proposed for evaluating the therapeutic outcome of sorafenib<sup>[88,89]</sup>. D before treatment in responders was found to be higher than D before treatment in nonresponders<sup>[88]</sup>. This might be due to the tumor histological grade. Sorafenib acts more effectively in low-grade HCCs<sup>[90]</sup>. D can better distinguish low-grade HCCs from high-grade HCCs<sup>[80]</sup>, and a higher D indicates low-grade HCCs. Lewin *et al*<sup>[89]</sup> reported that f increased significantly in responders after 2 wk. This perfusion parameter f increases with normalization of tumor vessels.

## CONCLUSION

DWI has potential as an imaging biomarker for fibrosis, tumor detection/characterization, and following/predicting therapy outcome. To improve accuracy and reproducibility, researchers have validated this new technique in terms of image acquisition, data sampling, and analysis. The added value of DWI in contrast-enhanced MRI has been established in the detection of malignant lesions of the liver. However, some limitations remain in terms of lesion characterization and fibrosis detection. Furthermore, the methodologies of image acquisition and data analysis have been inconsistent. Therefore, researchers should make every effort not only to improve accuracy and reproducibility but also to standardize the imaging parameters.

## REFERENCES

- 1 Prince MR, Zhang H, Zou Z, Staron RB, Brill PW. Incidence of immediate gadolinium contrast media reactions. *AJR Am J Roentgenol* 2011; **196**: W138-W143 [PMID: 21257854 DOI: 10.2214/AJR.10.4885]
- 2 Stejskal EO, Tanner JE. Spin diffusion measurements: spin echoes in the presence of a time-dependent field gradient. *J Chem Phys* 1965; **42**: 288-292 [DOI: 10.1063/1.1695690]
- 3 Le Bihan D, Breton E, Lallemand D, Grenier P, Cabanis E, Laval-Jeantet M. MR imaging of intravoxel incoherent motions: application to diffusion and perfusion in neurologic disorders.

- Radiology* 1986; **161**: 401-407 [PMID: 3763909 DOI: 10.1148/radiology.161.2.3763909]
- 4 **Yamada I**, Aung W, Himeno Y, Nakagawa T, Shibuya H. Diffusion coefficients in abdominal organs and hepatic lesions: evaluation with intravoxel incoherent motion echo-planar MR imaging. *Radiology* 1999; **210**: 617-623 [PMID: 10207458 DOI: 10.1148/radiology.210.3.r99fe17617]
  - 5 **Luciani A**, Vignaud A, Cavet M, Nhieu JT, Mallat A, Ruel L, Laurent A, Deux JF, Brugieres P, Rahmouni A. Liver cirrhosis: intravoxel incoherent motion MR imaging—pilot study. *Radiology* 2008; **249**: 891-899 [PMID: 19011186 DOI: 10.1148/radiol.2493080080]
  - 6 **Andreou A**, Koh DM, Collins DJ, Blackledge M, Wallace T, Leach MO, Orton MR. Measurement reproducibility of perfusion fraction and pseudodiffusion coefficient derived by intravoxel incoherent motion diffusion-weighted MR imaging in normal liver and metastases. *Eur Radiol* 2013; **23**: 428-434 [PMID: 23052642 DOI: 10.1007/s00330-012-2604-1]
  - 7 **Dyvorne HA**, Galea N, Nevers T, Fiel MI, Carpenter D, Wong E, Orton M, de Oliveira A, Feiweier T, Vachon ML, Babb JS, Taouli B. Diffusion-weighted imaging of the liver with multiple b values: effect of diffusion gradient polarity and breathing acquisition on image quality and intravoxel incoherent motion parameters—a pilot study. *Radiology* 2013; **266**: 920-929 [PMID: 23220895 DOI: 10.1148/radiol.12120686]
  - 8 **Chandarana H**, Do RK, Mussi TC, Jensen JH, Hajdu CH, Babb JS, Taouli B. The effect of liver iron deposition on hepatic apparent diffusion coefficient values in cirrhosis. *AJR Am J Roentgenol* 2012; **199**: 803-808 [PMID: 22997371 DOI: 10.2214/AJR.11.7541]
  - 9 **Taouli B**, Martin AJ, Qayyum A, Merriman RB, Vigneron D, Yeh BM, Coakley FV. Parallel imaging and diffusion tensor imaging for diffusion-weighted MRI of the liver: preliminary experience in healthy volunteers. *AJR Am J Roentgenol* 2004; **183**: 677-680 [PMID: 15333355 DOI: 10.2214/ajr.183.3.1830677]
  - 10 **Bammer R**, Keeling SL, Augustin M, Pruessmann KP, Wolf R, Stollberger R, Hartung HP, Fazekas F. Improved diffusion-weighted single-shot echo-planar imaging (EPI) in stroke using sensitivity encoding (SENSE). *Magn Reson Med* 2001; **46**: 548-554 [PMID: 11550248 DOI: 10.1002/mrm.1226]
  - 11 **Yoshikawa T**, Kawamitsu H, Mitchell DG, Ohno Y, Ku Y, Seo Y, Fujii M, Sugimura K. ADC measurement of abdominal organs and lesions using parallel imaging technique. *AJR Am J Roentgenol* 2006; **187**: 1521-1530 [PMID: 17114546 DOI: 10.2214/AJR.05.0778]
  - 12 **Wiesinger F**, Van de Moortele PF, Adriany G, De Zanche N, Ugurbil K, Pruessmann KP. Parallel imaging performance as a function of field strength—an experimental investigation using electrodynamic scaling. *Magn Reson Med* 2004; **52**: 953-964 [PMID: 15508167 DOI: 10.1002/mrm.20281]
  - 13 **Kandpal H**, Sharma R, Madhusudhan KS, Kapoor KS. Respiratory-triggered versus breath-hold diffusion-weighted MRI of liver lesions: comparison of image quality and apparent diffusion coefficient values. *AJR Am J Roentgenol* 2009; **192**: 915-922 [PMID: 19304695 DOI: 10.2214/AJR.08.1260]
  - 14 **Taouli B**, Sandberg A, Stemmer A, Parikh T, Wong S, Xu J, Lee VS. Diffusion-weighted imaging of the liver: comparison of navigator triggered and breathhold acquisitions. *J Magn Reson Imaging* 2009; **30**: 561-568 [PMID: 19711402 DOI: 10.1002/jmri.21876]
  - 15 **Asbach P**, Hein PA, Stemmer A, Wagner M, Huppertz A, Hamm B, Taupitz M, Klessen C. Free-breathing echo-planar imaging based diffusion-weighted magnetic resonance imaging of the liver with prospective acquisition correction. *J Comput Assist Tomogr* 2008; **32**: 372-378 [PMID: 18520540 DOI: 10.1097/RCT.0b013e3180dc930c]
  - 16 **Nasu K**, Kuroki Y, Fujii H, Minami M. Hepatic pseudo-anisotropy: a specific artifact in hepatic diffusion-weighted images obtained with respiratory triggering. *MAGMA* 2007; **20**: 205-211 [PMID: 17960439 DOI: 10.1007/s10334-007-0084-0]
  - 17 **Nasu K**, Kuroki Y, Sekiguchi R, Nawano S. The effect of simultaneous use of respiratory triggering in diffusion-weighted imaging of the liver. *Magn Reson Med Sci* 2006; **5**: 129-136 [PMID: 17139138 DOI: 10.2463/mrms.5.129]
  - 18 **Jerome NP**, Orton MR, d'Arcy JA, Collins DJ, Koh DM, Leach MO. Comparison of free-breathing with navigator-controlled acquisition regimes in abdominal diffusion-weighted magnetic resonance images: Effect on ADC and IVIM statistics. *J Magn Reson Imaging* 2014; **39**: 235-240 [PMID: 23580454 DOI: 10.1002/jmri.24140]
  - 19 **Kwee TC**, Takahara T, Koh DM, Niveststein RA, Luijten PR. Comparison and reproducibility of ADC measurements in breathhold, respiratory triggered, and free-breathing diffusion-weighted MR imaging of the liver. *J Magn Reson Imaging* 2008; **28**: 1141-1148 [PMID: 18972355 DOI: 10.1002/jmri.21569]
  - 20 **Chen X**, Qin L, Pan D, Huang Y, Yan L, Wang G, Liu Y, Liang C, Liu Z. Liver diffusion-weighted MR imaging: reproducibility comparison of ADC measurements obtained with multiple breath-hold, free-breathing, respiratory-triggered, and navigator-triggered techniques. *Radiology* 2014; **271**: 113-125 [PMID: 24475860 DOI: 10.1148/radiol.13131572]
  - 21 **Hamm B**, Staks T, Mühler A, Bollow M, Taupitz M, Frenzel T, Wolf KJ, Weimann HJ, Lange L. Phase I clinical evaluation of Gd-EOB-DTPA as a hepatobiliary MR contrast agent: safety, pharmacokinetics, and MR imaging. *Radiology* 1995; **195**: 785-792 [PMID: 7754011 DOI: 10.1148/radiology.195.3.7754011]
  - 22 **Saito K**, Araki Y, Park J, Metoki R, Katsuyama H, Nishio R, Kakizaki D, Moriyasu F, Tokuyue K. Effect of Gd-EOB-DTPA on T2-weighted and diffusion-weighted images for the diagnosis of hepatocellular carcinoma. *J Magn Reson Imaging* 2010; **32**: 229-234 [PMID: 20578029 DOI: 10.1002/jmri.22219]
  - 23 **Colagrande S**, Mazzoni LN, Mazzoni E, Pradella S. Effects of gadoteric acid on quantitative diffusion-weighted imaging of the liver. *J Magn Reson Imaging* 2013; **38**: 365-370 [PMID: 23239165 DOI: 10.1002/jmri.23978]
  - 24 **Liau J**, Lee J, Schroeder ME, Sirlin CB, Bydder M. Cardiac motion in diffusion-weighted MRI of the liver: artifact and a method of correction. *J Magn Reson Imaging* 2012; **35**: 318-327 [PMID: 21959926 DOI: 10.1002/jmri.22816]
  - 25 **Kwee TC**, Takahara T, Niwa T, Ivancevic MK, Herigault G, Van Cauteren M, Luijten PR. Influence of cardiac motion on diffusion-weighted magnetic resonance imaging of the liver. *MAGMA* 2009; **22**: 319-325 [PMID: 19727877 DOI: 10.1007/s10334-009-0183-1]
  - 26 **Kim SY**, Lee SS, Byun JH, Park SH, Kim JK, Park B, Kim N, Lee MG. Malignant hepatic tumors: short-term reproducibility of apparent diffusion coefficients with breath-hold and respiratory-triggered diffusion-weighted MR imaging. *Radiology* 2010; **255**: 815-823 [PMID: 20501719 DOI: 10.1148/radiol.10091706]
  - 27 **Metens T**, Absil J, Denolin V, Bali MA, Matos C. Liver apparent diffusion coefficient repeatability with individually predetermined optimal cardiac timing and artifact elimination by signal filtering. *J Magn Reson Imaging* 2016; **43**: 1100-1110 [PMID: 26566777 DOI: 10.1002/jmri.25089]
  - 28 **Mürtz P**, Flacke S, Träber F, van den Brink JS, Gieseke J, Schild HH. Abdomen: diffusion-weighted MR imaging with pulse-triggered single-shot sequences. *Radiology* 2002; **224**: 258-264 [PMID: 12091693 DOI: 10.1148/radiol.2241011117]
  - 29 **Atalay MK**, Poncelet BP, Kantor HL, Brady TJ, Weisskoff RM. Cardiac susceptibility artifacts arising from the heart-lung interface. *Magn Reson Med* 2001; **45**: 341-345 [PMID: 11180442]
  - 30 **Wood ML**, Runge VM, Henkelman RM. Overcoming motion in abdominal MR imaging. *AJR Am J Roentgenol* 1988; **150**: 513-522 [PMID: 3257601 DOI: 10.2214/ajr.150.3.513]
  - 31 **Wagner M**, Klessen C, Rief M, Elgeti T, Taupitz M, Hamm B, Asbach P. High-resolution T2-weighted abdominal magnetic resonance imaging using respiratory triggering: impact of butylscopolamine on image quality. *Acta Radiol* 2008; **49**: 376-382 [PMID: 18415778 DOI: 10.1080/02841850801894806]
  - 32 **Nasu K**, Kuroki Y, Sekiguchi R, Kazama T, Nakajima H. Measurement of the apparent diffusion coefficient in the liver: is it a reliable index for hepatic disease diagnosis? *Radiat Med* 2006; **24**: 438-444 [PMID: 16958425 DOI: 10.1007/s11604-006-0053-y]
  - 33 **Friedman SL**. Seminars in medicine of the Beth Israel Hospital, Boston. The cellular basis of hepatic fibrosis. Mechanisms and treatment strategies. *N Engl J Med* 1993; **328**: 1828-1835 [PMID: 8502273 DOI: 10.1056/NEJM199306243282508]

- 34 **Rojkind M**, Giambone MA, Biempica L. Collagen types in normal and cirrhotic liver. *Gastroenterology* 1979; **76**: 710-719 [PMID: 421999]
- 35 **Gressner AM**. The cell biology of liver fibrogenesis - an imbalance of proliferation, growth arrest and apoptosis of myofibroblasts. *Cell Tissue Res* 1998; **292**: 447-452 [PMID: 9582401 DOI: 10.1007/s004410051073]
- 36 **Wong JB**, Bennett WG, Koff RS, Pauker SG. Pretreatment evaluation of chronic hepatitis C: risks, benefits, and costs. *JAMA* 1998; **280**: 2088-2093 [PMID: 9875876 DOI: 10.1001/jama.280.24.2088]
- 37 **Regev A**, Berho M, Jeffers LJ, Milikowski C, Molina EG, Pyrsopoulos NT, Feng ZZ, Reddy KR, Schiff ER. Sampling error and intraobserver variation in liver biopsy in patients with chronic HCV infection. *Am J Gastroenterol* 2002; **97**: 2614-2618 [PMID: 12385448 DOI: 10.1111/j.1572-0241.2002.06038.x]
- 38 **Howlett DC**, Drinkwater KJ, Lawrence D, Barter S, Nicholson T. Findings of the UK national audit evaluating image-guided or image-assisted liver biopsy. Part II. Minor and major complications and procedure-related mortality. *Radiology* 2013; **266**: 226-235 [PMID: 23143026 DOI: 10.1148/radiol.12120224]
- 39 **Bakan AA**, Inci E, Bakan S, Gokturk S, Cimilli T. Utility of diffusion-weighted imaging in the evaluation of liver fibrosis. *Eur Radiol* 2012; **22**: 682-687 [PMID: 21984447 DOI: 10.1007/s00330-011-2295-z]
- 40 **Sandrasegaran K**, Akisik FM, Lin C, Tahir B, Rajan J, Saxena R, Aisen AM. Value of diffusion-weighted MRI for assessing liver fibrosis and cirrhosis. *AJR Am J Roentgenol* 2009; **193**: 1556-1560 [PMID: 19933647 DOI: 10.2214/AJR.09.2436]
- 41 **Lewin M**, Poujol-Robert A, Boëlle PY, Wendum D, Lasnier E, Viallon M, Guéchet J, Hoëffel C, Arrivé L, Tubiana JM, Poupon R. Diffusion-weighted magnetic resonance imaging for the assessment of fibrosis in chronic hepatitis C. *Hepatology* 2007; **46**: 658-665 [PMID: 17663420 DOI: 10.1002/hep.21747]
- 42 **Wang QB**, Zhu H, Liu HL, Zhang B. Performance of magnetic resonance elastography and diffusion-weighted imaging for the staging of hepatic fibrosis: A meta-analysis. *Hepatology* 2012; **56**: 239-247 [PMID: 22278368 DOI: 10.1002/hep.25610]
- 43 **Feier D**, Balassy C, Bastati N, Fragner R, Wrba F, Ba-Ssalamah A. The diagnostic efficacy of quantitative liver MR imaging with diffusion-weighted, SWI, and hepato-specific contrast-enhanced sequences in staging liver fibrosis--a multiparametric approach. *Eur Radiol* 2016; **26**: 539-546 [PMID: 25991488 DOI: 10.1007/s00330-015-3830-0]
- 44 **Wang Y**, Ganger DR, Levitsky J, Sternick LA, McCarthy RJ, Chen ZE, Fasanati CW, Bolster B, Shah S, Zuehlsdorff S, Omary RA, Ehman RL, Miller FH. Assessment of chronic hepatitis and fibrosis: comparison of MR elastography and diffusion-weighted imaging. *AJR Am J Roentgenol* 2011; **196**: 553-561 [PMID: 21343496 DOI: 10.2214/AJR.10.4580]
- 45 **Ichikawa S**, Motosugi U, Morisaka H, Sano K, Ichikawa T, Enomoto N, Matsuda M, Fujii H, Onishi H. MRI-based staging of hepatic fibrosis: Comparison of intravoxel incoherent motion diffusion-weighted imaging with magnetic resonance elastography. *J Magn Reson Imaging* 2015; **42**: 204-210 [PMID: 25223820 DOI: 10.1002/jmri.24760]
- 46 **Do RK**, Chandarana H, Felker E, Hajdu CH, Babb JS, Kim D, Taouli B. Diagnosis of liver fibrosis and cirrhosis with diffusion-weighted imaging: value of normalized apparent diffusion coefficient using the spleen as reference organ. *AJR Am J Roentgenol* 2010; **195**: 671-676 [PMID: 20729445 DOI: 10.2214/AJR.09.3448]
- 47 **Wu CH**, Ho MC, Jeng YM, Liang PC, Hu RH, Lai HS, Shih TT. Assessing hepatic fibrosis: comparing the intravoxel incoherent motion in MRI with acoustic radiation force impulse imaging in US. *Eur Radiol* 2015; **25**: 3552-3559 [PMID: 25991478 DOI: 10.1007/s00330-015-3774-4]
- 48 **Chung SR**, Lee SS, Kim N, Yu ES, Kim E, Kühn B, Kim IS. Intravoxel incoherent motion MRI for liver fibrosis assessment: a pilot study. *Acta Radiol* 2015; **56**: 1428-1436 [PMID: 25414372 DOI: 10.1177/0284185114559763]
- 49 **Patel J**, Sigmund EE, Rusinek H, Oei M, Babb JS, Taouli B. Diagnosis of cirrhosis with intravoxel incoherent motion diffusion MRI and dynamic contrast-enhanced MRI alone and in combination: preliminary experience. *J Magn Reson Imaging* 2010; **31**: 589-600 [PMID: 20187201 DOI: 10.1002/jmri.22081]
- 50 **Girometti R**, Furlan A, Esposito G, Bazzocchi M, Como G, Soldano F, Isola M, Toniutto P, Zuiani C. Relevance of b-values in evaluating liver fibrosis: a study in healthy and cirrhotic subjects using two single-shot spin-echo echo-planar diffusion-weighted sequences. *J Magn Reson Imaging* 2008; **28**: 411-419 [PMID: 18666139 DOI: 10.1002/jmri.21461]
- 51 **Murphy P**, Hooker J, Ang B, Wolfson T, Gamst A, Bydder M, Middleton M, Peterson M, Behling C, Loomba R, Sirlin C. Associations between histologic features of nonalcoholic fatty liver disease (NAFLD) and quantitative diffusion-weighted MRI measurements in adults. *J Magn Reson Imaging* 2015; **41**: 1629-1638 [PMID: 25256692 DOI: 10.1002/jmri.24755]
- 52 **Hayashi T**, Miyati T, Takahashi J, Fukuzawa K, Sakai H, Tano M, Saitoh S. Diffusion analysis with triexponential function in liver cirrhosis. *J Magn Reson Imaging* 2013; **38**: 148-153 [PMID: 23239543 DOI: 10.1002/jmri.23966]
- 53 **Lu PX**, Huang H, Yuan J, Zhao F, Chen ZY, Zhang Q, Ahuja AT, Zhou BP, Wang YX. Decreases in molecular diffusion, perfusion fraction and perfusion-related diffusion in fibrotic livers: a prospective clinical intravoxel incoherent motion MR imaging study. *PLoS One* 2014; **9**: e113846 [PMID: 25436458 DOI: 10.1371/journal.pone.0113846]
- 54 **Hansmann J**, Hernando D, Reeder SB. Fat confounds the observed apparent diffusion coefficient in patients with hepatic steatosis. *Magn Reson Med* 2013; **69**: 545-552 [PMID: 23161434 DOI: 10.1002/mrm.24535]
- 55 **Glover GH**. Multipoint Dixon technique for water and fat proton and susceptibility imaging. *J Magn Reson Imaging* 1991; **1**: 521-530 [PMID: 1790376 DOI: 10.1002/jmri.1880010504]
- 56 **Bydder M**, Yokoo T, Hamilton G, Middleton MS, Chavez AD, Schwimmer JB, Lavine JE, Sirlin CB. Relaxation effects in the quantification of fat using gradient echo imaging. *Magn Reson Imaging* 2008; **26**: 347-359 [PMID: 18093781 DOI: 10.1016/j.jmri.2007.08.012]
- 57 **Lee JT**, Liao J, Murphy P, Schroeder ME, Sirlin CB, Bydder M. Cross-sectional investigation of correlation between hepatic steatosis and IVIM perfusion on MR imaging. *Magn Reson Imaging* 2012; **30**: 572-578 [PMID: 22285877 DOI: 10.1016/j.jmri.2011.12.013]
- 58 **Le Bihan D**, Poupon C, Amadon A, Lethimonnier F. Artifacts and pitfalls in diffusion MRI. *J Magn Reson Imaging* 2006; **24**: 478-488 [PMID: 16897692 DOI: 10.1002/jmri.20683]
- 59 **Hernando D**, Levin YS, Sirlin CB, Reeder SB. Quantification of liver iron with MRI: state of the art and remaining challenges. *J Magn Reson Imaging* 2014; **40**: 1003-1021 [PMID: 24585403 DOI: 10.1002/jmri.24584]
- 60 **Queiroz-Andrade M**, Blasbalg R, Ortega CD, Rodstein MA, Baroni RH, Rocha MS, Cerri GG. MR imaging findings of iron overload. *Radiographics* 2009; **29**: 1575-1589 [PMID: 19959509 DOI: 10.1148/rg.296095511]
- 61 **Metwally MA**, Zein CO, Zein NN. Clinical significance of hepatic iron deposition and serum iron values in patients with chronic hepatitis C infection. *Am J Gastroenterol* 2004; **99**: 286-291 [PMID: 15046219 DOI: 10.1111/j.1572-0241.2004.04049.x]
- 62 **Price L**, Kowdley KV. The role of iron in the pathophysiology and treatment of chronic hepatitis C. *Can J Gastroenterol* 2009; **23**: 822-828 [PMID: 20011735 DOI: 10.1155/2009/290383]
- 63 **Beinker NK**, Voigt MD, Arendse M, Smit J, Stander IA, Kirsch RE. Threshold effect of liver iron content on hepatic inflammation and fibrosis in hepatitis B and C. *J Hepatol* 1996; **25**: 633-638 [PMID: 8938538 DOI: 10.1016/S0168-8278(96)80231-5]
- 64 **Asayama Y**, Yoshimitsu K, Nishihara Y, Irie H, Aishima S, Taketomi A, Honda H. Arterial blood supply of hepatocellular carcinoma and histologic grading: radiologic-pathologic correlation. *AJR Am J Roentgenol* 2008; **190**: W28-W34 [PMID: 18094269 DOI: 10.2214/AJR.07.2117]
- 65 **Bruegel M**, Gaa J, Waldt S, Woertler K, Holzapfel K, Kiefer B, Rummeny EJ. Diagnosis of hepatic metastasis: comparison of respiration-triggered diffusion-weighted echo-planar MRI and five t2-

- weighted turbo spin-echo sequences. *AJR Am J Roentgenol* 2008; **191**: 1421-1429 [PMID: 18941080 DOI: 10.2214/AJR.07.3279]
- 66 **Yang DM**, Jahng GH, Kim HC, Jin W, Ryu CW, Nam DH, Lee YK, Park SY. The detection and discrimination of malignant and benign focal hepatic lesions: T2 weighted vs diffusion-weighted MRI. *Br J Radiol* 2011; **84**: 319-326 [PMID: 20959371 DOI: 10.1259/bjr/50130643]
- 67 **Taouli B**, Vilgrain V, Dumont E, Daire JL, Fan B, Menu Y. Evaluation of liver diffusion isotropy and characterization of focal hepatic lesions with two single-shot echo-planar MR imaging sequences: prospective study in 66 patients. *Radiology* 2003; **226**: 71-78 [PMID: 12511671 DOI: 10.1148/radiol.2261011904]
- 68 **Okada Y**, Ohtomo K, Kiryu S, Sasaki Y. Breath-hold T2-weighted MRI of hepatic tumors: value of echo planar imaging with diffusion-sensitizing gradient. *J Comput Assist Tomogr* 1998; **22**: 364-371 [PMID: 9606375 DOI: 10.1097/00004728-199805000-00005]
- 69 **Kim YK**, Lee WJ, Park MJ, Kim SH, Rhim H, Choi D. Hypovascular hypointense nodules on hepatobiliary phase gadoteric acid-enhanced MR images in patients with cirrhosis: potential of DW imaging in predicting progression to hypervascular HCC. *Radiology* 2012; **265**: 104-114 [PMID: 22891358 DOI: 10.1148/radiol.12112649]
- 70 **Yuan YH**, Xiao EH, Liu JB, He Z, Jin K, Ma C, Xiang J, Xiao JH, Chen WJ. Characteristics and pathological mechanism on magnetic resonance diffusion-weighted imaging after chemoembolization in rabbit liver VX-2 tumor model. *World J Gastroenterol* 2007; **13**: 5699-5706 [PMID: 17963295 DOI: 10.3748/wjg.v13.i43.5699]
- 71 **Testa ML**, Chojniak R, Sene LS, Damascena AS, Guimarães MD, Szklaruk J, Marchiori E. Is DWI/ADC a useful tool in the characterization of focal hepatic lesions suspected of malignancy? *PLoS One* 2014; **9**: e101944 [PMID: 25025151 DOI: 10.1371/journal.pone.0101944]
- 72 **Bruegel M**, Holzapfel K, Gaa J, Woertler K, Waldt S, Kiefer B, Stemmer A, Ganter C, Rummeny EJ. Characterization of focal liver lesions by ADC measurements using a respiratory triggered diffusion-weighted single-shot echo-planar MR imaging technique. *Eur Radiol* 2008; **18**: 477-485 [PMID: 17960390 DOI: 10.1007/s00330-007-0785-9]
- 73 **Miller FH**, Hammond N, Siddiqi AJ, Shroff S, Khatri G, Wang Y, Merrick LB, Nikolaidis P. Utility of diffusion-weighted MRI in distinguishing benign and malignant hepatic lesions. *J Magn Reson Imaging* 2010; **32**: 138-147 [PMID: 20578020 DOI: 10.1002/jmri.22235]
- 74 **Heverhagen JT**. Noise measurement and estimation in MR imaging experiments. *Radiology* 2007; **245**: 638-639 [PMID: 18024445 DOI: 10.1148/radiol.2453062151]
- 75 **Nishie A**, Tajima T, Asayama Y, Ishigami K, Kakihara D, Nakayama T, Takayama Y, Okamoto D, Fujita N, Taketomi A, Yoshimitsu K, Honda H. Diagnostic performance of apparent diffusion coefficient for predicting histological grade of hepatocellular carcinoma. *Eur J Radiol* 2011; **80**: e29-e33 [PMID: 20619566 DOI: 10.1016/j.ejrad.2010.06.019]
- 76 **Nakajima Y**, Shimamura T, Kamiyama T, Kimura J, Sato N, Matsushita M, Une Y, Uchino J. Evaluation of surgical resection for small hepatocellular carcinomas. *Am J Surg* 1996; **171**: 360-363 [PMID: 8615473 DOI: 10.1016/S0002-9610(97)89642-0]
- 77 **Heo SH**, Jeong YY, Shin SS, Kim JW, Lim HS, Lee JH, Koh YS, Cho CK, Kang HK. Apparent diffusion coefficient value of diffusion-weighted imaging for hepatocellular carcinoma: correlation with the histologic differentiation and the expression of vascular endothelial growth factor. *Korean J Radiol* 2010; **11**: 295-303 [PMID: 20461183 DOI: 10.3348/kjr.2010.11.3.295]
- 78 **Woo S**, Lee JM, Yoon JH, Joo I, Han JK, Choi BI. Intravoxel incoherent motion diffusion-weighted MR imaging of hepatocellular carcinoma: correlation with enhancement degree and histologic grade. *Radiology* 2014; **270**: 758-767 [PMID: 24475811 DOI: 10.1148/radiol.13130444]
- 79 **Guo W**, Zhao S, Yang Y, Shao G. Histological grade of hepatocellular carcinoma predicted by quantitative diffusion-weighted imaging. *Int J Clin Exp Med* 2015; **8**: 4164-4169 [PMID: 26064326]
- 80 **Nakanishi M**, Chuma M, Hige S, Omatsu T, Yokoo H, Nakanishi K, Kamiyama T, Kubota K, Haga H, Matsuno Y, Onodera Y, Kato M, Asaka M. Relationship between diffusion-weighted magnetic resonance imaging and histological tumor grading of hepatocellular carcinoma. *Ann Surg Oncol* 2012; **19**: 1302-1309 [PMID: 21927976 DOI: 10.1245/s10434-011-2066-8]
- 81 **Chen CY**, Li CW, Kuo YT, Jaw TS, Wu DK, Jao JC, Hsu JS, Liu GC. Early response of hepatocellular carcinoma to transcatheter arterial chemoembolization: choline levels and MR diffusion constants—initial experience. *Radiology* 2006; **239**: 448-456 [PMID: 16569781 DOI: 10.1148/radiol.2392042202]
- 82 **Kokabi N**, Camacho JC, Xing M, Edalat F, Mittal PK, Kim HS. Immediate post-doxorubicin drug-eluting beads chemoembolization Mr Apparent diffusion coefficient quantification predicts response in unresectable hepatocellular carcinoma: A pilot study. *J Magn Reson Imaging* 2015; **42**: 981-989 [PMID: 25683022 DOI: 10.1002/jmri.24845]
- 83 **Park YS**, Lee CH, Kim JH, Kim IS, Kiefer B, Seo TS, Kim KA, Park CM. Using intravoxel incoherent motion (IVIM) MR imaging to predict lipiodol uptake in patients with hepatocellular carcinoma following transcatheter arterial chemoembolization: a preliminary result. *Magn Reson Imaging* 2014; **32**: 638-646 [PMID: 24703575 DOI: 10.1016/j.mri.2014.03.003]
- 84 **Goshima S**, Kanematsu M, Noda Y, Kondo H, Watanabe H, Bae KT. Diffusion kurtosis imaging to assess response to treatment in hypervascular hepatocellular carcinoma. *AJR Am J Roentgenol* 2015; **204**: W543-W549 [PMID: 25905960 DOI: 10.2214/AJR.14.13235]
- 85 **Koh DM**, Scurr E, Collins D, Kanber B, Norman A, Leach MO, Husband JE. Predicting response of colorectal hepatic metastasis: value of pretreatment apparent diffusion coefficients. *AJR Am J Roentgenol* 2007; **188**: 1001-1008 [PMID: 17377036 DOI: 10.2214/AJR.06.0601]
- 86 **Cui Y**, Zhang XP, Sun YS, Tang L, Shen L. Apparent diffusion coefficient: potential imaging biomarker for prediction and early detection of response to chemotherapy in hepatic metastases. *Radiology* 2008; **248**: 894-900 [PMID: 18710982 DOI: 10.1148/radiol.2483071407]
- 87 **Liang HY**, Huang YQ, Yang ZX, Ying-Ding MS, Rao SX. Potential of MR histogram analyses for prediction of response to chemotherapy in patients with colorectal hepatic metastases. *Eur Radiol* 2016; **26**: 2009-2018 [PMID: 26494642 DOI: 10.1007/s00330-015-4043-2]
- 88 **Shirota N**, Saito K, Sugimoto K, Takara K, Moriyasu F, Tokuyue K. Intravoxel incoherent motion MRI as a biomarker of sorafenib treatment for advanced hepatocellular carcinoma: a pilot study. *Cancer Imaging* 2016; **16**: 1 [PMID: 26822946 DOI: 10.1186/s40644-016-0059-3]
- 89 **Lewin M**, Fartoux L, Vignaud A, Arrivé L, Menu Y, Rosmorduc O. The diffusion-weighted imaging perfusion fraction f is a potential marker of sorafenib treatment in advanced hepatocellular carcinoma: a pilot study. *Eur Radiol* 2011; **21**: 281-290 [PMID: 20683597 DOI: 10.1007/s00330-010-1914-4]
- 90 **Takeda H**, Nishikawa H, Osaki Y, Tsuchiya K, Joko K, Ogawa C, Taniguchi H, Orito E, Uchida Y, Izumi N. Clinical features associated with radiological response to sorafenib in unresectable hepatocellular carcinoma: a large multicenter study in Japan. *Liver Int* 2015; **35**: 1581-1589 [PMID: 24836552 DOI: 10.1111/liv.12591]
- 91 **Cece H**, Ercan A, Yıldız S, Karakas E, Karakas O, Boyacı FN, Aydoğan T, Karakas EY, Cullu N, Ulas T. The use of DWI to assess spleen and liver quantitative ADC changes in the detection of liver fibrosis stages in chronic viral hepatitis. *Eur J Radiol* 2013; **82**: e307-e312 [PMID: 23518145 DOI: 10.1016/j.ejrad.2013.02.022]
- 92 **Taouli B**, Tolia AJ, Losada M, Babb JS, Chan ES, Bannan MA, Tobias H. Diffusion-weighted MRI for quantification of liver fibrosis: preliminary experience. *AJR Am J Roentgenol* 2007; **189**: 799-806 [PMID: 17885048 DOI: 10.2214/AJR.07.2086]
- 93 **Kocakoc E**, Bakan AA, Poyrazoglu OK, Dagli AF, Gul Y, Cicekci M, Bahcecioglu IH. Assessment of Liver Fibrosis with Diffusion-Weighted Magnetic Resonance Imaging Using Different b-values in Chronic Viral Hepatitis. *Med Princ Pract* 2015; **24**: 522-526 [PMID: 26183515 DOI: 10.1159/000434682]
- 94 **Ding Y**, Rao SX, Zhu T, Chen CZ, Li RC, Zeng MS. Liver fibrosis

- staging using T1 mapping on gadoteric acid-enhanced MRI compared with DW imaging. *Clin Radiol* 2015; **70**: 1096-1103 [PMID: 26164421 DOI: 10.1016/j.crad.2015.04.014]
- 95 **Fujimoto K**, Tonan T, Azuma S, Kage M, Nakashima O, Johkoh T, Hayabuchi N, Okuda K, Kawaguchi T, Sata M, Qayyum A. Evaluation of the mean and entropy of apparent diffusion coefficient values in chronic hepatitis C: correlation with pathologic fibrosis stage and inflammatory activity grade. *Radiology* 2011; **258**: 739-748 [PMID: 21248235 DOI: 10.1148/radiol.10100853]
- 96 **Bonekamp D**, Bonekamp S, Ou HY, Torbenson MS, Corona-Villalobos CP, Mezey E, Kamel IR. Assessing liver fibrosis: comparison of arterial enhancement fraction and diffusion-weighted imaging. *J Magn Reson Imaging* 2014; **40**: 1137-1146 [PMID: 24989329 DOI: 10.1002/jmri.24472]
- 97 **Kim YK**, Lee MW, Lee WJ, Kim SH, Rhim H, Lim JH, Choi D, Kim YS, Jang KM, Lee SJ, Lim HK. Diagnostic accuracy and sensitivity of diffusion-weighted and of gadoteric acid-enhanced 3-T MR imaging alone or in combination in the detection of small liver metastasis ( $\leq 1.5$  cm in diameter). *Invest Radiol* 2012; **47**: 159-166 [PMID: 22330426 DOI: 10.1097/RLL.0b013e31823a1495]
- 98 **Chung WS**, Kim MJ, Chung YE, Kim YE, Park MS, Choi JY, Kim KW. Comparison of gadoteric acid-enhanced dynamic imaging and diffusion-weighted imaging for the preoperative evaluation of colorectal liver metastases. *J Magn Reson Imaging* 2011; **34**: 345-353 [PMID: 21702068 DOI: 10.1002/jmri.22671]
- 99 **Koh DM**, Collins DJ, Wallace T, Chau I, Riddell AM. Combining diffusion-weighted MRI with Gd-EOB-DTPA-enhanced MRI improves the detection of colorectal liver metastases. *Br J Radiol* 2012; **85**: 980-989 [PMID: 22167501 DOI: 10.1259/bjr/91771639]
- 100 **Löwenthal D**, Zeile M, Lim WY, Wybranski C, Fischbach F, Wieners G, Pech M, Kropf S, Ricke J, Dudeck O. Detection and characterisation of focal liver lesions in colorectal carcinoma patients: comparison of diffusion-weighted and Gd-EOB-DTPA enhanced MR imaging. *Eur Radiol* 2011; **21**: 832-840 [PMID: 20886339 DOI: 10.1007/s00330-010-1977-2]
- 101 **Shimada K**, Isoda H, Hirokawa Y, Arizono S, Shibata T, Togashi K. Comparison of gadolinium-EOB-DTPA-enhanced and diffusion-weighted liver MRI for detection of small hepatic metastases. *Eur Radiol* 2010; **20**: 2690-2698 [PMID: 20563726 DOI: 10.1007/s00330-010-1842-3]
- 102 **Donati OF**, Fischer MA, Chuck N, Hunziker R, Weishaupt D, Reiner CS. Accuracy and confidence of Gd-EOB-DTPA enhanced MRI and diffusion-weighted imaging alone and in combination for the diagnosis of liver metastases. *Eur J Radiol* 2013; **82**: 822-828 [PMID: 23287713 DOI: 10.1016/j.ejrad.2012.12.005]
- 103 **Kim YK**, Kim CS, Han YM, Lee YH. Detection of liver malignancy with gadoteric acid-enhanced MRI: is addition of diffusion-weighted MRI beneficial? *Clin Radiol* 2011; **66**: 489-496 [PMID: 21367403 DOI: 10.1016/j.crad.2010.09.007]
- 104 **Goshima S**, Kanematsu M, Kondo H, Yokoyama R, Kajita K, Tsuge Y, Watanabe H, Shiratori Y, Onozuka M, Moriyama N. Diffusion-weighted imaging of the liver: optimizing b value for the detection and characterization of benign and malignant hepatic lesions. *J Magn Reson Imaging* 2008; **28**: 691-697 [PMID: 18777553 DOI: 10.1002/jmri.21467]
- 105 **Battal B**, Kocaoglu M, Akgun V, Karademir I, Deveci S, Guvenc I, Bulakbasi N. Diffusion-weighted imaging in the characterization of focal liver lesions: efficacy of visual assessment. *J Comput Assist Tomogr* 2011; **35**: 326-331 [PMID: 21586924 DOI: 10.1097/RCT.0b013e318216efeb]
- 106 **Gourtsoyianni S**, Papanikolaou N, Yarmenitis S, Maris T, Karantanas A, Gourtsoyiannis N. Respiratory gated diffusion-weighted imaging of the liver: value of apparent diffusion coefficient measurements in the differentiation between most commonly encountered benign and malignant focal liver lesions. *Eur Radiol* 2008; **18**: 486-492 [PMID: 17994317 DOI: 10.1007/s00330-007-0798-4]
- 107 **Namimoto T**, Yamashita Y, Sumi S, Tang Y, Takahashi M. Focal liver masses: characterization with diffusion-weighted echo-planar MR imaging. *Radiology* 1997; **204**: 739-744 [PMID: 9280252 DOI: 10.1148/radiology.204.3.9280252]
- 108 **Kim T**, Murakami T, Takahashi S, Hori M, Tsuda K, Nakamura H. Diffusion-weighted single-shot echoplanar MR imaging for liver disease. *AJR Am J Roentgenol* 1999; **173**: 393-398 [PMID: 10430143 DOI: 10.2214/ajr.173.2.10430143]
- 109 **Cieszanowski A**, Anysz-Grodzicka A, Szeszkowski W, Kaczynski B, Maj E, Gornicka B, Grodzicki M, Grudzinski IP, Stadnik A, Krawczyk M, Rowinski O. Characterization of focal liver lesions using quantitative techniques: comparison of apparent diffusion coefficient values and T2 relaxation times. *Eur Radiol* 2012; **22**: 2514-2524 [PMID: 22699872 DOI: 10.1007/s00330-012-2519-x]
- 110 **Demir OI**, Obuz F, Sağol O, Dicle O. Contribution of diffusion-weighted MRI to the differential diagnosis of hepatic masses. *Diagn Interv Radiol* 2007; **13**: 81-86 [PMID: 17562512]
- 111 **Oner AY**, Celik H, Oktar SO, Tali T. Single breath-hold diffusion-weighted MRI of the liver with parallel imaging: initial experience. *Clin Radiol* 2006; **61**: 959-965 [PMID: 17018309 DOI: 10.1016/j.crad.2006.06.014]
- 112 **Holzappel K**, Bruegel M, Eiber M, Ganter C, Schuster T, Heinrich P, Rummeny EJ, Gaa J. Characterization of small ( $\leq 10$  mm) focal liver lesions: value of respiratory-triggered echo-planar diffusion-weighted MR imaging. *Eur J Radiol* 2010; **76**: 89-95 [PMID: 19501995 DOI: 10.1016/j.ejrad.2009.05.014]
- 113 **Saito K**, Moriyasu F, Sugimoto K, Nishio R, Saguchi T, Akata S, Tokuyue K. Histological grade of differentiation of hepatocellular carcinoma: comparison of the efficacy of diffusion-weighted MRI with T2-weighted imaging and angiography-assisted CT. *J Med Imaging Radiat Oncol* 2012; **56**: 261-269 [PMID: 22697322 DOI: 10.1111/j.1754-9485.2012.02374.x]
- 114 **Nasu K**, Kuroki Y, Tsukamoto T, Nakajima H, Mori K, Minami M. Diffusion-weighted imaging of surgically resected hepatocellular carcinoma: imaging characteristics and relationship among signal intensity, apparent diffusion coefficient, and histopathologic grade. *AJR Am J Roentgenol* 2009; **193**: 438-444 [PMID: 19620441 DOI: 10.2214/AJR.08.1424]

**P- Reviewer:** Bubnov RV, Ferraioli G, Gatselis NK, Waisberg J

**S- Editor:** Kong JX **L- Editor:** A **E- Editor:** Lu YJ



## Sonoelastography in the musculoskeletal system: Current role and future directions

Naomi Winn, Radhesh Lalam, Victor Cassar-Pullicino

Naomi Winn, Radhesh Lalam, Victor Cassar-Pullicino, Department of Radiology, Robert Jones and Agnes Hunt Orthopaedic Hospital NHS Foundation Trust, Oswestry SY10 7AG, United Kingdom

**Author contributions:** Winn N wrote the manuscript; Lalam R and Cassar-Pullicino V critically reviewed the text and images.

**Conflict-of-interest statement:** No potential conflicts of interest. No financial support.

**Open-Access:** This article is an open-access article which was selected by an in-house editor and fully peer-reviewed by external reviewers. It is distributed in accordance with the Creative Commons Attribution Non Commercial (CC BY-NC 4.0) license, which permits others to distribute, remix, adapt, build upon this work non-commercially, and license their derivative works on different terms, provided the original work is properly cited and the use is non-commercial. See: <http://creativecommons.org/licenses/by-nc/4.0/>

**Manuscript source:** Invited manuscript

**Correspondence to:** Dr. Victor Cassar-Pullicino, Department of Radiology, Robert Jones and Agnes Hunt Orthopaedic Hospital NHS Foundation Trust, Gobowen, Oswestry SY10 7AG, United Kingdom. [victor.pullicino@rjah.nhs.uk](mailto:victor.pullicino@rjah.nhs.uk)  
Telephone: +44-1691-404000

Received: June 27, 2016

Peer-review started: June 29, 2016

First decision: August 5, 2016

Revised: August 17, 2016

Accepted: September 7, 2016

Article in press: October 28, 2016

Published online: November 28, 2016

### Abstract

Ultrasound is an essential modality within musculoskeletal imaging, with the recent addition of elastography. The elastic properties of tissues are different from the acoustic impedance used to create B mode imaging

and the flow properties used within Doppler imaging, hence elastography provides a different form of tissue assessment. The current role of ultrasound elastography in the musculoskeletal system will be reviewed, in particular with reference to muscles, tendons, ligaments, joints and soft tissue tumours. The different ultrasound elastography methods currently available will be described, in particular strain elastography and shear wave elastography. Future directions of ultrasound elastography in the musculoskeletal system will also be discussed.

**Key words:** Ultrasound; Elastography; Musculoskeletal system

© **The Author(s) 2016.** Published by Baishideng Publishing Group Inc. All rights reserved.

**Core tip:** This review article describes the different techniques of ultrasound elastography and their current and future role in the musculoskeletal system.

Winn N, Lalam R, Cassar-Pullicino V. Sonoelastography in the musculoskeletal system: Current role and future directions. *World J Radiol* 2016; 8(11): 868-879 Available from: URL: <http://www.wjgnet.com/1949-8470/full/v8/i11/868.htm> DOI: <http://dx.doi.org/10.4329/wjr.v8.i11.868>

### INTRODUCTION

Ultrasound is an essential modality within medical imaging, predominantly for assessing soft tissues. Recently, the additional tool of ultrasound elastography has become commercially available for further assessment of tissues, in addition to the standard B-mode and Doppler imaging. The elastic properties of tissues are different from the acoustic impedance used to create B mode imaging and the flow properties used within Doppler imaging, hence elastography provides a different form of

tissue assessment and possibly showing pathology before it can be detected on B mode imaging. This may be of particular use in the musculoskeletal system where there is a wide spectrum of tissue specialisation. Elastography assesses the strain (stiffness) of these tissues in response to stress, through a variety of different methods which will be discussed.

Throughout history, the stiffness of tissues has been used as a marker of disease, through palpation. Generally, malignant tissues are stiffer or harder than benign tissues, a feature which can be distinguished through direct palpation, corresponding to manual compression. This concept has been extended within the field of ultrasound, with maps of tissue stiffness generated alongside anatomical images.

## PRINCIPLES OF ELASTOGRAPHY

The term elastography was described by Ophir *et al*<sup>[1]</sup> as a method of portraying the strain properties of biological tissue. The strain of a tissue is its response to an applied stress, or pressure, with both longitudinal and shear components. A longitudinal strain occurs when a tissue is compressed or stretched, whilst a shear strain is the response to angular forces, such as twisting. Biological tissues have both viscous (liquid-like) and elastic (solid-like) properties, with a complex interplay between the two given the non-uniform nature of biological tissues. When a stress is applied to fluids, the pressure is the same in all directions, hence shear strain and shear waves do not exist in pure fluids. The Elastic modulus of a material gives an indication of how it responds to a change in applied stress and is defined as the slope of the stress-strain curve. The elastic modulus can be described as either Young's modulus (E) (compressive stress/compressive strain) or the shear modulus (G) (shear stress/shear strain). The bulk modulus is a three dimensional extension of Young's modulus and describes volumetric stress over volumetric strain<sup>[2]</sup>. Young's modulus and shear modulus are the most applicable to biological tissues, with an approximation between them described as  $E \cong 3G$ . The elastic modulus of a tissue is inversely proportional to the strain, *i.e.*, the greater the elastic modulus, the less the tissue strain.

In medical usage, elastography requires the application of a mechanical stress to the tissues and then measurement of the displacement before and immediately after the stress as an estimate of the strain<sup>[3]</sup>. Soft tissues in the body have a high water content and are virtually incompressible, thus sophisticated equipment is necessary to detect small tissue displacements. There are currently two main elastography methods in general clinical usage, namely compression/strain elastography and shear wave elastography.

### Strain elastography

In strain, or compression elastography, a force (*i.e.*, stress) is applied from the transducer by repetitive

manual pressure and the displacement (strain) is calculated from the return velocities of the tissues with respect to time. Motion intrinsic to the subject can also be used as the stress generator, such as aortic pulsation, however this is less useful in the musculoskeletal system where more superficial structures are of interest.

Measuring the displacement (strain) of the tissues secondary to an applied force (stress) gives a qualitative map of the elastic modulus distribution, termed an elastogram. This elastogram is colour-coded and often super-imposed on a grey-scale B mode image for anatomical localisation. True quantitative measures cannot be taken from this elastogram, as the applied force is unknown. A semi-quantitative evaluation, however, can be determined from the ratio of the displacement of the tissue of interest and an adjacent structure, such as subcutaneous fat.

Strain elastography has many potential disadvantages, including the variability in the pressure applied to the tissue. This can be partly compensated for by a graphical representation of the adequacy of the compression, however, the potential for inter-observer and intra-observer variation remains<sup>[4]</sup>. At least three cycles of compression and decompression have been recommended for optimum assessment<sup>[5]</sup>, however, extensive preload of the tissues through repeated compressions can alter tissue elasticity. Thus, enough compression/decompression cycles must be performed to obtain a representative assessment, however, excessive compression may adversely affect the resulting elastograms through pre-loading the tissues. Correct probe alignment is required to compensate for potential out of plane compression of the tissue and anisotropy. Compression along the longitudinal axis of the region of interest has been shown to be optimal as compression in the transverse plane gives rise to artefacts at the medial and lateral sides of the image and out-of-plane movement. Constraints from bony anatomy, such as around the ankle, can also make uniform compression difficult across the region of interest, in particular in the musculoskeletal system.

### Shear wave elastography

Shear wave elastography applies a vibration to tissues through a focussed ultrasound pulse, generated by the transducer. This deposition of energy within the tissues creates transverse waves, or shear waves, which are perpendicular to the push pulse. The shear wave velocities can be measured from Doppler frequency modulation of simultaneously transmitted probing ultrasound waves. Young's modulus can then be estimated as a function of the shear wave velocity. The stiffer the tissue is (the less compliant to shear forces), the faster the propagated shear waves within it<sup>[6]</sup>.

Although shear wave elastography is likely to be more reproducible than strain elastography owing to the standardised applied stress, it still has limitations. Shear waves are attenuated at depth and thus very deep tissues (> 9 cm from the skin) cannot be assessed.

Conversely, an adequate depth of tissue is required in order to generate shear waves, hence very superficial structures are difficult to assess. This can partly be compensated for by using a gel stand-off on the patient. Shear waves are not generated within fluids, thus cystic structures cannot be adequately analysed<sup>[7]</sup>. The size of the region of interest may also potentially affect the shear wave measurements. Similar to strain elastography, the amount of probe pressure applied to the skin has the potential to affect the tissue elasticity, through pre-loading the tissues, as shown in a study assessing muscle elastic properties with shear wave elastography and varying technical parameters<sup>[8]</sup>. Assessment of a tissue in the longitudinal vs transverse plane may potentially affect the shear wave measurements owing to anisotropy, similar to strain elastography. The acoustic radiation force impulse required to generate shear waves deposits energy in the tissues, manifest partly as heating. This should be considered with repeated measurements, as the heating effect may adversely alter the measurements or potentially cause tissue damage. Commercially available systems have an in-built cooling delay in the order of a few seconds, to reduce any potential heating, however, prolonged usage may still heat the tissues and alter the properties of the generated shear waves.

Measured values of shear waves are given as either a velocity in m/s or a stiffness in kPa. The elasticity expressed in kPa can be approximated into shear wave velocity using the equation  $E = 3rc^2$ , where  $E$  is Young modulus,  $r$  is density (estimated at 1000 kg/m<sup>3</sup>), and  $c$  is the speed of sound<sup>[9]</sup>. This method of converting the values is useful in isotropic tissues, such as the breast, however, it may not be applicable to tendons and muscles which are anisotropic, with potential for faster propagation of shear waves along the longitudinal axis of the tendon<sup>[10]</sup>. Thus, caution must be used when comparing values quoted in kPa with m/s as they may not be directly comparable.

A study assessing the differences between two commercially available systems for shear wave elastography has shown that the results in assessing liver stiffness are broadly similar, however, the measurements in kPa vs m/s are not directly interchangeable, thus, the machines should be kept constant if temporal follow-up is required<sup>[11]</sup>. Reference standards for shear wave elastography have been determined in many tissues, including the thyroid, submandibular glands, masseter, gastrocnemius and supraspinatus muscles and the Achilles tendon<sup>[12]</sup>, however these should be used with caution given the potential for poor reproducibility between vendor equipment.

### **Transient elastography**

Another form of elastography currently within the remit of clinical practice is transient elastography, however, its use is generally outside of the musculoskeletal field. Transient elastography generates a single short impulse of energy, from which the generated shear waves are

measured. This is available commercially as a "Fibroscan" for assessing liver fibrosis, but is not currently used in the musculoskeletal system<sup>[13]</sup>.

## **MUSCULOSKELETAL APPLICATIONS OF ELASTOGRAPHY**

### **Muscles**

Skeletal muscles are readily accessible for ultrasound assessment, being superficial in location. Strain elastography has been used to assess many muscle pathologies<sup>[14,15]</sup>, including muscular dystrophy, with a case report showing diseased muscle fibres to be stiffer compared with a normal healthy volunteer<sup>[16]</sup>. In children with cerebral palsy, elastography has been used to guide botulinum toxin injections into contracted muscles, identified as harder on the elastogram<sup>[17]</sup>. In myositis, an alteration in the normal muscle elastogram has been shown, with pathological muscles predominantly appearing harder<sup>[18]</sup>. Within normal muscle, strain elastography has demonstrated greater stiffness in the biceps brachii muscle following exercise compared with pre-exercise elastograms<sup>[19]</sup>. The postulated cause for this is the physiological response to exercise with increased blood flow and capillary permeability. Between three observers, the authors showed good reliability. A further study reported differences in the stiffness of quadriceps muscle in female subjects with patellofemoral pain syndrome compared with healthy controls<sup>[20]</sup>. Elastography has also been used in muscular trauma, showing alteration in the normal elastograms with intra-muscular haemorrhage and fibrosis<sup>[21]</sup>. Both strain and shear wave elastography have been used to assess masseter muscle in healthy volunteers and patients with facial pain<sup>[22-25]</sup>, with good reproducibility between the two techniques. Patients with facial pain and temporomandibular joint dysfunction have been shown to have a greater stiffness in masseter muscle compared with healthy controls. This correlates with the clinical finding of altered hardness of masseter muscle in symptomatic patients with facial pain, thus ultrasound elastography could become a useful adjunct to current techniques in the assessment of these patients<sup>[26]</sup>.

Assessing skeletal muscle with ultrasound elastography, however, has many potential limitations regarding reproducibility. Ensuring a standardised state of contraction/relaxation between assessments is necessary, as is the state of the muscle regarding exercise and rest. Muscles are also subject to anisotropy, so the probe orientation when assessing different muscles must be kept in the same plane (Figure 1). The above factors generate significant challenges with standardisation. In the immediate future elastography alone or in combination with other imaging modalities is unlikely to replace muscle biopsy for the diagnosis of muscular pathologies, namely muscular dystrophy and myositis. The role of elastography in assessing functional muscle disorders is also in its infancy and more research is needed to assess whether it is truly of value or not, given the difficulty with standardisation.

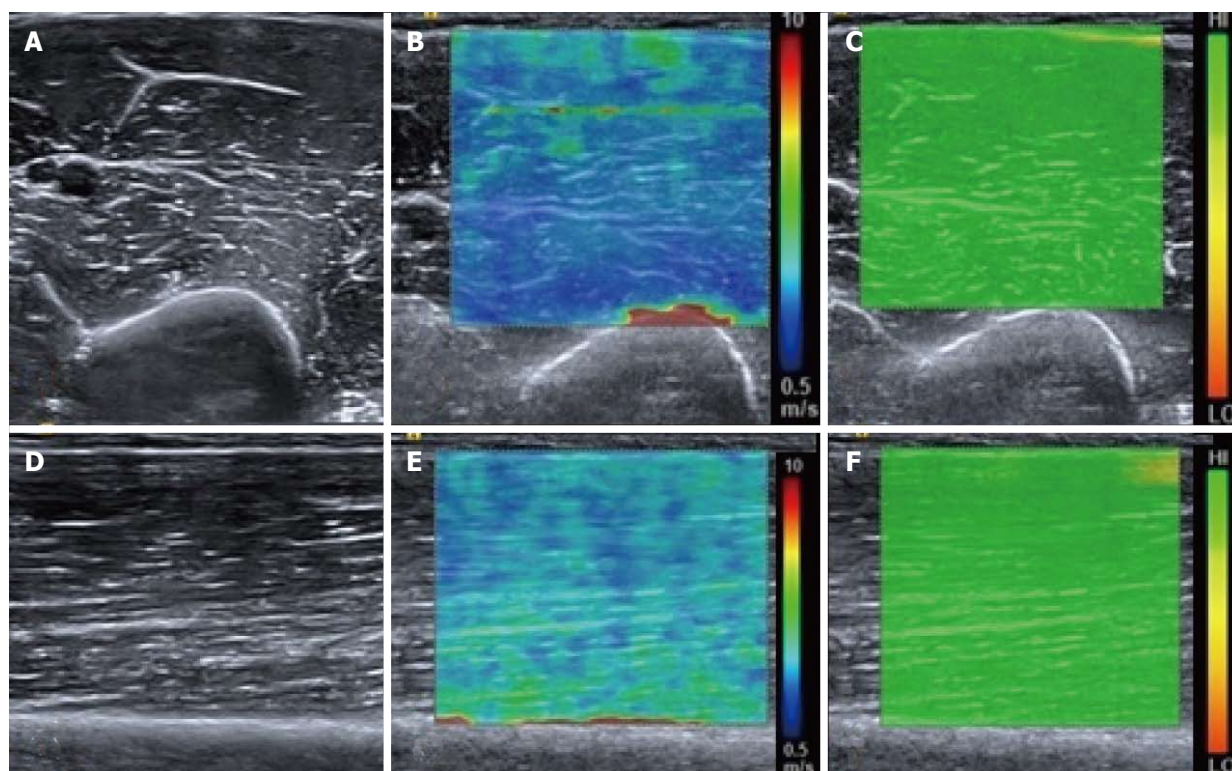


**Figure 1 Normal relaxed biceps brachii muscle.** B mode transverse image of the mid biceps brachii muscle (A) with the corresponding shear wave elastography image (B) showing the shear wave velocity distribution. The velocity map is coloured such that blue represents the slowest waves and red the fastest, illustrated by the scale. Note the fast (red colour) shear waves at the interface with the hard humeral bone. A range of shear wave velocities are seen at the fascial interfaces within the muscle belly. The upper right image (C) shows the quality map with green colouring representing a high quality elastogram. Corresponding longitudinal B mode image of the mid biceps brachii muscle (D), shear wave velocity image (E) and quality map (F). The velocity distribution is slightly different in the longitudinal plane compared with the transverse plane owing to the greater effect of anisotropy in the transverse plane compared with the longitudinal plane.

### Tendons

Elastography allows the possibility of assessing tendons for mucoid degeneration or small interstitial tears potentially before they become apparent on conventional B-mode imaging. When tendons degenerate, the collagen fibres break down and it is proposed that tendons become softer<sup>[27]</sup>, thus a change in their elasticity can be detected with elastography. Conversely, if a tendon repairs with fibrosis, this may be seen as a hardening of the tendon substance, with a stiffer elastographic picture.

The Achilles tendon has received the most attention within elastography studies owing to its ease of accessibility, relatively large size and susceptibility to pathology. It is composed of tightly packed collagen fibres which appear as hypochoic on B-mode ultrasound with areas of increased reflectivity corresponding to linear interfaces. In symptomatic Achilles tendons there is a disorganisation and breakdown of the collagen fibres, corresponding to mucoid degeneration, and it is proposed that this leads to a softer tendon structure compared with normal<sup>[28]</sup>. This is shown as alteration in the B-mode architecture, mainly as regions of hypochoic within the tendon substance. The corresponding strain elastography images often show softer regions within the tendon in these areas<sup>[29-31]</sup>. In patients with surgically repaired Achilles tendons, the regenerative tissue has

been shown to be harder and more heterogeneous compared with healthy controls, indicating the reparative tissue to be firmer than normal tendon tissue<sup>[30]</sup>. Furthermore, patients with ankylosing spondylitis have been shown to have changes in tendon elasticity in strain elastography correlating with B-mode changes, with a difference compared with healthy controls<sup>[32]</sup>.

Shear wave elastography has also been used to study the Achilles tendon. Slower shear wave velocities have been demonstrated in tendinopathic tendons compared with healthy controls<sup>[33]</sup>, also suggesting a softer tendon substance in pathology (Figure 2). As described previously, shear wave elastography measurements are not necessarily comparable between different manufacturers' equipment, thus potentially limiting the reproducibility. This is evidenced by the large range of quoted normal shear wave values for the Achilles tendon within healthy subjects<sup>[34]</sup>.

The reproducibility of shear wave elastography has been assessed in tendons with *in vivo* and *in vitro* testing. In a study from 2013, repeatability was found to be better in the *in vitro* setting compared with *in vivo*, most likely because the *in vitro* conditions were more amenable to standardisation<sup>[35]</sup>. Also, the assessed tendon outside the body is static, compared with potential for movement and assessing a different position along the tendon or

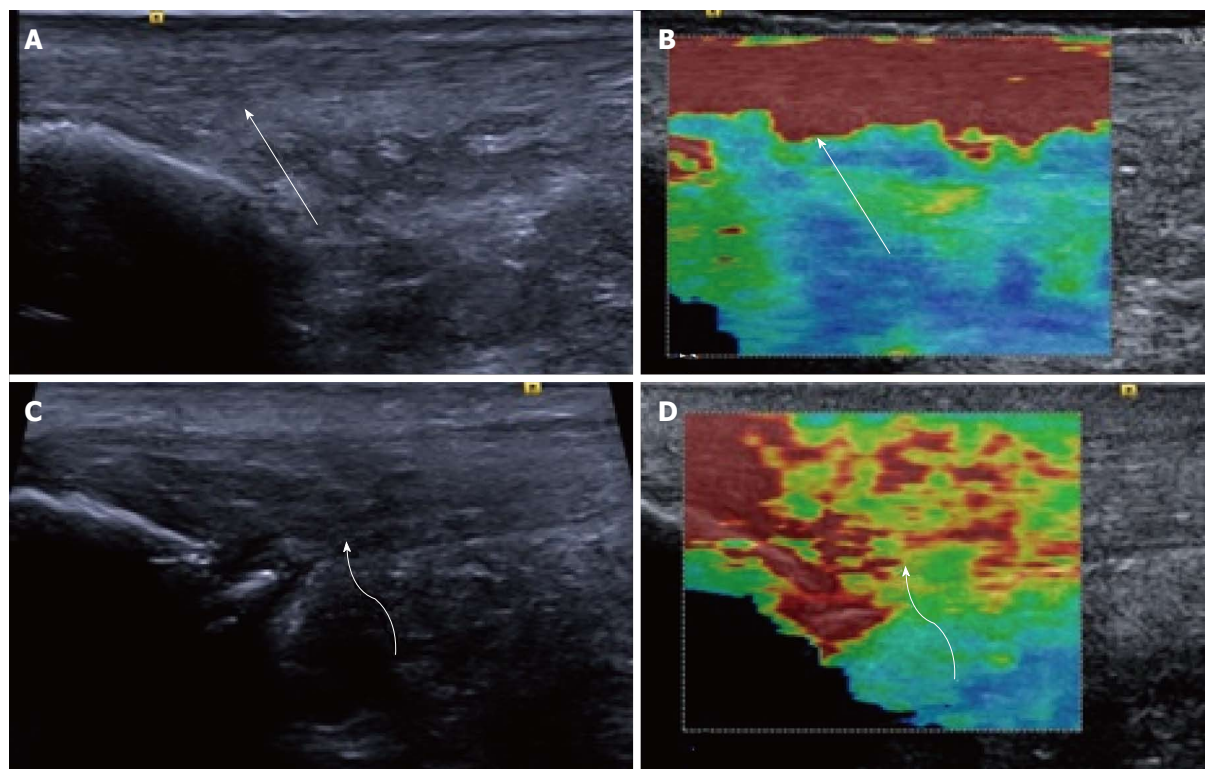


**Figure 2** Longitudinal shear wave elastography of the Achilles tendon. In a healthy volunteer the Achilles tendon is seen as smooth and homogeneous (arrow) on the B mode image (A) with a homogeneous elastogram (B, arrow). In a patient with symptomatic Achilles tendinopathy there is an alteration of the B mode echotexture with regions of hypoechogenicity (C, curved arrow) and dystrophic ossification at the calcaneal enthesis. The elastogram (D) is heterogeneous with regions of blue and yellow colouring (curved arrow) corresponding to a slower velocity and tendon softening.

different probe orientation in human subjects compared with laboratory conditions. A different *in vitro* study of harvested equine tendons and strain elastography showed poor repeatability between experiments, reflecting the more variable nature of strain elastography compared with shear wave elastography<sup>[36]</sup>.

Away from the Achilles tendon, ultrasound elastography has been used to assess supraspinatus muscle and tendon (Figure 3), with tendinosis predominantly being shown as tendon softening, but also regions of increased stiffness, purported to represent reparative fibrosis (Figures 4 and 5)<sup>[37-39]</sup>. Strain elastography has also been used around the elbow to assess the common extensor tendon. In a study comparing healthy volunteers with those who were symptomatic, the symptomatic common extensor tendons were shown to be softer compared with healthy volunteers<sup>[40]</sup>.

Thus, within the tendons the predominant elastographic picture of mucoid degeneration/tendinosis is softening, however, some studies have shown tendinosis as increased tendon stiffness, making a general statement of the elastic properties of tendinosis problematic. The future role of elastography may therefore be to identify areas that have a heterogeneous, disordered elastogram (either softening or hardening) corresponding to tendinosis, rather than the homogeneous elastogram of a normal tendon. This may allow preclinical detection of pathology, potentially of relevance to athletes allowing

an alteration in training before injuries occur, or as a screening tool prior to any sporting commitments. Further research is also needed to ascertain if the changes identified on elastography resolve following treatment, or if the tendon becomes asymptomatic. If this were known, then potentially the appearances of a tendon on elastography could be used for prognosis to try and predict the time for tendon healing. Additionally, the elastograms of asymptomatic people of different ages has not been fully characterised and it is not known if the normal ageing process gives rise to different tendon stiffness, or the relevance of alterations in the elastograms in asymptomatic individuals.

### **Fascia and ligaments**

A recent prospective study has shown that the coracohumeral ligament is stiffer in patients with adhesive capsulitis compared with their unaffected contralateral shoulder. Interestingly, this study also demonstrated variations in the stiffness of the ligament depending on the degree of external rotation of the arm<sup>[41]</sup>. This is an exciting development, potentially adding additional criteria for diagnosing adhesive capsulitis in addition to the thickness of the coracohumeral ligament.

Within the plantar fascia, a study using strain elastography found the plantar fascia in symptomatic patients to be thicker and more hypoechoic compared with controls, correlating with a loss of elasticity, or a harder

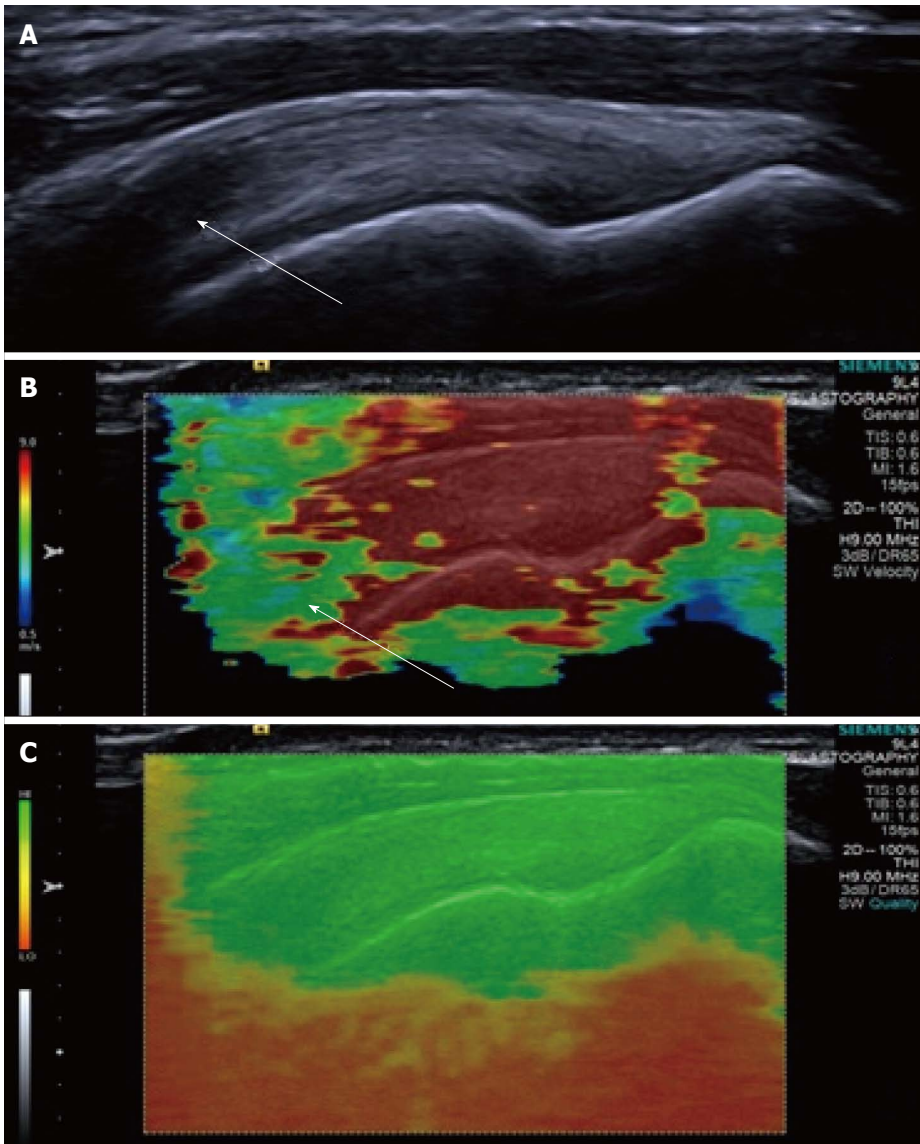


**Figure 3** Longitudinal shear wave elastography of a normal supraspinatus tendon. Normal B mode appearances (A) showing anisotropy (arrow) owing to the curved orientation of the tendon. The corresponding elastogram (B) shows heterogeneous stiffness at the region of anisotropy (arrow) and absence of measurements from deep in the humeral head. The quality map (C) shows a high quality elastogram in the tendon substance and poor quality in the bone, as would be expected for such a stiff structure with limited propagation of shear waves.

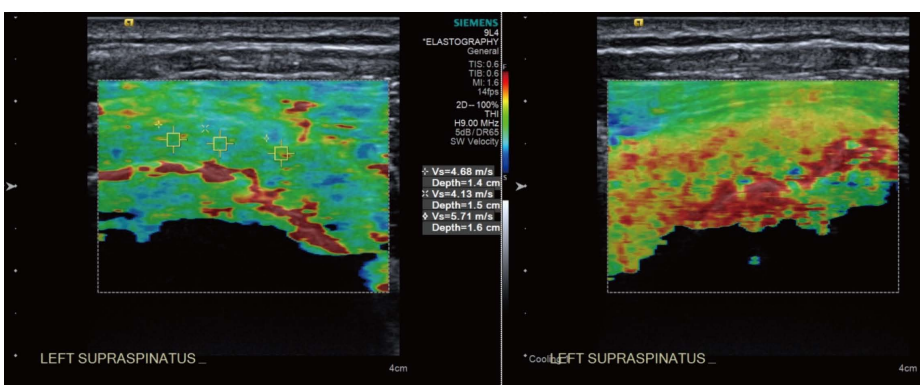


**Figure 4** Longitudinal shear wave elastography of a tendinopathic supraspinatus tendon showing a disorganised, heterogeneous pattern, contrasted to the homogeneous appearance of the normal tendon in Figure 3. Note the regions of interest (small boxes) where shear wave velocity measurements have been taken.

fascia<sup>[42]</sup>.

A further study looking at the stiffness of the A1 pulley in patients with trigger finger showed the pulley to be stiffer in symptomatic patients<sup>[43]</sup>, corresponding with changes in the B-mode appearances too. A further preliminary study has assessed the transverse carpal ligament in the carpal tunnel and the effects of probe pressure on the resultant shear wave velocities.

Variations were identified according to the applied probe pressure, indicating that the technique is still somewhat operator dependent<sup>[44]</sup>. The small size of the finger pulleys and carpal ligaments also significantly limits the use of this technique as the resolution of these small structures can be less than the resolution of the elastograms, particularly with regard to the region of interest for measurement of shear wave velocities within

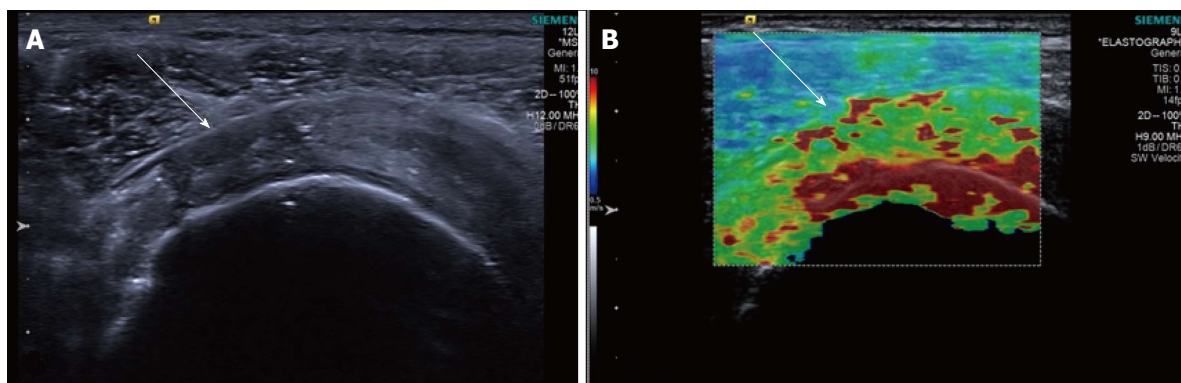


**Figure 5** Longitudinal shear wave elastography of a tendinopathic supraspinatus tendon in a different patient to Figure 4. The B mode image (A) shows a partial thickness tear involving the bursal surface fibres (arrow). The corresponding velocity elastogram (B) shows a disorganised pattern with the tear less well delineated (arrow) compared with the B mode image.

the currently available equipment.

### Carpal tunnel

The median nerve at the wrist has been studied with both shear wave elastography and strain elastography<sup>[45]</sup>. Using strain elastography, the median nerve in patients with carpal tunnel syndrome has been shown to be stiffer compared with controls<sup>[46]</sup>. These findings are also replicated with shear wave elastography, with a greater shear wave stiffness shown in patients with carpal tunnel syndrome compared with controls<sup>[47]</sup>. Thus elastography is a useful addition to the B mode appearances and the cross sectional area of the median nerve in diagnosing carpal tunnel syndrome, with potential to replace nerve conduction studies as the diagnostic gold standard.

### Joints

Very little information is available on elastography of the joints, in particular, the synovium. To date, there are no published clinical trials assessing elastography in the joints. Case reports of strain elastography in a small number of patients suggests that inflammatory synovitis may appear as firm, compared with infective synovitis which may appear as firm to soft. Thus, there is overlap in the elastographic appearances between infective and inflammatory synovitis and the technique is unable to replace the gold standard of tissue diagnosis for either infective or inflammatory synovitis<sup>[48,49]</sup>.

There is no data published on the elastographic appearances of the synovium in normal subjects vs those with an inflammatory arthropathy (Figure 6). This is an area requiring further research, to determine if elastography can be as useful a tool as Doppler in the assessment of suspected inflammatory synovitis and potential response to disease modifying anti-rheumatic therapies.

### Tumours

Elastography in tumours has been used extensively outside the musculoskeletal system, predominantly within breast, thyroid and prostate lesions. Within the breast, elastography is proving to be useful to help

differentiate between benign and malignant lesions (including threshold values for shear wave velocities in malignant lesions) however, within the thyroid there is significant overlap in the elastographic characteristics between the two.

In musculoskeletal soft tissue tumours, elastography has been used to prospectively assess lesions to attempt to differentiate between benign and malignant pathologies. Malignant lesions have been shown to be stiffer on strain elastography compared with benign lesions on a semi-quantitative scale, similar to lesions outside of the musculoskeletal system<sup>[50]</sup>. However, a recently published study by the group in Leeds assessing the role of shear wave elastography in musculoskeletal tumours has been unable to replicate these early findings, with the authors concluding that there is currently no additional role for shear wave elastography in soft tissue tumours compared with B mode imaging<sup>[51]</sup>. The authors found no statistically significant association between shear wave velocity and malignancy. According to the strain elastography study, one may have expected malignant tumours to be stiffer than benign tumours and thus have a tendency for higher shear wave velocities. Possibly the discordant results are accounted for by the tumour case mix, different elastography technique or study design. Soft tissue tumours are very heterogeneous on B mode imaging (Figure 7) compared with breast lesions and it is probable that further studies will replicate the findings of the Leeds group, showing a large overlap in the shear wave velocity measurements between benign and malignant soft tissue lesions. In the immediate future imaging characteristics alone, even with the addition of elastography, are unlikely to replace biopsy for the diagnosis of malignant vs benign lesions. Similar to tendons, the role of elastography in soft tissue tumours is likely to be in identifying a heterogeneous, disorganised internal substance suggesting an aggressive nature or de-differentiation, vs a smooth homogeneous pattern of a non-aggressive lesion. This could be used to guide biopsy by potentially identifying aggressive regions within a lesion, or to identify malignant degeneration in a previously diagnosed benign lesion.

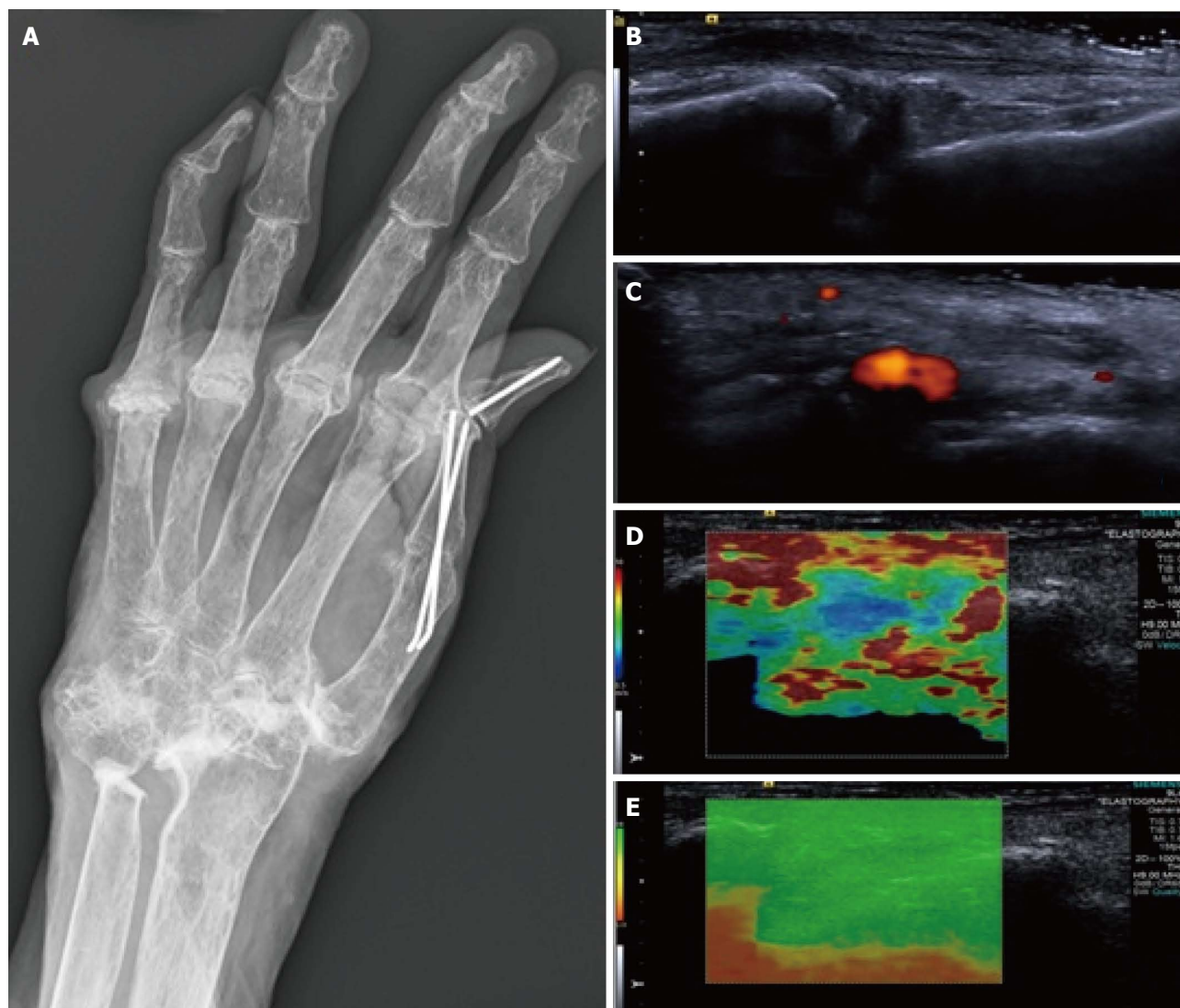


**Figure 6 Synovitis at the carpus.** Radiograph (A) in a patient with long-standing rheumatoid arthritis and worsening wrist pain. The longitudinal B mode image (B) and colour Doppler image (C) show hypoechoogenicity of the synovium with increased Doppler flow indicating an active synovitis. The corresponding longitudinal shear wave velocity elastogram (D) shows relatively uniformly soft synovium (blue colour) compared with the adjacent tissues which are more heterogeneous in their stiffness. The significance of this has not yet been adequately investigated. The elastogram is of good quality (E).

Another potential use of elastography in tumours may be to define the boundaries of a lesion, compared with normal tissue. In regions with poor B-mode contrast it can be hard to identify the margin of a lesion, however, the elastogram may show a sharp demarcation if the lesion has different elastic properties compared with the adjacent normal tissue (Figure 8). This is of value within breast<sup>[52]</sup> and prostate lesions and may prove to be the most useful application of elastography in soft tissue tumours.

## ELASTOGRAPHY OUTSIDE THE MUSCULOSKELETAL SYSTEM

Elastography has been extensively used in structures outside the musculoskeletal system, namely the liver, breast, thyroid and prostate<sup>[53-60]</sup>. Within the liver, it has now become standard in the assessment of fibrosis,

replacing biopsy in many instances. In the breast, thyroid and prostate, elastography has become part of the non-invasive assessment of a lesion, being used in addition to the B mode and Doppler characteristics<sup>[61-63]</sup>. Generally, aggressive cancers with more malignant features have been shown to have a greater stiffness as measured by shear wave elastography compared with less aggressive tumours<sup>[64]</sup>. However, despite the recent advances in tumour characterisation with elastography and other imaging parameters, the gold standard of biopsy has not yet been replaced by imaging alone for the majority of lesions and it this is unlikely to be the case in the near future.

## FUTURE DIRECTIONS

### Technical

As with all technological advances, time will bring refinements in the current technology, perhaps allowing

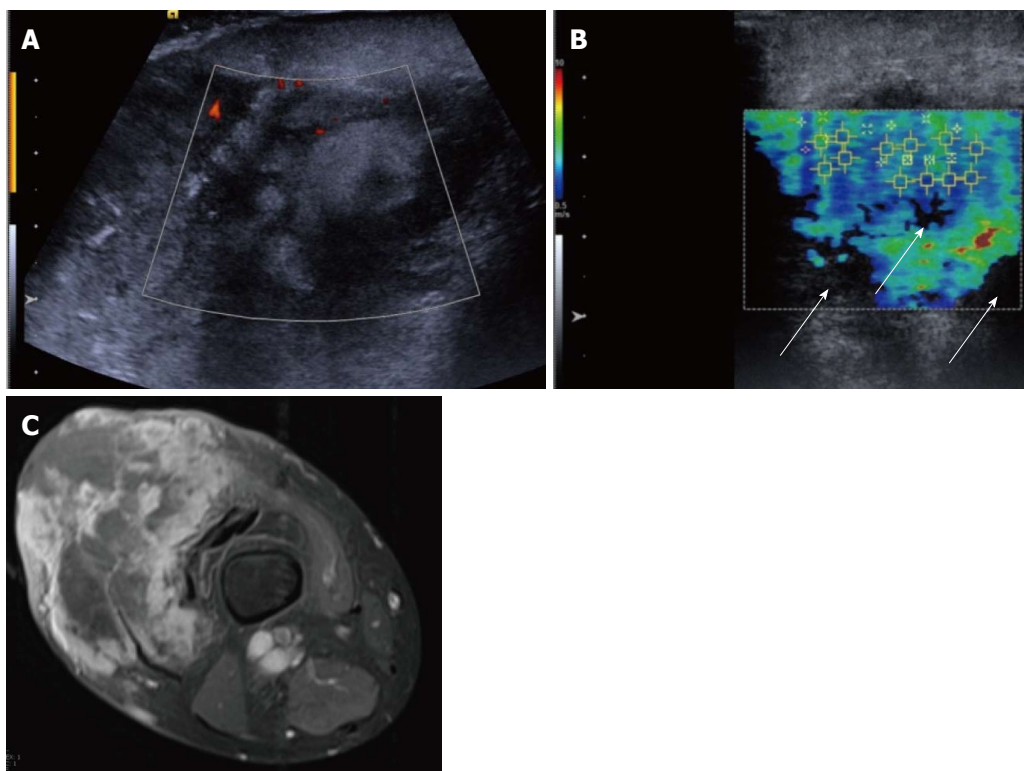


**Figure 7 Pleomorphic sarcoma of the distal thigh.** Transverse B mode image with colour Doppler (A) shows a disorganised tumour with wide variation in echotexture and limited Doppler flow. The shear wave velocity elastogram (B) also shows a wide variation in stiffness with some regions of absent measurements, seen as the black areas on the image (arrow), possibly owing to the very dense/stiff nature of the tumour. The axial proton density fat suppressed magnetic resonance image (C) shows a large tumour in the anterior compartment of the thigh with very varied signal.

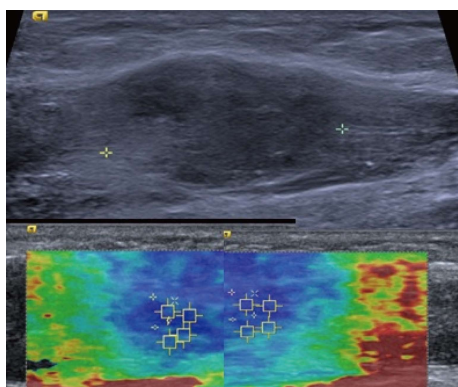


**Figure 8 Intramuscular nodular fasciitis, longitudinal images.** The B mode image (upper image) shows that the margins of the lesion are poorly defined and relatively hard to discern. The shear wave velocity elastograms (lower images) show a clear difference in stiffness between the lesion and adjacent normal muscle fibres, as shown by the blue (slow) colour map of the lesion compared with the green and red (faster) colour map of the adjacent muscle fibres.

shear wave measurements at greater depths, or within very superficial structures such as skin.

Elastography adds another facet to the available ultrasound capabilities and may potentially be fused with other imaging modalities, namely CT and MRI. This could then create a navigable data set to aid with surgical planning or to guide tumour resection, particularly with reference to tumour margins.

### Clinical applications

Within the musculoskeletal system ultrasound elastography has the potential to become as valuable a tool as within the liver, breast and thyroid. It may allow identification of preclinical tendinosis and thus modification of activity or prophylactic treatment prior to symptoms developing. It could be used to predict time to recovery following treatment and help guide the timing of return to activity, once the tendon elastogram returns to normal.

Elastography could ultimately obviate the need for biopsy in soft tissue tumours enabling differentiation between benign and malignant lesions, although as described above, further research is needed. Following tumour resection it may help distinguish post-surgical scarring from recurrent tumour, with the scarring being harder and more homogeneous than tumour.

Elastography could possibly be used to assess the state of cartilage in areas accessible to the ultrasound probe, such as the shoulder and talar dome. Cartilage which is degenerate may display different elastic properties, similar to DGEMRIC and T2 rho magnetic resonance imaging (MRI), thus providing a cheaper alternative to MRI. Within the synovium, if the synovitis of inflammatory arthropathies displays reliable alterations in elasticity compared with normal synovium, it may form part of the routine assessment and synovitis grading, similar to power Doppler.

Within current parameters, elastography data from bone is limited as it is virtually incompressible. If the technology could be refined to detect even the smallest deformation in bone or fracture callus, it could potentially be used to assess when a fracture callus has matured enough to withstand weight-bearing, or to similarly assess the fusion mass following spinal surgery.

## CONCLUSION

Ultrasound elastography is an exciting new development within clinical practice. Strain elastography has created maps of tissue stiffness, in addition to the B mode and Doppler characteristics. The arrival of shear wave elastography has brought a quantitative assessment to elastography and introduced a technique which is potentially less operator dependent compared with strain elastography. The use of ultrasound elastography in the musculoskeletal system is likely to become as widespread as within the liver, breast and thyroid now that more clinical departments have access to this technology. With greater clinical usage and research, its applications will be verified, validated and widened. However in the immediate future the role of ultrasound elastography is likely to be complementary to conventional imaging techniques in providing an additional tool, rather than replacing anything that is current standard practice.

## REFERENCES

- Ophir J, Alam SK, Garra BS, Kallel F, Konofagou EE, Krouskop T, Merritt CR, Righetti R, Souchon R, Srinivasan S, Varghese T. Elastography: Imaging the elastic properties of soft tissues with ultrasound. *J Med Ultrason* (2001) 2002; **29**: 155 [PMID: 27277961 DOI: 10.1007/BF02480847]
- Gennisson JL, Defieux T, Fink M, Tanter M. Ultrasound elastography: principles and techniques. *Diagn Interv Imaging* 2013; **94**: 487-495 [PMID: 23619292 DOI: 10.1016/j.diii.2013.01.022]
- Taylor LS, Porter BC, Rubens DJ, Parker KJ. Three-dimensional sonoelastography: principles and practices. *Phys Med Biol* 2000; **45**: 1477-1494 [PMID: 10870705]
- Drakonaki EE, Allen GM, Wilson DJ. Ultrasound elastography for musculoskeletal applications. *Br J Radiol* 2012; **85**: 1435-1445 [PMID: 23091287 DOI: 10.1259/bjr/93042867]
- Klauser AS, Faschingbauer R, Jaschke WR. Is sonoelastography of value in assessing tendons? *Semin Musculoskelet Radiol* 2010; **14**: 323-333 [PMID: 20539957 DOI: 10.1055/s-0030-1254521]
- Benson J. Understanding ARFI and New Elastography Quantification Technologies. Available from: URL: <http://usa.healthcare.siemens.com/ultrasound/understanding-arfi>
- Elkateb Hachemi M, Callé S, Remenieras JP. Transient displacement induced in shear wave elastography: comparison between analytical results and ultrasound measurements. *Ultrasonics* 2006; **44** Suppl 1: e221-e225 [PMID: 16843510 DOI: 10.1016/j.ultras.2006.06.022]
- Kot BC, Zhang ZJ, Lee AW, Leung VY, Fu SN. Elastic modulus of muscle and tendon with shear wave ultrasound elastography: variations with different technical settings. *PLoS One* 2012; **7**: e44348 [PMID: 22952961 DOI: 10.1371/journal.pone.0044348]
- Youk JH, Son EJ, Park AY, Kim JA. Shear-wave elastography for breast masses: local shear wave speed (m/sec) versus Young modulus (kPa). *Ultrasonography* 2014; **33**: 34-39 [PMID: 24936493 DOI: 10.14366/usg.13005]
- Brum J, Bernal M, Gennisson JL, Tanter M. In vivo evaluation of the elastic anisotropy of the human Achilles tendon using shear wave dispersion analysis. *Phys Med Biol* 2014; **59**: 505-523 [PMID: 24434420 DOI: 10.1088/0031-9155/59/3/505]
- Woo H, Lee JY, Yoon JH, Kim W, Cho B, Choi BI. Comparison of the Reliability of Acoustic Radiation Force Impulse Imaging and Supersonic Shear Imaging in Measurement of Liver Stiffness. *Radiology* 2015; **277**: 881-886 [PMID: 26147680 DOI: 10.1148/radiol.2015141975]
- Arda K, Ciledag N, Aribas BK, Aktas E, Köse K. Quantitative assessment of the elasticity values of liver with shear wave ultrasonographic elastography. *Indian J Med Res* 2013; **137**: 911-915 [PMID: 23760376 DOI: 10.2214/AJR.10.5449]
- Barr RG, Ferraioli G, Palmeri ML, Goodman ZD, Garcia-Tsao G, Rubin J, Garra B, Myers RP, Wilson SR, Rubens D, Levine D. Elastography Assessment of Liver Fibrosis: Society of Radiologists in Ultrasound Consensus Conference Statement. *Ultrasound Q* 2016; **32**: 94-107 [PMID: 27233069 DOI: 10.1097/RUQ.0000000000000209]
- Ehy SF, Song P, Chen S, Chen Q, Greenleaf JF, An KN. Validation of shear wave elastography in skeletal muscle. *J Biomech* 2013; **46**: 2381-2387 [PMID: 23953670 DOI: 10.1016/j.jbiomech.2013.07.033]
- Yoshitake Y, Takai Y, Kanehisa H, Shinohara M. Muscle shear modulus measured with ultrasound shear-wave elastography across a wide range of contraction intensity. *Muscle Nerve* 2014; **50**: 103-113 [PMID: 24155045 DOI: 10.1002/mus.24104]
- Drakonaki EE, Allen GM. Magnetic resonance imaging, ultrasound and real-time ultrasound elastography of the thigh muscles in congenital muscle dystrophy. *Skeletal Radiol* 2010; **39**: 391-396 [PMID: 20205351 DOI: 10.1007/s00256-009-0861-0]
- Vasilescu D, Vasilescu D, Ducea S, Botar-Jid C, Sfrângeu S, Cosma D. Sonoelastography contribution in cerebral palsy spasticity treatment assessment, preliminary report: a systematic review of the literature apropos of seven patients. *Med Ultrason* 2010; **12**: 306-310 [PMID: 21210016]
- Botar-Jid C, Damian L, Ducea SM, Vasilescu D, Rednic S, Badea R. The contribution of ultrasonography and sonoelastography in assessment of myositis. *Med Ultrason* 2010; **12**: 120-126 [PMID: 21173939]
- Yanagisawa O, Niitsu M, Kurihara T, Fukubayashi T. Evaluation of human muscle hardness after dynamic exercise with ultrasound real-time tissue elastography: a feasibility study. *Clin Radiol* 2011; **66**: 815-819 [PMID: 21529793 DOI: 10.1016/j.crad.2011.03.012]
- Botanlioglu H, Kantarci F, Kaynak G, Unal Y, Ertan S, Aydingoz O, Erginer R, Unlu MC, Mihmanli I, Babacan M. Shear wave elastography properties of vastus lateralis and vastus medialis obliquus muscles in normal subjects and female patients with patellofemoral pain syndrome. *Skeletal Radiol* 2013; **42**: 659-666 [PMID: 22996306 DOI: 10.1007/s00256-012-1520-4]
- Botar Jid C, Vasilescu D, Damian L, Dumitriu D, Ciurea A, Ducea SM. Musculoskeletal sonoelastography. Pictorial essay. *Med Ultrason* 2012; **14**: 239-245 [PMID: 22957331]
- Nakayama M, Arijii Y, Nishiyama W, Arijii E. Evaluation of the masseter muscle elasticity with the use of acoustic coupling agents as references in strain sonoelastography. *Dentomaxillofac Radiol* 2015; **44**: 20140258 [PMID: 25411712 DOI: 10.1259/dmfr.20140258]
- Arijii Y, Nakayama M, Nishiyama W, Nozawa M, Arijii E. Shear-wave sonoelastography for assessing masseter muscle hardness in comparison with strain sonoelastography: study with phantoms and healthy volunteers. *Dentomaxillofac Radiol* 2016; **45**: 20150251 [PMID: 26624000 DOI: 10.1259/dmfr.20150251]
- Arijii Y, Gotoh A, Hiraiwa Y, Kise Y, Nakayama M, Nishiyama W, Sakuma S, Kurita K, Arijii E. Sonographic elastography for evaluation of masseter muscle hardness. *Oral Radiol* 2013; **29**: 64-69 [DOI: 10.1007/s11282-012-0111-3]
- Arijii Y, Nakayama M, Taguchi A, Gotoh A, Kise Y, Katsumata A, Kurita K, Arijii E. Intramuscular changes of soft and hard areas after low-level static contraction of the masseter muscle and the correlations with muscle hardness and increase in water content: evaluations with sonographic elastography and magnetic resonance imaging. *Oral Surg Oral Med Oral Pathol Oral Radiol* 2013; **116**: 354-361 [PMID: 23953421 DOI: 10.1016/j.oooo.2013.05.017]
- Kashima K, Igawa K, Maeda S, Sakoda S. Analysis of muscle

- hardness in patients with masticatory myofascial pain. *J Oral Maxillofac Surg* 2006; **64**: 175-179 [PMID: 16413887 DOI: 10.1016/j.joms.2005.10.012]
- 27 **Sharma P**, Maffulli N. Biology of tendon injury: healing, modeling and remodeling. *J Musculoskelet Neuronal Interact* 2006; **6**: 181-190 [PMID: 16849830]
- 28 **Kader D**, Saxena A, Movin T, Maffulli N. Achilles tendinopathy: some aspects of basic science and clinical management. *Br J Sports Med* 2002; **36**: 239-249 [PMID: 12145112]
- 29 **De Zordo T**, Chhem R, Smekal V, Feuchtner G, Reindl M, Fink C, Faschingbauer R, Jaschke W, Klauser AS. Real-time sonoelastography: findings in patients with symptomatic achilles tendons and comparison to healthy volunteers. *Ultraschall Med* 2010; **31**: 394-400 [PMID: 19946833 DOI: 10.1055/s-0028-1109809]
- 30 **Tan S**, Kudaş S, Özcan AS, İpek A, Karaoğlanoğlu M, Arslan H, Bozkurt M. Real-time sonoelastography of the Achilles tendon: pattern description in healthy subjects and patients with surgically repaired complete ruptures. *Skeletal Radiol* 2012; **41**: 1067-1072 [PMID: 22167230 DOI: 10.1007/s00256-011-1339-4]
- 31 **Ooi CC**, Schneider ME, Malliaras P, Counsel P, Connell DA. Prevalence of morphological and mechanical stiffness alterations of mid Achilles tendons in asymptomatic marathon runners before and after a competition. *Skeletal Radiol* 2015; **44**: 1119-1127 [PMID: 25787114 DOI: 10.1007/s00256-015-2132-6]
- 32 **Turan A**, Tufan A, Mercan R, Teber MA, Tezcan ME, Bitik B, Goker B, Haznedaroğlu S. Real-time sonoelastography of Achilles tendon in patients with ankylosing spondylitis. *Skeletal Radiol* 2013; **42**: 1113-1118 [PMID: 23685710 DOI: 10.1007/s00256-013-1637-0]
- 33 **Aubry S**, Nueffer JP, Tanter M, Becce F, Vidal C, Michel F. Viscoelasticity in Achilles tendonopathy: quantitative assessment by using real-time shear-wave elastography. *Radiology* 2015; **274**: 821-829 [PMID: 25329764 DOI: 10.1148/radiol.14140434]
- 34 **Chen XM**, Cui LG, He P, Shen WW, Qian YJ, Wang JR. Shear wave elastographic characterization of normal and torn achilles tendons: a pilot study. *J Ultrasound Med* 2013; **32**: 449-455 [PMID: 23443185]
- 35 **Peltz CD**, Haladik JA, Divine G, Siegal D, van Holsbeeck M, Bey MJ. ShearWave elastography: repeatability for measurement of tendon stiffness. *Skeletal Radiol* 2013; **42**: 1151-1156 [PMID: 23640400 DOI: 10.1007/s00256-013-1629-0]
- 36 **Buck AR**, Verstraete N, Li Y, Schweizer A, Snedeker JG, Buck FM. Detection of small tendon lesions by sonoelastographic visualization of strain profile differences: initial experiences. *Skeletal Radiol* 2012; **41**: 1073-1079 [PMID: 22218832 DOI: 10.1007/s00256-011-1349-2]
- 37 **Liu J**, Zhan W, Zhou M, Zhang X. Ultrasound elastography of the supraspinatus tendon guided by US-MRI virtual navigation. *Technol Health Care* 2015; **23** Suppl 2: S263-S268 [PMID: 26410491 DOI: 10.3233/THC-150961]
- 38 **Muraki T**, Ishikawa H, Morise S, Yamamoto N, Sano H, Itoi E, Izumi S. Ultrasound elastography-based assessment of the elasticity of the supraspinatus muscle and tendon during muscle contraction. *J Shoulder Elbow Surg* 2015; **24**: 120-126 [PMID: 25017314 DOI: 10.1016/j.jse.2014.04.012]
- 39 **Roskopf AB**, Ehmann C, Buck FM, Gerber C, Flück M, Pfirmann CW. Quantitative Shear-Wave Elastography of the Supraspinatus Muscle: Reliability of the Method and Relation to Tendon Integrity and Muscle Quality. *Radiology* 2016; **278**: 465-474 [PMID: 26540450 DOI: 10.1148/radiol.2015150908]
- 40 **De Zordo T**, Lill SR, Fink C, Feuchtner GM, Jaschke W, Bellmann-Weiler R, Klauser AS. Real-time sonoelastography of lateral epicondylitis: comparison of findings between patients and healthy volunteers. *AJR Am J Roentgenol* 2009; **193**: 180-185 [PMID: 19542412 DOI: 10.2214/AJR.08.2020]
- 41 **Wu CH**, Chen WS, Wang TG. Elasticity of the Coracohumeral Ligament in Patients with Adhesive Capsulitis of the Shoulder. *Radiology* 2016; **278**: 458-464 [PMID: 26323030 DOI: 10.1148/radiol.2015150888]
- 42 **Sconfienza LM**, Silvestri E, Orlandi D, Fabbro E, Ferrero G, Martini C, Sardanelli F, Cimmino MA. Real-time sonoelastography of the plantar fascia: comparison between patients with plantar fasciitis and healthy control subjects. *Radiology* 2013; **267**: 195-200 [PMID: 23297327 DOI: 10.1148/radiol.12120969]
- 43 **Miyamoto H**, Miura T, Isayama H, Masuzaki R, Koike K, Ohe T. Stiffness of the first annular pulley in normal and trigger fingers. *J Hand Surg Am* 2011; **36**: 1486-1491 [PMID: 21802865 DOI: 10.1016/j.jhssa.2011.05.038]
- 44 **Shen ZL**, Vince DG, Li ZM. In vivo study of transverse carpal ligament stiffness using acoustic radiation force impulse (ARFI) imaging. *PLoS One* 2013; **8**: e68569 [PMID: 23861919 DOI: 10.1371/journal.pone.0068569]
- 45 **McDonagh C**, Alexander M, Kane D. The role of ultrasound in the diagnosis and management of carpal tunnel syndrome: a new paradigm. *Rheumatology* (Oxford) 2015; **54**: 9-19 [PMID: 25118315 DOI: 10.1093/rheumatology/keu275]
- 46 **Miyamoto H**, Halpern EJ, Kastlunger M, Gabl M, Arora R, Bellmann-Weiler R, Feuchtner GM, Jaschke WR, Klauser AS. Carpal tunnel syndrome: diagnosis by means of median nerve elasticity—improved diagnostic accuracy of US with sonoelastography. *Radiology* 2014; **270**: 481-486 [PMID: 24471391 DOI: 10.1148/radiol.13122901]
- 47 **Kantarci F**, Ustabasioglu FE, Delil S, Olgun DC, Korkmaz B, Dikici AS, Tutar O, Nalbantoglu M, Uzun N, Mihmanli I. Median nerve stiffness measurement by shear wave elastography: a potential sonographic method in the diagnosis of carpal tunnel syndrome. *Eur Radiol* 2014; **24**: 434-440 [PMID: 24220753 DOI: 10.1007/s00330-013-3023-7]
- 48 **Lalitha P**, Reddy B. Synovial Sonoelastography: Utility in differentiating between inflammatory and infective synovitis- a comparative study with magnetic resonance imaging. *Eur Soc Radiol* 2011; C-0470
- 49 **Lalitha P**, Reddy MCh, Reddy KJ. Musculoskeletal applications of elastography: a pictorial essay of our initial experience. *Korean J Radiol* 2011; **12**: 365-375 [PMID: 21603296 DOI: 10.3348/kjr.2011.12.3.365]
- 50 **Magarelli N**, Carducci C, Bucalo C, Filograna L, Rapisarda S, De Waure C, Dell'Atti C, Maccauro G, Leone A, Bonomo L. Sonoelastography for qualitative and quantitative evaluation of superficial soft tissue lesions: a feasibility study. *Eur Radiol* 2014; **24**: 566-573 [PMID: 24272225 DOI: 10.1007/s00330-013-3069-6]
- 51 **Pass B**, Jafari M, Rowbotham E, Hensor EMA, Gupta H, Robinson P. Do quantitative and qualitative shear wave elastography have a role in evaluating musculoskeletal soft tissue masses? *Eur Radiol* 2016 Jun 8; Epub ahead of print [PMID: 27277260 DOI: 10.1007/s00330-016-4427-y]
- 52 **Mullen R**, Thompson JM, Moussa O, Vinnicombe S, Evans A. Shear-wave elastography contributes to accurate tumour size estimation when assessing small breast cancers. *Clin Radiol* 2014; **69**: 1259-1263 [PMID: 25239790 DOI: 10.1016/j.crad.2014.08.002]
- 53 **Madhok R**, Tapasvi C, Prasad U, Gupta AK, Aggarwal A. Acoustic radiation force impulse imaging of the liver: measurement of the normal mean values of the shearing wave velocity in a healthy liver. *J Clin Diagn Res* 2013; **7**: 39-42 [PMID: 23450092 DOI: 10.7860/JCDR/2012/5070.2665]
- 54 **Friedrich-Rust M**, Buggisch P, de Knecht RJ, Dries V, Shi Y, Matschenz K, Schneider MD, Herrmann E, Petersen J, Schulze F, Zeuzem S, Sarrazin C. Acoustic radiation force impulse imaging for non-invasive assessment of liver fibrosis in chronic hepatitis B. *J Viral Hepat* 2013; **20**: 240-247 [PMID: 23490368 DOI: 10.1111/j.1365-2893.2012.01646.x]
- 55 **Hanquinet S**, Courvoisier D, Kanavaki A, Dhouib A, Anooshiravani M. Acoustic radiation force impulse imaging-normal values of liver stiffness in healthy children. *Pediatr Radiol* 2013; **43**: 539-544 [PMID: 23247632 DOI: 10.1007/s00247-012-2553-5]
- 56 **D'Onofrio M**, Crosara S, De Robertis R, Canestrini S, Demozzi E, Gallotti A, Pozzi Mucelli R. Acoustic radiation force impulse of the liver. *World J Gastroenterol* 2013; **19**: 4841-4849 [PMID: 23946588 DOI: 10.3748/wjg.v19.i30.4841]
- 57 **Guzmán-Aroca F**, Frutos-Bernal MD, Bas A, Luján-Mompeán JA, Reus M, Berná-Serna Jde D, Parrilla P. Detection of non-alcoholic steatohepatitis in patients with morbid obesity before bariatric surgery: preliminary evaluation with acoustic radiation force impulse imaging. *Eur Radiol* 2012; **22**: 2525-2532 [PMID: 22648049 DOI: 10.1007/

- s00330-012-2505-3]
- 58 **Ying L**, Lin X, Xie ZL, Tang FY, Hu YP, Shi KQ. Clinical utility of acoustic radiation force impulse imaging for identification of malignant liver lesions: a meta-analysis. *Eur Radiol* 2012; **22**: 2798-2805 [PMID: 22772145 DOI: 10.1007/s00330-012-2540-0]
- 59 **Şirli R**, Sporea I, Bota S, Raţiu I. Liver elastography for the diagnosis of portal hypertension in patients with liver cirrhosis. *Med Ultrason* 2012; **14**: 225-230 [PMID: 22957328]
- 60 **Ginat DT**, Destounis SV, Barr RG, Castaneda B, Strang JG, Rubens DJ. US elastography of breast and prostate lesions. *Radiographics* 2009; **29**: 2007-2016 [PMID: 19926759 DOI: 10.1148/rg.297095058]
- 61 **Tozaki M**, Isobe S, Sakamoto M. Combination of elastography and tissue quantification using the acoustic radiation force impulse (ARFI) technology for differential diagnosis of breast masses. *Jpn J Radiol* 2012; **30**: 659-670 [PMID: 22836905 DOI: 10.1007/s11604-012-0106-3]
- 62 **Evans A**, Whelehan P, Thomson K, McLean D, Brauer K, Purdie C, Baker L, Jordan L, Rauchhaus P, Thompson A. Invasive breast cancer: relationship between shear-wave elastographic findings and histologic prognostic factors. *Radiology* 2012; **263**: 673-677 [PMID: 22523322 DOI: 10.1148/radiol.12111317]
- 63 **Correas JM**, Tissier AM, Khairoune A, Vassiliu V, Méjean A, Hélénon O, Memo R, Barr RG. Prostate cancer: diagnostic performance of real-time shear-wave elastography. *Radiology* 2015; **275**: 280-289 [PMID: 25599156 DOI: 10.1148/radiol.14140567]
- 64 **Bojunga J**, Dauth N, Berner C, Meyer G, Holzer K, Voelkl L, Herrmann E, Schroeter H, Zeuzem S, Friedrich-Rust M. Acoustic radiation force impulse imaging for differentiation of thyroid nodules. *PLoS One* 2012; **7**: e42735 [PMID: 22952609 DOI: 10.1371/journal.pone.0042735]

**P- Reviewer:** Razek AAKA, Schoenhagen P **S- Editor:** Ji FF  
**L- Editor:** A **E- Editor:** Lu YJ



## Mechanisms underlying $^{18}\text{F}$ -fluorodeoxyglucose accumulation in colorectal cancer

Kenji Kawada, Masayoshi Iwamoto, Yoshiharu Sakai

Kenji Kawada, Masayoshi Iwamoto, Yoshiharu Sakai, Department of Surgery, Graduate School of Medicine, Kyoto University, Kyoto 606-8507, Japan

**Author contributions:** Kawada K wrote the paper; Iwamoto M and Sakai Y contributed critical revision of the manuscript for important intellectual content.

**Conflict-of-interest statement:** The authors have no conflicts of interest to report.

**Open-Access:** This article is an open-access article which was selected by an in-house editor and fully peer-reviewed by external reviewers. It is distributed in accordance with the Creative Commons Attribution Non Commercial (CC BY-NC 4.0) license, which permits others to distribute, remix, adapt, build upon this work non-commercially, and license their derivative works on different terms, provided the original work is properly cited and the use is non-commercial. See: <http://creativecommons.org/licenses/by-nc/4.0/>

**Manuscript source:** Invited manuscript

**Correspondence to:** Kenji Kawada, MD, PhD, Department of Surgery, Graduate School of Medicine, Kyoto University, 54 Shogoin-Kawara-cho, Sakyo-ku, Kyoto 606-8507, Japan. [kkawada@kuhp.kyoto-u.ac.jp](mailto:kkawada@kuhp.kyoto-u.ac.jp)  
Telephone: +81-75-3667595  
Fax: +81-75-3667642

Received: June 1, 2016  
Peer-review started: June 9, 2016  
First decision: July 30, 2016  
Revised: August 24, 2016  
Accepted: September 13, 2016  
Article in press: September 15, 2016  
Published online: November 28, 2016

### Abstract

Positron emission tomography (PET) with  $^{18}\text{F}$ -fluorodeoxyglucose (FDG) is a diagnostic tool to evaluate metabolic activity by measuring accumulation of FDG, an

analogue of glucose, and has been widely used for detecting small tumors, monitoring treatment response and predicting patients' prognosis in a variety of cancers. However, the molecular mechanism of FDG accumulation into tumors remains to be investigated. It is well-known that most cancers are metabolically active with elevated glucose metabolism, a phenomenon known as the Warburg effect. The underlying mechanisms for elevated glucose metabolism in cancer tissues are complex. Recent reports have indicated the potential of FDG-PET/CT scans in predicting mutational status (*e.g.*, *KRAS* gene mutation) of colorectal cancer (CRC), which suggests that FDG-PET/CT scans may play a key role in determining therapeutic strategies by non-invasively predicting treatment response to anti-epidermal growth factor receptor (EGFR) therapy. In this review, we summarize the current findings investigating the molecular mechanism of  $^{18}\text{F}$ -FDG accumulation in CRC.

**Key words:**  $^{18}\text{F}$ -fluorodeoxyglucose-positron emission tomography; Colorectal cancer; Glucose metabolism; Mutational status; *KRAS*

© **The Author(s) 2016.** Published by Baishideng Publishing Group Inc. All rights reserved.

**Core tip:** Malignant cancers are preferential to metabolize glucose by glycolysis, even in the presence of oxygen, so-called Warburg effect. This elevated glucose metabolism is responsible for  $^{18}\text{F}$ -fluorodeoxyglucose (FDG) accumulation into cancer cells, which results in the positive signals in FDG-positron emission tomography scans. In spite of its clinical utility, the cellular and molecular mechanisms of  $^{18}\text{F}$ -FDG accumulation have not yet been elucidated. Here we review the current literature published with respect to the mechanisms of  $^{18}\text{F}$ -FDG accumulation into colorectal cancer tissues.

Kawada K, Iwamoto M, Sakai Y. Mechanisms underlying  $^{18}\text{F}$ -fluorodeoxyglucose accumulation in colorectal cancer. *World J Radiol* 2016; 8(11): 880-886 Available from: URL: <http://www.wjgnet.com>

## INTRODUCTION

Positron emission tomography (PET) with <sup>18</sup>F-fluorodeoxyglucose (FDG) is a imaging method used for detecting small tumors, monitoring treatment response and predicting patients' prognosis in a variety types of cancers<sup>[1,2]</sup>. This technique is based on evaluating tissue glucose metabolism by measuring accumulated FDG, a glucose analogue. FDG is incorporated into the cell through glucose transporters (GLUTs), and then phosphorylated by hexokinases (HXKs) to FDG-6-phosphate, which becomes stored within the cell. There is no standardized approach for quantitative measurement of <sup>18</sup>F-FDG accumulation yet, although the <sup>18</sup>F-FDG maximum standardized uptake value (SUV<sub>max</sub>) is commonly considered as a barometer of tumor viability. In addition to SUV<sub>max</sub>, there are some <sup>18</sup>F-FDG uptake-related quantitative parameters: SUV<sub>mean</sub> (average SUV within the tumor), SUV<sub>peak</sub> (peak SUV), metabolic tumor volume (MTV), total lesion glycolysis (TLG), *etc.*

Most cancer cells are preferential to metabolize glucose by glycolysis, even in the presence of oxygen, so-called "aerobic glycolysis (Warburg effect)"<sup>[3,4]</sup>. This increased glucose metabolism accounts for <sup>18</sup>F-FDG accumulation into cancer cells, which results in the positive signals in FDG-PET/CT scans. However, the mechanisms how <sup>18</sup>F-FDG is accumulated into cancer tissues are complex<sup>[5-7]</sup>. These factors are divided into tumor-related (*e.g.*, glucose metabolism, histological differentiation, vascular factor, tumor size and hypoxia) and non-tumor-related components (*e.g.*, high serum glucose level and local inflammation). <sup>18</sup>F-FDG is not specifically accumulated into cancer; it can also be accumulated into inflammatory sites as well. In spite of its clinical usefulness, the cellular and molecular mechanisms of <sup>18</sup>F-FDG accumulation have not yet been elucidated so far.

Colorectal cancer (CRC) is the third most common cancer and the fourth most common cause of cancer-related deaths in the world, with the majority attributable to distant metastases<sup>[8]</sup>. In spite of great advance in systemic treatment of metastatic CRC, the overall 5-year patient survival has remained lamentably low, below 10%. CRC is progressively promoted through multistep carcinogenesis of accumulated genetic changes in oncogenes and tumor suppressor genes. Most adenomas are initiated by inactivation of the *APC* gene, and then progress into adenocarcinomas through accumulation of additional alterations in the *KRAS*, *TP53* and *SMAD4* genes, *etc.*<sup>[9]</sup>.

In this context, this review summarizes the current literatures investigating the molecular mechanisms how <sup>18</sup>F-FDG is accumulated into CRC.

## GLUCOSE TRANSPORTERS AND HEXOKINASES

A line of literatures have demonstrated that <sup>18</sup>F-FDG accumulation in cancer cells depends largely on two classes of proteins: Glucose transporters (GLUT) and Hexokinases (HXKs)<sup>[10]</sup>. <sup>18</sup>F-FDG is incorporated into the cell via a family of 14 facilitative GLUTs, and then phosphorylated by HXKs to FDG-6-phosphate, which becomes stored within the cell, because of its negative charge. The up-regulation of GLUTs is commonly occurred in most cancers and is associated with poor prognosis of patients. Although different types of tumors have distinct expressions of different GLUTs, GLUT1 up-regulation is common in most cancers and is linked to tumor stage and prognosis<sup>[11,12]</sup>. In addition, increased levels of HXK (primarily, HXK2 of the 4 types) occur in many cancers<sup>[13,14]</sup>. HXK2 binds to the mitochondria membrane and efficiently phosphorylates FDG to FDG-6-phosphate. <sup>18</sup>F-FDG accumulation depends largely on GLUT1 and the rate-limiting glycolytic enzyme, HXK2, in most types of cancers, although other GLUT proteins (*e.g.*, GLUT3) and other enzymes downstream of HXK (*e.g.*, pyruvate dehydrogenase kinase 1) may be involved<sup>[10]</sup>. While the combined expression of GLUT1 and HXK2 likely plays some role in determining <sup>18</sup>F-FDG accumulation, the presence and strength of these associations seem to vary among tumor types, and conclusive evidence for one protein playing a dominant role is lacking. Although the molecular mechanisms of <sup>18</sup>F-FDG accumulation into CRC are not as well-analyzed as in breast and lung cancers, several studies indicate that, in CRC, an increase of GLUT1 expression is more essential for <sup>18</sup>F-FDG accumulation than HXK activity<sup>[10,15]</sup>.

### ***KRAS mutations in the KRAS gene in CRCs***

Oncogenic activation of *KRAS* affects several cellular functions that regulate morphology, proliferation, and motility. *KRAS* mutations occur in a variety of human malignancies, most frequently in pancreatic cancer, non-small cell lung cancer (NSCLC) and CRCs. In particular, *KRAS* mutations occur in approximately 40% of CRCs; mutations of codon 12 or 13 occur in more than 90% of the cases. The *RAS* gene family encodes membrane-bound guanosine triphosphate (GTP) proteins that interact with several metabolic pathways, such as mitogen-activated protein kinase (MAPK) and phosphoinositide 3-kinase (PI3K). Activating *RAS* mutations alter the activity of GTPase, inducing constitutive activation of *RAS* pathway. A number of clinical studies indicate that *KRAS* mutations can predict a lack of response to anti-epidermal growth factor receptor (EGFR) therapy<sup>[16,17]</sup>. The anti-EGFR antibodies (cetuximab and panitumumab) are now recommended only for CRCs with wild-type *KRAS*, although a wild-type *KRAS* gene does not guarantee a response. Therefore, mutational testing of the *KRAS* gene, using biopsied or resected tissues, is incorporated

into routine clinical practice. However, one limitation is the heterogeneity of *KRAS* mutational status, which can either be intratumoral heterogeneity within a primary CRC<sup>[18]</sup>, or discordant *KRAS* status between a primary CRC and its corresponding metastatic CRC<sup>[19,20]</sup>. Another limitation is failure to judge *KRAS* status due to poor quality of extracted DNA. In addition, it is not always easy to extract the samples from metastatic CRCs due to limited access and invasive procedures. Therefore, alternative non-invasive tool to predict the mutation profile, such as <sup>18</sup>F-FDG PET scans, could help overcome these limitations.

### Association between *KRAS* mutations and <sup>18</sup>F-FDG accumulation

There is recent preclinical evidence that *KRAS* mutations are associated with increased expression of GLUT1. Studies with isogenic CRC cell lines indicated a significant increase in glucose uptake caused by GLUT1 up-regulation, which is prominent in CRC cells with mutant *KRAS* alleles, providing them with a growth advantage in low glucose environment<sup>[21]</sup>. In a retrospective analysis ( $n = 51$ ), we previously found that SUVmax and tumor-to-liver ratio (TLR) were significantly higher in primary CRCs with mutated *KRAS* than in those with wild-type *KRAS*, and that SUVmax exhibited an odds ratio (OR) of 1.17 with an accuracy of 75% in predicting *KRAS* status when using a cutoff value of 13<sup>[22]</sup>. This was the first clinical report to show the causal relationship between *KRAS* mutations and <sup>18</sup>F-FDG accumulation in a variety of cancer.

Following this report, some other groups have also shown that <sup>18</sup>F-FDG accumulation can reflect *KRAS* mutational status in CRC and NSCLC (Table 1). Using a larger size of sample ( $n = 121$ ), Chen *et al.*<sup>[23]</sup> investigated the association between <sup>18</sup>F-FDG uptake-related parameters and *KRAS* mutational status, and found that SUVmax and TW40% (a 40% threshold level of SUVmax for tumor width (TW) were 2 predictors for *KRAS* mutations of CRC. Receiver operating characteristics analysis revealed that the accuracy of SUVmax was highest (70%) with a cutoff value of 11, and that the TW40% method could achieve higher accuracy (71.4%) when focusing on rectal cancer. Miles *et al.*<sup>[24]</sup> reported that multifunctional imaging with PET/CT and recursive decision-tree analysis to combine measurements of tumor <sup>18</sup>F-FDG uptake (SUVmax), CT texture (expressed as mean of positive pixels) and blood perfusion (measured by dynamic contrast-enhanced CT) enabled to identify CRCs with *KRAS* mutations showing hypoxic or proliferative phenotypes. This exploratory study with 33 CRC patients indicated that the true-positive rate, false-positive rate and accuracy of the decision tree were 82.4% (63.9%-93.9%), 0% (0%-10.4%) and 90.1% (79.2%-96.0%), respectively. The accuracy of SUVmax could be improved when combined with other imaging features: SUVmax, CT texture and perfusion. Lee *et al.*<sup>[25]</sup> investigated the relationship between <sup>18</sup>F-FDG uptake-related parameters (e.g., SUVmax, SUVpeak, MTV and TLG), *KRAS* mutations and C-reactive protein (CRP) with 179 CRC cases. Multivariate analysis demonstrated that

SUVmax and SUVpeak are significantly associated with *KRAS* mutational status (OR, 3.3,  $P = 0.005$  and OR, 3.9,  $P = 0.004$ , respectively) together with histological findings and lymph node metastasis. <sup>18</sup>F-FDG accumulation was significantly higher in CRCs with mutated *KRAS* and normal CRP levels. CRCs with high CRP levels ( $> 6.0$  mg/L;  $n = 47$ ) was correlated to larger tumor size, higher SUVmax, higher SUVpeak, higher MTV and higher TLG, compared to those with low CRP levels ( $< 6.0$  mg/L;  $n = 132$ ), which indicates that local inflammation with high CRP levels could affect <sup>18</sup>F-FDG quantification in CRC tumors.

However, the clinical benefit of above findings was limited, because endoscopic biopsy for *KRAS* mutational testing is easy in primary CRC. Importantly, we have recently examined whether a similar relationship can exist in metastatic CRC<sup>[26]</sup>. In a retrospective analysis with 55 metastatic CRC tumors, we found that SUVmax was not associated with *KRAS* mutational status. However, when focusing on tumors larger than 10 mm in order to remove the partial volume effect, SUVmax was significantly higher in CRCs with mutated *KRAS* than in those with wild-type *KRAS* ( $8.3 \pm 4.1$  and  $5.7 \pm 2.4$ , respectively;  $P = 0.03$ ). *KRAS* status of metastatic CRC was predicted with an accuracy of 71.4% when using a SUVmax cutoff value of 6.0. This is the first clinical study showing a causal relationship between <sup>18</sup>F-FDG accumulation and *KRAS* mutations in metastatic CRC, which indicates that FDG-PET/CT scans might determine therapeutic strategies by predicting treatment response to anti-EGFR therapy. Meanwhile, Krikelis *et al.*<sup>[27]</sup> reported a lack of association between <sup>18</sup>F-FDG accumulation and *KRAS* mutational status of metastatic CRC. Although sample size and ethnic differences might be sources of the bias, we suppose that the lack of association may be due to improper patient selection. In other clinical studies, patients with high serum glucose levels, small-sized tumors or high CRP levels were excluded, because these variables interfere with <sup>18</sup>F-FDG accumulation.

In genetically engineered mouse models (GEMM)-derived orthotopic transplant models of CRC, subcutaneous tumors from *KRAS*-mutant *APC*<sup>-/-</sup> *TP53*<sup>-/-</sup> CRC cells produced a significantly higher <sup>18</sup>F-FDG PET signal compared to *KRAS*-wild-type *APC*<sup>-/-</sup> *TP53*<sup>-/-</sup> CRC cells<sup>[28]</sup>. Oncogenic *KRAS* promotes an increase in cellular glucose uptake and lactate production *in vitro* and *in vivo*.

Regarding NSCLC ( $n = 102$ ), Caicedo *et al.*<sup>[29]</sup> found that NSCLC tumors harboring *KRAS* mutations exhibited significantly higher <sup>18</sup>F-FDG accumulation than those with wild-type *KRAS*, although no associations between different EGFR mutation types and <sup>18</sup>F-FDG uptake were found. The sensitivity and specificity of *KRAS* mutational status were 78.6% and 62.2%, respectively, with a diagnostic accuracy of 66.7%. A multivariate model with stage, gender, age and SUVmean could predict *KRAS* mutational status in stage III or IV. A recent study using GEMM of lung cancer reported that mice harboring lung tumors with *KRAS* and *LKB1* or *TP53* mutations showed

**Table 1** Clinical reports investigating the relationship between <sup>18</sup>F-fluorodeoxyglucose accumulation and *KRAS* mutations

Ref.	Cancer type	Sample size	Parameters related to <i>KRAS</i> mutations	Sensitivity (%)	Specificity (%)	Accuracy (%)
Kawada <i>et al.</i> <sup>[22]</sup>	CRC	51	SUVmax	74.0	75.0	75.0
			TLR	70.0	71.0	71.0
Chen <i>et al.</i> <sup>[23]</sup>	CRC	121	SUVmax	52.4	71.7	70.0
	CRC	121	TW40%	53.2	67.6	62.0
	RC	49	TW40%	80.0	79.1	71.4
Miles <i>et al.</i> <sup>[24]</sup>	CRC	33	Decision tree with SUVmax, MPP and BF	82.4	100.0	90.1
Lee <i>et al.</i> <sup>[25]</sup>	CRC	132		SUVmax	60.0	50.3
			SUVpeak	73.3	60.5	67.8
Caicedo <i>et al.</i> <sup>[29]</sup>	NSCLC	102	SUVmean	78.6	62.2	66.7
Kawada <i>et al.</i> <sup>[26]</sup>	mCRC	42	SUVmax	68.0	74.0	71.4

SUV: Standardized uptake value; TLR: Tumor-to-liver SUV ratio; TW40%: A 40% threshold level of SUVmax for tumor width; MPP: Mean of positive pixels; BF: Blood flow; CRC: Colorectal cancer; RC: Rectal cancer; NSCLC: Non-small-cell lung cancer; mCRC: Metastatic CRC.

significantly higher <sup>18</sup>F-FDG accumulation than those with only *KRAS* mutations<sup>[30]</sup>. Taken together, FDG-PET/CT scans could predict *KRAS* mutational status in a variety of human *KRAS*-related cancers (CRC, NSCLC, pancreatic cancer, *etc.*).

## HYPOXIA

The relationship between glucose metabolism and tumor growth can be explained by adaptation to hypoxia through up-regulation of GLUTs as well as the translocation and increased enzymatic activity of HXK<sup>[31]</sup>. Hypoxia-inducible factor-1 $\alpha$  (HIF-1 $\alpha$ ) mediates cellular response to hypoxia, such as glucose metabolism and angiogenesis. Under hypoxic conditions, HIF-1 $\alpha$  accelerates glycolysis by up-regulation of inducing glucose transporters and some enzymes<sup>[32]</sup>. Some researchers have reported that there is a synergistic interaction between hypoxia, mutated *KRAS* and GLUT1 expression<sup>[33-36]</sup>. When CRC cells were cultured *in vitro* under hypoxia, mutated *KRAS* increased the translation of HIF-1 $\alpha$  by the PI3K pathway<sup>[33]</sup>. In addition, hypoxia or HIF-1 $\alpha$  could also increase mutated *KRAS* activity, which indicate that there is a positive feedback between *KRAS* pathway and hypoxia<sup>[36]</sup>. Hypoxia can boost expression levels of GLUT1 through HIF-1 $\alpha$ <sup>[35]</sup>. We have recently reported that mutated *KRAS* causes higher <sup>18</sup>F-FDG accumulation by up-regulation of GLUT1 and at least partially by induction of HIF-1 $\alpha$  under hypoxia<sup>[37]</sup>. We also examined 51 clinical CRC samples, and found that *KRAS* mutational status was significantly associated with SUVmax and with GLUT1 expression, but not with HXK2 expression<sup>[21,35]</sup>. These data suggest that <sup>18</sup>F-FDG accumulation observed in FDG-PET scans could reflect elevated glucose metabolism by mutated *KRAS* and hypoxia.

Goh *et al.*<sup>[38]</sup> investigated the *in vivo* flow-metabolic phenotype by integrated <sup>18</sup>F-FDG PET/perfusion CT and its relationship to histopathological findings with 45 primary CRCs. The flow-metabolic ratio was significantly lower for CRCs with high expressions of VEGF or HIF-1 $\alpha$  compared to CRCs with lower expression, which indicated that CRCs with a low-flow-high-metabolism phenotype reflected a more angiogenic phenotype. With breast

cancer cell lines, Smith *et al.*<sup>[39]</sup> reported that hypoxia up-regulated GLUT1 and 6-phosphofructo-2-kinase (PFK) involved in glucose transport and glycolysis, and that these changes were induced by HIF-1 $\alpha$  up-regulation and AMP-activated protein kinase (AMPK) activation. Preclinical studies have reported a correlation between <sup>18</sup>F-FDG accumulation and tumor hypoxia detected by pimonidazole<sup>[40]</sup> or <sup>18</sup>F-fluoromisonidazole (FMISO)<sup>[41]</sup>, a PET tracer designed to identify hypoxic cells. Similarly, some studies noted a correlation between <sup>18</sup>F-FDG and <sup>18</sup>F-FMISO retention in a clinical setting<sup>[42,43]</sup>.

## ONCOGENE PATHWAY ACTIVATION

Using GEMM, Alvarez *et al.*<sup>[44]</sup> investigated <sup>18</sup>F-FDG accumulation in tumors driven by c-Myc, HER2/neu, Akt1, Wnt1 or H-RAS oncogenes, and found that <sup>18</sup>F-FDG accumulation was correlated positively with HXK2 and HIF-1 $\alpha$ , and negatively with PFK2b and p-AMPK. The correlation between HXK2 and <sup>18</sup>F-FDG accumulation was not dependent on all variables tested, indicating that HXK2 could independently predict <sup>18</sup>F-FDG accumulation in this model. In contrast, GLUT1 expression was associated with <sup>18</sup>F-FDG accumulation only in tumors driven by Akt1 or HER2/neu. These above results demonstrated that the oncogenic pathway was a determinant of <sup>18</sup>F-FDG accumulation mediated by glycolytic enzymes. Moreover, certain oncogenes such as Src and c-Myc, as well as elements of the PI3K/Akt pathway, can be associated with activated glycolysis<sup>[45-47]</sup>.

Tian *et al.*<sup>[48]</sup> investigated the correlations between SUVmax and expressions of GLUT1, hepatocyte growth factor (HGF) and vascular endothelial growth factor-C (VEGF-C) in 33 CRC patients, and found that there was a significant differences in SUVmax among CRCs expressing GLUT1, HGF, c-Met and VEGF-1. Choi *et al.*<sup>[49]</sup> investigated the correlations between SUVmax and EGFR expression with 132 CRC patients, and found that SUVmax was significantly lower in EGFR-non-expressing tumors than in EGFR-expressing tumors (10.0  $\pm$  4.2 vs 12.1  $\pm$  2.1; *P* = 0.012). At the SUVmax threshold of 7.5, the sensitivity and specificity for predicting EGFR expression were 84.9% and 40.4%, which indicated SUVmax had a limited role in

predicting EGFR expression. In preclinical murine models with tumor xenografts, Ma *et al.*<sup>[50]</sup> reported that <sup>18</sup>F-FDG PET accumulation was correlated with activated Akt and cellular membrane-bound GLUT1, and that the FDG-PET response did not correlate with the tumor growth response during mammalian target of rapamycin (mTOR) inhibitor therapy.

## HUMAN CYTOMEGALOVIRUS AND EPSTEIN-BARR VIRUS

It has been debated whether human cytomegalovirus (HCMV) and Epstein-Barr virus (EBV) are involved in rectal cancer. Sole *et al.*<sup>[51]</sup> reported that patients with HCMV/EBV co-infection had a significantly higher SUVmax than patients without viral co-infection, when analyzing 37 rectal cancer patients ( $P = 0.02$ ). *KRAS* wild-type status was significantly more frequently observed in patients with EBV and HCMV/EBV co-infection.

## F-BOX AND WD REPEAT DOMAIN-CONTAINING 7

F-box and WD repeat domain-containing 7 (FBW7) is a E3 ubiquitin ligase and a tumor suppressor frequently mutated in CRC. In CRC, it was recently reported that FBW7 targets CDX2 (caudal-related homeobox transcription factor 2) for degradation *via* two cdc42-phosphoclegron motifs in a GSK3beta-dependent manner<sup>[52]</sup>. Ji *et al.*<sup>[53]</sup> have recently reported that *KRAS* mutations inhibit the tumor suppressor FBW7, which negatively regulates glucose metabolism by targeting the c-Myc/TXNIP (thioredoxin binding protein) axis in pancreatic cancer. The expression level of FBW7 was negatively associated with PET/CT SUVmax in 60 pancreatic cancer patients, indicating that FBW7 is an important *KRAS* downstream effector and might reverse *KRAS*-driven metabolic change.

## LACTATE DEHYDROGENASE A

Lactate dehydrogenase A (LDHA) converts pyruvate to lactate and is overexpressed in many cancers<sup>[54]</sup>. Up-regulation of LDHA ensures efficient glycolytic metabolism for tumor cells and reduces oxygen dependency<sup>[55]</sup>. In a retrospective analysis of 51 lung adenocarcinomas, Zhou *et al.*<sup>[56]</sup> reported that SUVmax was significantly higher in the LDHA high-expression group than the LDHA low-expression group ( $P = 0.018$ ). GLUT1 expression in lung adenocarcinomas was significantly associated with <sup>18</sup>F-FDG accumulation and LDHA expression, whereas HXK2 expression was not. In CRC, it was recently reported that LDHA negatively regulated by miRNAs promotes aerobic glycolysis<sup>[57]</sup>.

## PROLIFERATION-ASSOCIATED ANTIGEN KI-67

According to a meta-analysis (81 studies, 3242 patients),

Deng *et al.*<sup>[58]</sup> reported that the relationship between <sup>18</sup>F-FDG accumulation and Ki-67 expression was significant in thymic epithelial tumors, gastrointestinal stromal tumors (GISTs), moderate in breast, lung and pancreatic cancers, and average in CRCs, and poor in thyroid and gastric cancers.

## CONCLUSION

For prediction of *KRAS* mutations in CRC, the overall accuracy of SUVmax alone has only been found to be modest, ranging from 60% to 75%, although the accuracy could be improved when combined with other clinicopathologic or imaging parameters. New targeted therapies are being developed for tumors that selectively express *KRAS* mutations<sup>[59]</sup>. Hence, the availability of non-invasive methods, such as molecular imaging, for predicting *KRAS* mutational status could have considerable clinical relevance, because of their potential to improve the assessment of other molecular alterations in the future. Future advances in PET radiotracers may increase the sensitivity and specificity of this technique to provide full molecular assessment of CRC.

## REFERENCES

- 1 de Geus-Oei LF, Vriens D, van Laarhoven HW, van der Graaf WT, Oyen WJ. Monitoring and predicting response to therapy with <sup>18</sup>F-FDG PET in colorectal cancer: a systematic review. *J Nucl Med* 2009; **50** Suppl 1: 43S-54S [PMID: 19403879 DOI: 10.2967/jnumed.108.057224]
- 2 Moulton CA, Gu CS, Law CH, Tandan VR, Hart R, Quan D, Fairfull Smith RJ, Jalink DW, Husien M, Serrano PE, Hendler AL, Haider MA, Ruo L, Gulenchyn KY, Finch T, Julian JA, Levine MN, Gallinger S. Effect of PET before liver resection on surgical management for colorectal adenocarcinoma metastases: a randomized clinical trial. *JAMA* 2014; **311**: 1863-1869 [PMID: 24825641 DOI: 10.1001/jama.2014.3740]
- 3 Warburg O. On the origin of cancer cells. *Science* 1956; **123**: 309-314 [PMID: 13298683 DOI: 10.1126/science.123.3191.309]
- 4 Koppenol WH, Bounds PL, Dang CV. Otto Warburg's contributions to current concepts of cancer metabolism. *Nat Rev Cancer* 2011; **11**: 325-337 [PMID: 21508971 DOI: 10.1038/nrc3038]
- 5 Pauwels EK, Ribeiro MJ, Stoot JH, McCready VR, Bourguignon M, Mazzière B. FDG accumulation and tumor biology. *Nucl Med Biol* 1998; **25**: 317-322 [PMID: 9639291 DOI: 10.1016/S0969-8051(97)00226-6]
- 6 Gillies RJ, Robey I, Gatenby RA. Causes and consequences of increased glucose metabolism of cancers. *J Nucl Med* 2008; **49** Suppl 2: 24S-42S [PMID: 18523064 DOI: 10.2967/jnumed.107.047258]
- 7 Plathow C, Weber WA. Tumor cell metabolism imaging. *J Nucl Med* 2008; **49** Suppl 2: 43S-63S [PMID: 18523065 DOI: 10.2967/jnumed.107.045930]
- 8 Weitz J, Koch M, Debus J, Höhler T, Galle PR, Büchler MW. Colorectal cancer. *Lancet* 2005; **365**: 153-165 [PMID: 15639298 DOI: 10.1016/S0140-6736(05)17706-X]
- 9 Weinberg RA. Multi-step tumorigenesis. In: The biology of cancer. Chapter 11. New York, NY: Garland Science Taylor & Francis Group, LLC, 2007; **11**: 399-462
- 10 Jadvar H, Alavi A, Gambhir SS. <sup>18</sup>F-FDG uptake in lung, breast, and colon cancers: molecular biology correlates and disease characterization. *J Nucl Med* 2009; **50**: 1820-1827 [PMID: 19837767 DOI: 10.2967/jnumed.108.054098]
- 11 Medina RA, Owen GI. Glucose transporters: expression, regulation and cancer. *Biol Res* 2002; **35**: 9-26 [PMID: 12125211 DOI: 10.4067/S0716-97602002000100004]

- 12 **Smith TA.** Facilitative glucose transporter expression in human cancer tissue. *Br J Biomed Sci* 1999; **56**: 285-292 [PMID: 10795374]
- 13 **Mathupala SP,** Ko YH, Pedersen PL. Hexokinase II: cancer's double-edged sword acting as both facilitator and gatekeeper of malignancy when bound to mitochondria. *Oncogene* 2006; **25**: 4777-4786 [PMID: 16892090 DOI: 10.1038/sj.onc.1209603]
- 14 **Smith TA.** Mammalian hexokinases and their abnormal expression in cancer. *Br J Biomed Sci* 2000; **57**: 170-178 [PMID: 10912295]
- 15 **Maddalena F,** Lettini G, Gallicchio R, Sisinni L, Simeon V, Nardelli A, Venetucci AA, Storto G, Landriscina M. Evaluation of Glucose Uptake in Normal and Cancer Cell Lines by Positron Emission Tomography. *Mol Imaging* 2015; **14**: 490-498 [PMID: 26461458]
- 16 **Jonker DJ,** O'Callaghan CJ, Karapetis CS, Zalberg JR, Tu D, Au HJ, Berry SR, Krahn M, Price T, Simes RJ, Tebbutt NC, van Hazel G, Wierzbicki R, Langer C, Moore MJ. Cetuximab for the treatment of colorectal cancer. *N Engl J Med* 2007; **357**: 2040-2048 [PMID: 18003960 DOI: 10.1056/NEJMoa071834]
- 17 **Karapetis CS,** Khambata-Ford S, Jonker DJ, O'Callaghan CJ, Tu D, Tebbutt NC, Simes RJ, Chalchal H, Shapiro JD, Robitaille S, Price TJ, Shepherd L, Au HJ, Langer C, Moore MJ, Zalberg JR. K-ras mutations and benefit from cetuximab in advanced colorectal cancer. *N Engl J Med* 2008; **359**: 1757-1765 [PMID: 18946061 DOI: 10.1056/NEJMoa0804385]
- 18 **Baldus SE,** Schaefer KL, Engers R, Hartleb D, Stoecklein NH, Gabbert HE. Prevalence and heterogeneity of KRAS, BRAF, and PIK3CA mutations in primary colorectal adenocarcinomas and their corresponding metastases. *Clin Cancer Res* 2010; **16**: 790-799 [PMID: 20103678 DOI: 10.1158/1078-0432.CCR-09-2446]
- 19 **Albanese I,** Scibetta AG, Migliavacca M, Russo A, Bazan V, Tomasino RM, Colomba P, Tagliavia M, La Farina M. Heterogeneity within and between primary colorectal carcinomas and matched metastases as revealed by analysis of Ki-ras and p53 mutations. *Biochem Biophys Res Commun* 2004; **325**: 784-791 [PMID: 15541358 DOI: 10.1016/j.bbrc.2004.10.111]
- 20 **Molinari F,** Martin V, Saletti P, De Dosso S, Spitale A, Camponovo A, Bordoni A, Crippa S, Mazzucchelli L, Frattini M. Differing deregulation of EGFR and downstream proteins in primary colorectal cancer and related metastatic sites may be clinically relevant. *Br J Cancer* 2009; **100**: 1087-1094 [PMID: 19293803 DOI: 10.1038/sj.bjc.6604848]
- 21 **Yun J,** Rago C, Cheong I, Pagliarini R, Angenendt P, Rajagopalan H, Schmidt K, Willson JK, Markowitz S, Zhou S, Diaz LA, Velculescu VE, Lengauer C, Kinzler KW, Vogelstein B, Papadopoulos N. Glucose deprivation contributes to the development of KRAS pathway mutations in tumor cells. *Science* 2009; **325**: 1555-1559 [PMID: 19661383 DOI: 10.1126/science.1174229]
- 22 **Kawada K,** Nakamoto Y, Kawada M, Hida K, Matsumoto T, Murakami T, Hasegawa S, Togashi K, Sakai Y. Relationship between 18F-fluorodeoxyglucose accumulation and KRAS/BRAF mutations in colorectal cancer. *Clin Cancer Res* 2012; **18**: 1696-1703 [PMID: 22282467 DOI: 10.1158/1078-0432.CCR-11-1909]
- 23 **Chen SW,** Chiang HC, Chen WT, Hsieh TC, Yen KY, Chiang SF, Kao CH. Correlation between PET/CT parameters and KRAS expression in colorectal cancer. *Clin Nucl Med* 2014; **39**: 685-689 [PMID: 24978328 DOI: 10.1097/RLU.0000000000000481]
- 24 **Miles KA,** Ganeshan B, Rodriguez-Justo M, Goh VJ, Ziauddin Z, Engledow A, Meagher M, Endozo R, Taylor SA, Halligan S, Ell PJ, Groves AM. Multifunctional imaging signature for V-KI-RAS2 Kirsten rat sarcoma viral oncogene homolog (KRAS) mutations in colorectal cancer. *J Nucl Med* 2014; **55**: 386-391 [PMID: 24516257 DOI: 10.2967/jnumed.113.120485]
- 25 **Lee JH,** Kang J, Baik SH, Lee KY, Lim BJ, Jeon TJ, Ryu YH, Sohn SK. Relationship Between 18F-Fluorodeoxyglucose Uptake and V-Ki-Ras2 Kirsten Rat Sarcoma Viral Oncogene Homolog Mutation in Colorectal Cancer Patients: Variability Depending on C-Reactive Protein Level. *Medicine* (Baltimore) 2016; **95**: e2236 [PMID: 26735530 DOI: 10.1097/MD.0000000000002236]
- 26 **Kawada K,** Toda K, Nakamoto Y, Iwamoto M, Hatano E, Chen F, Hasegawa S, Togashi K, Date H, Uemoto S, Sakai Y. Relationship Between 18F-FDG PET/CT Scans and KRAS Mutations in Metastatic Colorectal Cancer. *J Nucl Med* 2015; **56**: 1322-1327 [PMID: 26135109 DOI: 10.2967/jnumed.115.160614]
- 27 **Krikelis D,** Skoura E, Kotoula V, Rondogianni P, Pianou N, Samartzis A, Xanthakis I, Fountzilias G, Datsis IE. Lack of association between KRAS mutations and 18F-FDG PET/CT in Caucasian metastatic colorectal cancer patients. *Anticancer Res* 2014; **34**: 2571-2579 [PMID: 24778079]
- 28 **Martin ES,** Belmont PJ, Sinnamon MJ, Richard LG, Yuan J, Coffee EM, Roper J, Lee L, Heidari P, Lunt SY, Goel G, Ji X, Xie Z, Xie T, Lamb J, Weinrich SL, VanArsdale T, Bronson RT, Xavier RJ, Vander Heiden MG, Kan JL, Mahmood U, Hung KE. Development of a colon cancer GEMM-derived orthotopic transplant model for drug discovery and validation. *Clin Cancer Res* 2013; **19**: 2929-2940 [PMID: 23403635 DOI: 10.1158/1078-0432.CCR-12-2307]
- 29 **Caicedo C,** Garcia-Velloso MJ, Lozano MD, Labiano T, Vigil Diaz C, Lopez-Picazo JM, Gurrpide A, Zulueta JJ, Richter Echevarria JA, Perez Gracia JL. Role of [<sup>18</sup>F]FDG PET in prediction of KRAS and EGFR mutation status in patients with advanced non-small-cell lung cancer. *Eur J Nucl Med Mol Imaging* 2014; **41**: 2058-2065 [PMID: 24990403 DOI: 10.1007/s00259-014-2833-4]
- 30 **Chen Z,** Cheng K, Walton Z, Wang Y, Ebi H, Shimamura T, Liu Y, Tupper T, Ouyang J, Li J, Gao P, Woo MS, Xu C, Yanagita M, Altabef A, Wang S, Lee C, Nakada Y, Peña CG, Sun Y, Franchetti Y, Yao C, Saur A, Cameron MD, Nishino M, Hayes DN, Wilkerson MD, Roberts PJ, Lee CB, Bardeesy N, Butaney M, Chirieac LR, Costa DB, Jackman D, Sharpless NE, Castrillon DH, Demetri GD, Jänne PA, Pandolfi PP, Cantley LC, Kung AL, Engelman JA, Wong KK. A murine lung cancer co-clinical trial identifies genetic modifiers of therapeutic response. *Nature* 2012; **483**: 613-617 [PMID: 22425996 DOI: 10.1038/nature10937]
- 31 **Macheda ML,** Rogers S, Best JD. Molecular and cellular regulation of glucose transporter (GLUT) proteins in cancer. *J Cell Physiol* 2005; **202**: 654-662 [PMID: 15389572 DOI: 10.1002/jcp.20166]
- 32 **Semenza GL.** HIF-1 mediates metabolic responses to intratumoral hypoxia and oncogenic mutations. *J Clin Invest* 2013; **123**: 3664-3671 [PMID: 23999440 DOI: 10.1172/JCI67230]
- 33 **Kikuchi H,** Pino MS, Zeng M, Shirasawa S, Chung DC. Oncogenic KRAS and BRAF differentially regulate hypoxia-inducible factor-1 $\alpha$  and -2 $\alpha$  in colon cancer. *Cancer Res* 2009; **69**: 8499-8506 [PMID: 19843849 DOI: 10.1158/0008-5472.CAN-09-2213]
- 34 **Zeng M,** Kikuchi H, Pino MS, Chung DC. Hypoxia activates the K-ras proto-oncogene to stimulate angiogenesis and inhibit apoptosis in colon cancer cells. *PLoS One* 2010; **5**: e10966 [PMID: 20532039 DOI: 10.1371/journal.pone.0010966]
- 35 **Lee-Kong SA,** Ruby JA, Chessin DB, Pucciarelli S, Shia J, Riedel ER, Nitti D, Guillem JG. Hypoxia-related proteins in patients with rectal cancer undergoing neoadjuvant combined modality therapy. *Dis Colon Rectum* 2012; **55**: 990-995 [PMID: 22874607 DOI: 10.1097/DCR.0b013e31825bd80c]
- 36 **Wang Y,** Lei F, Rong W, Zeng Q, Sun W. Positive feedback between oncogenic KRAS and HIF-1 $\alpha$  confers drug resistance in colorectal cancer. *Onco Targets Ther* 2015; **8**: 1229-1237 [PMID: 26060408 DOI: 10.2147/OTT.S80017]
- 37 **Iwamoto M,** Kawada K, Nakamoto Y, Itatani Y, Inamoto S, Toda K, Kimura H, Sasazuki T, Shirasawa S, Okuyama H, Inoue M, Hasegawa S, Togashi K, Sakai Y. Regulation of 18F-FDG accumulation in colorectal cancer cells with mutated KRAS. *J Nucl Med* 2014; **55**: 2038-2044 [PMID: 25453050 DOI: 10.2967/jnumed.114.142927]
- 38 **Goh V,** Engledow A, Rodriguez-Justo M, Shastry M, Peck J, Blackman G, Endozo R, Taylor S, Halligan S, Ell P, Groves AM. The flow-metabolic phenotype of primary colorectal cancer: assessment by integrated 18F-FDG PET/perfusion CT with histopathologic correlation. *J Nucl Med* 2012; **53**: 687-692 [PMID: 22454485 DOI: 10.2967/jnumed.111.098525]
- 39 **Smith TA,** Zanda M, Fleming IN. Hypoxia stimulates 18F-fluorodeoxyglucose uptake in breast cancer cells via hypoxia inducible factor-1 and AMP-activated protein kinase. *Nucl Med Biol* 2013; **40**: 858-864 [PMID: 23786679 DOI: 10.1016/j.nuclmedbio.2013.05.006]
- 40 **Dearling JL,** Flynn AA, Sutcliffe-Goulden J, Petrie IA, Boden

- R, Green AJ, Boxer GM, Begent RH, Pedley RB. Analysis of the regional uptake of radiolabeled deoxyglucose analogs in human tumor xenografts. *J Nucl Med* 2004; **45**: 101-107 [PMID: 14734681]
- 41 **Wyss MT**, Honer M, Schubiger PA, Ametamey SM. NanoPET imaging of [(18)F]fluoromisonidazole uptake in experimental mouse tumours. *Eur J Nucl Med Mol Imaging* 2006; **33**: 311-318 [PMID: 16258762 DOI: 10.1007/s00259-005-1951-4]
- 42 **Rajendran JG**, Mankoff DA, O'Sullivan F, Peterson LM, Schwartz DL, Conrad EU, Spence AM, Muzi M, Farwell DG, Krohn KA. Hypoxia and glucose metabolism in malignant tumors: evaluation by [18F]fluoromisonidazole and [18F]fluorodeoxyglucose positron emission tomography imaging. *Clin Cancer Res* 2004; **10**: 2245-2252 [PMID: 15073099 DOI: 10.1158/1078-0432.CCR-0688-3]
- 43 **Zimny M**, Gagel B, DiMartino E, Hamacher K, Coenen HH, Westhofen M, Eble M, Buell U, Reinartz P. FDG--a marker of tumour hypoxia? A comparison with [18F]fluoromisonidazole and pO<sub>2</sub>-polarography in metastatic head and neck cancer. *Eur J Nucl Med Mol Imaging* 2006; **33**: 1426-1431 [PMID: 16841141 DOI: 10.1007/s00259-006-0175-6]
- 44 **Alvarez JV**, Belka GK, Pan TC, Chen CC, Blankemeyer E, Alavi A, Karp JS, Chodosh LA. Oncogene pathway activation in mammary tumors dictates FDG-PET uptake. *Cancer Res* 2014; **74**: 7583-7598 [PMID: 25239452 DOI: 10.1158/0008-5472.CAN-14-1235]
- 45 **Flier JS**, Mueckler MM, Usher P, Lodish HF. Elevated levels of glucose transport and transporter messenger RNA are induced by ras or src oncogenes. *Science* 1987; **235**: 1492-1495 [PMID: 3103217 DOI: 10.1126/science.3103217]
- 46 **Osthus RC**, Shim H, Kim S, Li Q, Reddy R, Mukherjee M, Xu Y, Wonsley D, Lee LA, Dang CV. Deregulation of glucose transporter 1 and glycolytic gene expression by c-Myc. *J Biol Chem* 2000; **275**: 21797-21800 [PMID: 10823814 DOI: 10.1074/jbc.C000023200]
- 47 **Wieman HL**, Wofford JA, Rathmell JC. Cytokine stimulation promotes glucose uptake via phosphatidylinositol-3 kinase/Akt regulation of Glut1 activity and trafficking. *Mol Biol Cell* 2007; **18**: 1437-1446 [PMID: 17301289 DOI: 10.1091/mbc.E06-07-0593]
- 48 **Tian M**, Yu L, Zhang Y, Gao X. Correlations between SUVmax and expression of GLUT1 and growth factors inducing lymphangiogenesis. *Acad Radiol* 2012; **19**: 420-426 [PMID: 22444673 DOI: 10.1016/j.acra.2011.12.006]
- 49 **Choi YJ**, Kim MJ, Lee BH, Kwon MJ, Hwang HS. Relationship between Preoperative <sup>18</sup>F-Fluorodeoxyglucose Uptake and Epidermal Growth Factor Receptor Status in Primary Colorectal Cancer. *Yonsei Med J* 2016; **57**: 232-237 [PMID: 26632406 DOI: 10.3349/ymj.2016.57.1.232]
- 50 **Ma WW**, Jacene H, Song D, Vilardell F, Messersmith WA, Laheru D, Wahl R, Endres C, Jimeno A, Pomper MG, Hidalgo M. [18F]fluorodeoxyglucose positron emission tomography correlates with Akt pathway activity but is not predictive of clinical outcome during mTOR inhibitor therapy. *J Clin Oncol* 2009; **27**: 2697-2704 [PMID: 19380450 DOI: 10.1200/JCO.2008.18.8383]
- 51 **Sole CV**, Calvo FA, Ferrer C, Alvarez E, Carreras JL, Ochoa E. Human cytomegalovirus and Epstein-Barr virus infection impact on (18)F-FDG PET/CT SUVmax, CT volumetric and KRAS-based parameters of patients with locally advanced rectal cancer treated with neoadjuvant therapy. *Eur J Nucl Med Mol Imaging* 2015; **42**: 186-196 [PMID: 25269837 DOI: 10.1007/s00259-014-2910-8]
- 52 **Kumar Y**, Shukla N, Thacker G, Kapoor I, Lochab S, Bhatt ML, Chattopadhyay N, Sanyal S, Trivedi AK. Ubiquitin Ligase, Fbw7, Targets CDX2 for Degradation via Two Phosphodegron Motifs in a GSK3β-Dependent Manner. *Mol Cancer Res* 2016; **14**: 1097-1109 [PMID: 27470268 DOI: 10.1158/1541-7786.MCR-16-0138]
- 53 **Ji S**, Qin Y, Liang C, Huang R, Shi S, Liu J, Jin K, Liang D, Xu W, Zhang B, Liu L, Liu C, Xu J, Ni Q, Chiao PJ, Li M, Yu X. FBW7 (F-box and WD Repeat Domain-Containing 7) Negatively Regulates Glucose Metabolism by Targeting the c-Myc/TXNIP (Thioredoxin-Binding Protein) Axis in Pancreatic Cancer. *Clin Cancer Res* 2016; **22**: 3950-3960 [PMID: 26983463 DOI: 10.1158/1078-0432.CCR-15-2380]
- 54 **Miao P**, Sheng S, Sun X, Liu J, Huang G. Lactate dehydrogenase A in cancer: a promising target for diagnosis and therapy. *IUBMB Life* 2013; **65**: 904-910 [PMID: 24265197 DOI: 10.1002/iub.1216]
- 55 **Fantin VR**, St-Pierre J, Leder P. Attenuation of LDH-A expression uncovers a link between glycolysis, mitochondrial physiology, and tumor maintenance. *Cancer Cell* 2006; **9**: 425-434 [PMID: 16766262 DOI: 10.1016/j.ccr.2006.04.023]
- 56 **Zhou X**, Chen R, Xie W, Ni Y, Liu J, Huang G. Relationship between 18F-FDG accumulation and lactate dehydrogenase A expression in lung adenocarcinomas. *J Nucl Med* 2014; **55**: 1766-1771 [PMID: 25342384 DOI: 10.2967/jnumed.114.145490]
- 57 **Wang J**, Wang H, Liu A, Fang C, Hao J, Wang Z. Lactate dehydrogenase A negatively regulated by miRNAs promotes aerobic glycolysis and is increased in colorectal cancer. *Oncotarget* 2015; **6**: 19456-19468 [PMID: 26062441 DOI: 10.18632/oncotarget.3318]
- 58 **Deng SM**, Zhang W, Zhang B, Chen YY, Li JH, Wu YW. Correlation between the Uptake of 18F-Fluorodeoxyglucose (18F-FDG) and the Expression of Proliferation-Associated Antigen Ki-67 in Cancer Patients: A Meta-Analysis. *PLoS One* 2015; **10**: e0129028 [PMID: 26038827 DOI: 10.1371/journal.pone.0129028]
- 59 **Ostrem JM**, Peters U, Sos ML, Wells JA, Shokat KM. K-Ras(G12C) inhibitors allosterically control GTP affinity and effector interactions. *Nature* 2013; **503**: 548-551 [PMID: 24256730 DOI: 10.1038/nature12796]

P- Reviewer: Chen K, Palumbo B S- Editor: Kong JX L- Editor: A  
E- Editor: Lu YJ



## Retrospective Study

## CO<sub>2</sub>BOLD assessment of moyamoya syndrome: Validation with single photon emission computed tomography and positron emission tomography imaging

Alain Pellaton, Philippe Bijlenga, Laurie Bouchez, Victor Cuvinciuc, Isabelle Barnaure, Valentina Garibotto, Karl-Olof Lövblad, Sven Haller

Alain Pellaton, Laurie Bouchez, Victor Cuvinciuc, Isabelle Barnaure, Karl-Olof Lövblad, Sven Haller, Diagnostic and Interventional Neuroradiology, Geneva University Hospitals, 1211 Geneva, Switzerland

Philippe Bijlenga, Neurosurgery, Geneva University Hospitals, 1211 Geneva, Switzerland

Valentina Garibotto, Nuclear Medicine, Geneva University Hospitals, 1211 Geneva, Switzerland

**Author contributions:** Pellaton A contributed to data acquisition, data analysis, manuscript preparation; Bijlenga P contributed to patient selection, biostatistics, manuscript preparation; Bouchez L contributed to manuscript preparation; Cuvinciuc V and Barnaure I contributed to data analysis; Garibotto V contributed to data analysis, manuscript preparation; Lövblad KO contributed to manuscript preparation; Haller S contributed to data acquisition, biostatistics, manuscript preparation.

**Supported by** The Swiss National Science Foundation grant, No. 140340.

**Institutional review board statement:** We declare that the current study has been approved by the University of Geneva Ethical Committee and has therefore been performed in accordance with the ethical standards laid down in the 1964 Declaration of Helsinki and its later amendments.

**Informed consent statement:** Individual patient consent was waived by the local ethical committee for this retrospective study.

**Conflict-of-interest statement:** No conflicts of interest.

**Open-Access:** This article is an open-access article which was selected by an in-house editor and fully peer-reviewed by external reviewers. It is distributed in accordance with the Creative Commons Attribution Non Commercial (CC BY-NC 4.0) license, which permits others to distribute, remix, adapt, build upon this work non-commercially, and license their derivative works on

different terms, provided the original work is properly cited and the use is non-commercial. See: <http://creativecommons.org/licenses/by-nc/4.0/>

**Manuscript source:** Invited manuscript

**Correspondence to:** Karl-Olof Lövblad, MD, Diagnostic and Interventional Neuroradiology, Geneva University Hospitals, 4 rue Gabrielle-Perret Gentil, 1211 Geneva, Switzerland. [karl-olof.lovblad@hcuge.ch](mailto:karl-olof.lovblad@hcuge.ch)  
Telephone: +41-22-3727045  
Fax: +41-22-3727072

**Received:** April 21, 2016

**Peer-review started:** April 22, 2016

**First decision:** July 5, 2016

**Revised:** September 5, 2016

**Accepted:** September 21, 2016

**Article in press:** September 22, 2016

**Published online:** November 28, 2016

### Abstract

#### AIM

To compare the assessment of cerebrovascular reserve (CVR) using CO<sub>2</sub>BOLD magnetic resonance imaging (MRI) vs positron emission tomography (PET) and single photon emission computed tomography (SPECT) as reference standard.

#### METHODS

Ten consecutive patients (8 women, mean age of 41 ± 26 years) with moyamoya syndrome underwent 14 pre-surgical evaluations for external-internal carotid artery bypass surgery. CVR was assessed using CO<sub>2</sub>BOLD and PET (4)/SPECT (11) with a maximum interval of 36 d, and

evaluated by two experienced neuroradiologists.

## RESULTS

The inter-rater agreement was 0.81 for SPECT (excellent), 0.43 for PET (fair) and 0.7 for CO<sub>2</sub>BOLD (good). In 9/14 cases, there was a correspondence between CO<sub>2</sub>BOLD and PET/SPECT. In 4/14 cases, CVR was over-estimated in CO<sub>2</sub>BOLD, while in 1/14 case, CVR was underestimated in CO<sub>2</sub>BOLD. The sensitivity of CO<sub>2</sub>BOLD was 86% and a specificity of 43%.

## CONCLUSION

CO<sub>2</sub>BOLD can be used for pre-surgical assessment of CVR in patients with moyamoya syndrome and combines the advantages of absent irradiation, high availability of MRI and assessment of brain parenchyma, cerebral vessels and surrogate CVR in one stop.

**Key words:** Moyamoya; Vascular reserve; CO<sub>2</sub>BOLD; Cerebrovascular reserve

© The Author(s) 2016. Published by Baishideng Publishing Group Inc. All rights reserved.

**Core tip:** Inter-rater agreement of cerebrovascular reserve (CVR) assessment in CO<sub>2</sub>BOLD is similar to positron emission tomography (PET)/single photon emission computed tomography (SPECT); CO<sub>2</sub>BOLD has a sensitivity of 86% and specificity of 43% compared to PET/SPECT; Overall, CO<sub>2</sub>BOLD tends to over-estimate reduction in CVR compared to PET and SPECT as reference standard; Taking this over-estimation of CO<sub>2</sub>BOLD into account would further improve its sensitivity and specificity; CVR can be assessed using CO<sub>2</sub>BOLD for pre-surgical evaluation and follow-up of moyamoya syndrome patients.

Pellaton A, Bijlenga P, Bouchez L, Cuvinciu V, Barnaure I, Garibotto V, Lövblad KO, Haller S. CO<sub>2</sub>BOLD assessment of moyamoya syndrome: Validation with single photon emission computed tomography and positron emission tomography imaging. *World J Radiol* 2016; 8(11): 887-894 Available from: URL: <http://www.wjgnet.com/1949-8470/full/v8/i11/887.htm> DOI: <http://dx.doi.org/10.4329/wjr.v8.i11.887>

## INTRODUCTION

The term "moyamoya" means puff of smoke and describes the formation of collateral vessels due to high-grade stenosis of the distal internal carotid and proximal middle cerebral arteries. There are two related forms of the disease. Moyamoya disease is typically symmetric, genetically determined, prevalent notably in Japan and symptomatic at early stages in most cases<sup>[1]</sup>. In contrast, moyamoya syndrome or pattern is typically asymmetric, caused by a variety of underlying etiologies, more common in European countries with a prevalence of 3/1000000 and usually symptomatic only at later stages of the disease<sup>[2,3]</sup>. Extracranial-intracranial (EC-

IC) bypass is the most important surgical intervention, notably to prevent subsequent ischemic events and secondary hemorrhage<sup>[2,4]</sup>. The challenge in the follow-up of patients with moyamoya syndrome is the selection of the optimal time-point for the surgical intervention of the EC-IC bypass, as the benefit of prevention of stroke or hemorrhage contrasts the risk of peri-surgical complications of this difficult intervention.

The assessment of the cerebrovascular reserve (CVR) was previously proposed as one option to define the optimal timing for a surgical intervention<sup>[4-7]</sup>. Nuclear medicine, notably positron emission tomography (PET) and single photon emission computed tomography (SPECT) based methods, are the established techniques for the assessment of CVR. Disadvantages of these techniques are the radiation exposure, notably during several longitudinal follow-up investigations in moyamoya syndrome patients, the relatively limited availability and high costs compared to magnetic resonance imaging (MRI). Moreover, PET or SPECT imaging does not allow for the assessment of the brain parenchyma to evaluate acute or old vascular lesions, nor the assessment of the vessels to evaluate the progression of the vascular stenosis. The assessment of CVR in MRI would therefore provide a one-stop imaging solution assessing brain structure, vessels and CVR in a widely available and radiation free technique.

The current investigation tests whether carbon dioxide (CO<sub>2</sub>) blood oxygenation level dependent (BOLD) MRI may be used for the pre-surgical assessment of surrogate CVR in moyamoya patients. In principle, the inhalation of CO<sub>2</sub> induces a vasodilation and as a consequence a BOLD response, which can be measured by dedicated MRI sequences as known from functional MRI<sup>[8]</sup>. CO<sub>2</sub>-BOLD was demonstrated to be safe and feasible in clinical neuroimaging<sup>[9]</sup> and provided interesting results for example in the assessment of patients with proximal internal carotid artery stenosis both before and after intervention<sup>[10,11]</sup> as well as for the evaluation of surrogate CVR in adult and pediatric moyamoya<sup>[12-17]</sup>. Note that CVR is historically defined as CBF increase following a vasodilator challenge. In contrast, the change in the BOLD signal following the CO<sub>2</sub> stimulation includes contributions from CBF, cerebral blood volume, and oxygenation changes, and is thus more complex than simple CBF change. Consequently, CO<sub>2</sub> induced BOLD change is not equal to CVR as classically defined, yet correlated as demonstrated previously<sup>[18]</sup>. We therefore use the term "surrogate" CVR in the context of CO<sub>2</sub>BOLD.

In particular, we directly compared surrogate CVR assessment based on CO<sub>2</sub>BOLD MRI using a simple nasal cannula setup vs PET/SPECT as reference standard in ten consecutive patients with moyamoya syndrome undergoing pre-surgical evaluation for EC-IC bypass.

## MATERIALS AND METHODS

### Participants

This retrospective study was approved by the local

**Table 1** Essential demographic and clinical data of the included patients

No	Age	Gender	Diagnosis	Etiology	Treatment	PET	SPECT	BOLD
1	53	F	Bilateral moyamoya	Unknown	Bypass	0	1	1
2	41	F	Bilateral moyamoya	Unknown	Bypass	1	2	3
3	26	F	Left moyamoya	Unknown	Bypass	1	1	1
4	15	F	Right moyamoya	Unknown	Conservative	0	1	1
5	42	F	Bilateral moyamoya	Unknown	Bilateral bypass	0	1	1
6	39	F	Bilateral moyamoya	Unknown	Bypass	2	0	2
7	51	M	Right moyamoya	Dissection	Bypass	0	1	1
8	42	F	Right moyamoya	Unknown	Bypass	0	2	2
9	46	M	Bilateral moyamoya	Unknown	Conservative	0	1	1
10	58	F	Bilateral moyamoya	Stenosis	Bypass	0	1	1
Mean age	41.3				Total	4	11	14

PET: Positron emission tomography; SPECT: Single photon emission computed tomography; F: Female; M: Male.

ethical committee and includes ten consecutive patients (8 women and 2 men with a mean age of  $41 \pm 26$  years, see Table 1) with moyamoya syndrome undergoing 14 pre-surgical evaluations for EC-IC bypass between November 2010 and August 2014. All patients underwent pre-surgical evaluation for moyamoya syndrome with SPECT and/or PET as part of their clinical routine workup as well as MRI. For these 14 pre-surgical evaluations, we compared the CO<sub>2</sub>BOLD to the SPECT and/or PET assessments of the corresponding time point, and the maximum delay between PET/SPECT and CO<sub>2</sub>BOLD MRI was 36 d. Two cases had both SPECT and PET, but only in one case PET and SPECT were performed at the same time point. For this case, we compared the CO<sub>2</sub>BOLD the consensus of PET and SPECT.

### MRI

Imaging data were acquired on a clinical routine whole body 3T MR scanner (MAGNETOM Trio, Siemens Healthcare, Erlangen, Germany).

We deliberately chose a very simple CO<sub>2</sub> challenge, which was equivalent to previous investigations<sup>[11,19]</sup>. In essence, the CO<sub>2</sub> challenge consisted of a 9 min block-design of 1 min OFF, 2 min ON, 2 min OFF, 2 min ON, 2 min OFF (Figure 1). During the ON periods, a ready-to-use mix of 7% CO<sub>2</sub> with synthetic air (in a gas bottle outside the MR scanner room) was applied using a simple nasal cannula which was connected using a simple silicone tube. The MR technician manually started and stopped the CO<sub>2</sub> application at 8 L/min using a standard clinical flow meter. During the OFF periods, participant inhaled normal room air. Data acquisition consisted in a standard echo echo-planar imaging (EPI) covering the entire brain with the following parameters: 74 × 74 matrix, 45 slices, voxel size 2.97 mm × 2.97 mm × 3.0 mm, TE of 30 ms, TR 3000 ms, 180 repetitions.

A structural 3DT1 sequence was collected for spatial normalization (256 × 256 matrix, 176 slices, 1 mm × 1 mm × 1 mm, TE 2.3 ms, TR 2300 ms). Additional sequences (axial SE T2w and GRE T2\*, diffusion tensor imaging DTI with 30 directions, fluid attenuated inversion recovery FLAIR) were acquired and analyzed to rule out concomitant disease such as ischemic stroke, subdural

hematomas and susceptibility artifacts from prior hemorrhage or space-occupying lesions.

### PET imaging

PET imaging was performed during routine clinical assessment using the following parameters: Quantitative images were created after two intravenous injections of about 800 MBq of <sup>15</sup>O-H<sub>2</sub> separated by at least 90 min. The injection of acetazolamide was made 20 min before the second acquisition. For patients weighing more than 60 kg, 1 g was intravenously administered, for others the dose was reduced proportionally. The acquisition was performed on a standard high-resolution PET scanner with trans-axial images of the brain reconstructed using filtered back-projection (128 × 128 matrix, 35 slices, 2.34 mm × 2.34 mm × 4.25 mm voxel size) on non-decay-corrected data. Parametric images were obtained following a previously published approach<sup>[13]</sup>. CVR maps are generated by comparison of pre- and post-acetazolamide images.

### SPECT imaging

SPECT imaging was performed during routine clinical assessment using the following parameters (known as "split-dose" protocol): "Baseline images" were acquired 20 min after the intravenous injection of 300 MBq of <sup>99m</sup>Tc-HMPAO. Subsequently, 1000 mg of acetazolamide were administered (slow infusion over 5 min) under blood pressure and heart rate monitoring. Twenty minutes later, a second dose of 600 MBq of <sup>99m</sup>Tc-HMPAO was injected and "acetazolamide images" were acquired 20 min after administration. The 2 acquisitions are made on a triple head gamma-camera (Toshiba Medical Systems Corporation), equipped with fan beam, low-energy, high-resolution collimators. Sixty projection over 360 degrees were acquired. Filtered back projection reconstruction was done using a 128 × 128 matrix and applying a uniform Chang attenuation correction. Equivalent to PET, CVR maps are generated by comparison of pre- and post-acetazolamide images.

### CO<sub>2</sub>BOLD data post-processing

The CO<sub>2</sub>BOLD data were processed with the free FSL

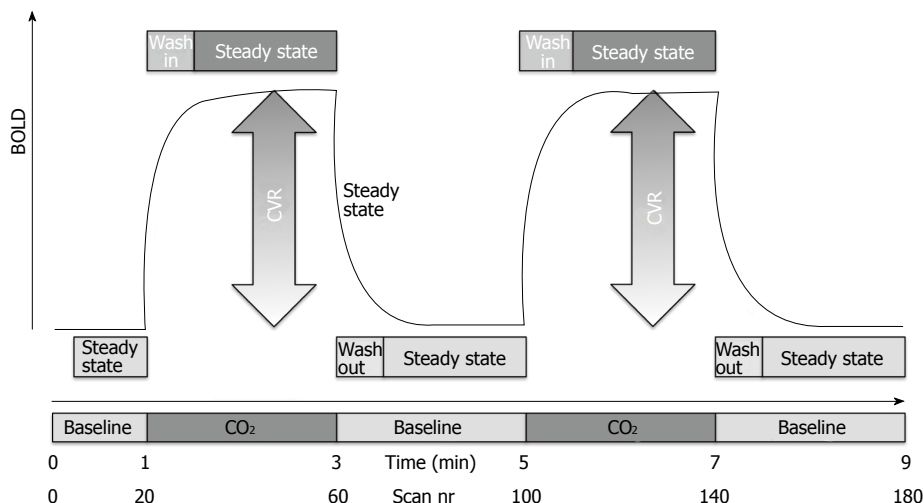


**Figure 1** Schematic representation of the ON-OFF CO<sub>2</sub> challenge of 7% CO<sub>2</sub> applied via a simple nasal cannula. The magnitude of the CO<sub>2</sub> induced change in the blood oxygenation level dependent (BOLD) response represents the cerebrovascular reserve (CVR).

software (FMRIB Software Library, version 5.0.2.1; www.fmrib.ox.ac.uk/fsl). The essential processing steps include motion correction, spatial smoothing (10 mm filter size) and masking of non-brain voxels using brain extraction tool (BET, part of FSL). We then calculated parametric maps of the SURROGATE CVT response using an adapted ON-OFF regressor, which was convolved with a square basic shape corresponding to the ON-OFF CO<sub>2</sub> inhalation. This schematic curvature was modified with a Gaussian convolution where the sigma factor was change. We calculated the maps with different models of sigma curvature to take into account delayed vascular response due to the proximal vascular stenosis. The delay was varied as 30, 45, 60, 75, 90 and 120 s to model variable speed of the CO<sub>2</sub> induced BOLD response (Figure 2). Both readers had all 6 maps available for the comparison between BOLD and PET/SPECT and reported that they preferentially used the 90 and 120 maps because the other maps were less informative.

**Visual analysis**

The visual analysis of the surrogate CVT maps derived from CO<sub>2</sub>BOLD MRI, PET and SPECT images was independently performed by two neuroradiologists (Figure 3 for an example case) and the ratings were considered as independent points. All cases and all imaging modalities were independently evaluated in four vascular territories: Left/right anterior cerebral artery (ACA) and left/right middle cerebral artery (MCA) territory based on a three point rating system: 0 = no reduction in CVR, 1 = mild reduction in CVR, 2 = severe reduction in CVR.

**Statistical analysis**

In a first step, we calculated the inter-rater agreement between both raters separately for CO<sub>2</sub>BOLD, SPECT and PET using Cohen’s kappa statistics with quadratic weighting.

In a second step, we binarized the results in order

to calculate sensitivity and specificity values of CVR for the comparison of CO<sub>2</sub>BOLD vs PET/SPECT. This analysis was done within the clinical context, *i.e.*, the presence of at least one territory with a substantial reduction of CVR is considered as indication for a treatment. This means that the CVR for both PET/SPECT or CO<sub>2</sub>BOLD was considered “reduced” when at least one vascular territory had a significant reduction of CVR, for example substantial reduction in left MCA and mild reduction in left ACA territory. Conversely, the CVR was considered as normal when no territory had a substantial reduction of CVR, for example mild reduction in both left ACA and MCA territories. Based on this classification, we calculated sensitivity, specificity, positive predictive value, negative predictive value and accuracy.

**RESULTS**

**Inter-rater agreement**

The inter-rater agreement was 0.81 for SPECT (excellent), 0.43 for PET (fair) and 0.7 for CO<sub>2</sub>BOLD (good).

**Correspondence of CVR between CO<sub>2</sub>BOLD and PET/SPECT**

The correspondence of CVR assessment between CO<sub>2</sub>BOLD and PET/SPECT is illustrated in Table 2. In 9/14 cases, there was a correspondence between CO<sub>2</sub>BOLD and PET/SPECT. In 4/14 cases, Surrogate CVT was significantly reduced in CO<sub>2</sub>BOLD but not in PET/SPECT, while in 1/14 case surrogate CVT was significantly reduced in PET/SPECT but not in CO<sub>2</sub>BOLD. Consequently, CO<sub>2</sub>BOLD tends to over-estimate the reduction in surrogate CVR compared to PET/SPECT. The sensitivity of CO<sub>2</sub>BOLD was 86% and a specificity of 43%.

**DISCUSSION**

The assessment of surrogate CVR using CO<sub>2</sub>BOLD and

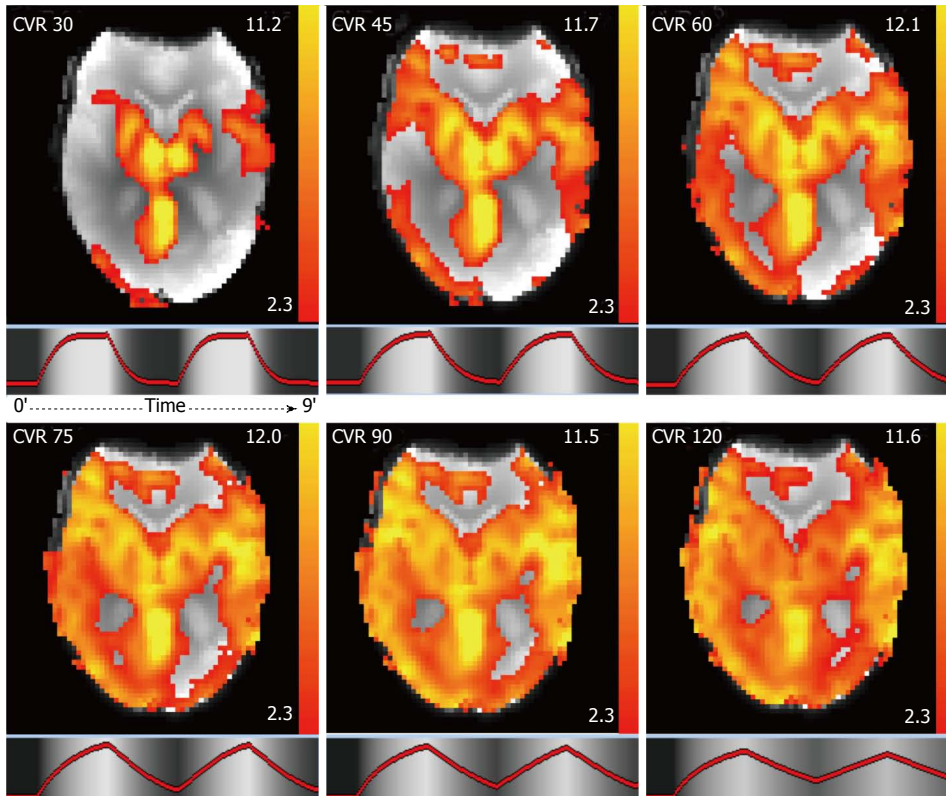


**Figure 2** CO<sub>2</sub>BOLD cerebrovascular reserve maps in axial view. To take into account delayed vascular response due to the proximal vascular stenosis, the delay of the CO<sub>2</sub> induced BOLD response was varied from 30, 45, 60, 75, 90 to 120 s. Units = Z value. CVR: Cerebrovascular reserve.

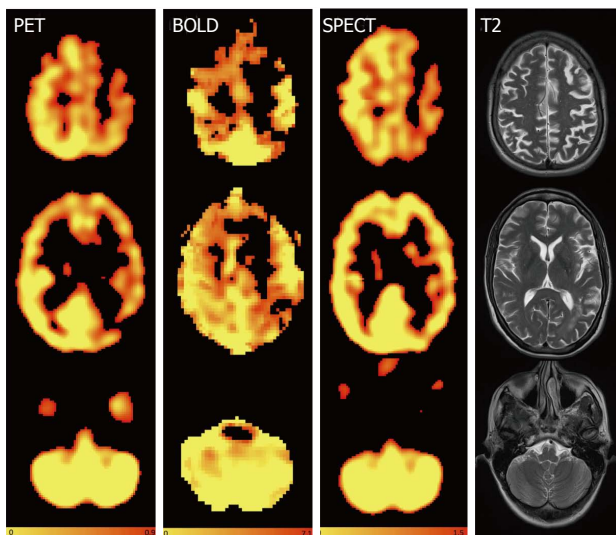


**Figure 3** Axial images of a sample patient showing reduced cerebrovascular reserve on the left hemispheric anterior cerebral artery and middle cerebral artery territories without any diminution of the cerebrovascular reserve in the cerebellum for positron emission tomography, CO<sub>2</sub>BOLD and single photon emission computed tomography and axial T2. The readings for the territories right ACM, right anterior cerebral artery (ACA), left ACM and left ACA were 0 (normal), 0, 2 (substantial reduction), 2 for reader A and 1, 0, 2, 2 for reader B for PET, 0, 1, 2, 2 and 1, 0, 2, 2 for CO<sub>2</sub>BOLD and 1, 1, 2, 2 and 1, 1, 2, 2 for SPECT. 0 = no reduction in CVR, 1 = mild reduction in CVR, 2 = severe reduction in CVR Color-scales represent: PET: Normalized accumulated activity, dimensionless under the assumption that 1 mL of tissue weights 1 g. BOLD: Statistical Z value, SPECT: Relative counts, normalized to the mean counts in the cerebellum, dimensionless. PET: Positron emission tomography; SPECT: Single photon emission computed tomography; BOLD: Blood oxygenation level dependent.

a simple nasal cannula approach in MRI in the pre-surgical evaluation and follow-up of moyamoya patients combines the advantages of: (1) absent irradiation notably in the context of serial follow-up; (2) minimal experimental setup; (3) high patient comfort; and (4) the simultaneous assessment of brain parenchyma (acute/old vascular lesions), vessels (progression of vascular stenosis) and CVR in only one imaging session.

The assessment of surrogate CVR in CO<sub>2</sub>BOLD compared to the reference standard PET/SPECT provided a good sensitivity of 86% yet a relatively low specificity of 43%. The relatively high sensitivity is of particular interest in the clinical context of pre-surgical evaluation of CVR. CO<sub>2</sub>BOLD could therefore be used as a screening modality for reduction of surrogate CVR in the pre-surgical evaluation and follow-up of moyamoya patients, and in case of a pathologic result of CO<sub>2</sub>BOLD the reference standard techniques PET or SPECT could be performed in a second step. Moreover, our results show that CO<sub>2</sub>BOLD tends to over-estimate the reduction of surrogate CVR with respect to the reference standard techniques PET or SPECT. Taking this knowledge into account during the interpretation of the CO<sub>2</sub>BOLD CVR maps could therefore further improve the sensitivity and specificity of this technique in the future. Moreover, as the CO<sub>2</sub>BOLD challenge includes contributions from CBF, cerebral blood volume, and oxygenation changes, and is thus more complex than simple CBF change assessed in PET or SPECT.

**Table 2** Concordance between CO<sub>2</sub>BOLD and positron emission tomography/single photon emission computed tomography

	PET/SPECT pathologic	PET/SPECT normal	
CO <sub>2</sub> BOLD pathologic	6 TP 43%	4 FP 29%	PPV 60%
CO <sub>2</sub> BOLD normal	1 FN 7%	3 TN 21%	NPV 75%
	SENS 86%	SPEC 43%	ACC 64%

TP: True positive; TN: True negative; FP: False positive; FN: False negative; SENS: Sensitivity; SPEC: Specificity; PPV: Positive predictive value; NPV: Negative predictive value; ACC: Accuracy; PET: Positron emission tomography; SPECT: Single photon emission computed tomography.

Future direct comparisons of CO<sub>2</sub>BOLD vs PET or SPECT, ideally in a larger sample size or model, might assess the differences between CO<sub>2</sub>BOLD surrogate CVR and PET/SPECT CVR in more detail. The inter-rater reliability of CO<sub>2</sub>BOLD is in the range of the reference techniques PET and SPECT.

A few previous investigations already successfully CVR in moyamoya patients based on BOLD imaging. Heyn *et al.*<sup>[12]</sup> investigated 11 patients with moyamoya using a tight-fitting facemask demonstrated good correlated of CVR maps with conventional angiography disease stage. Mandell *et al.*<sup>[13]</sup> investigated CVR based on BOLD in several vascular diseases including 12 patients with moyamoya again using a tight facemask with a rebreathing bag and found good correlation with arterial spin labeling (ASL). A follow-up study by the same group demonstrated that preoperative CO<sub>2</sub>BOLD CVR predicts the hemodynamic effect of ECIC bypass using the same computer-controlled gas blender and a tight facemask<sup>[17]</sup>. The BOLD technique may also be used to assess treatment effect in pre- vs post-operative moyamoya disease<sup>[14]</sup>. Han *et al.*<sup>[15]</sup> used a computer-driven gas blender and a tight facemask in thirteen pediatric moyamoya patients and were able to reliably derive CVR maps. The advantage of tight facemasks and gas blenders is not only the more accurate delivery of the CO<sub>2</sub> stimulus, but also the possibility of assessment of the end tidal CO<sub>2</sub> concentration for quantification. An alternative approach for the assessment of CVR is the breath-hold technique<sup>[20]</sup>. Thomas *et al.*<sup>[16]</sup> used a breath-hold challenge in eight consecutive pediatric moyamoya patients and found that while all breath-hold challenge during general anesthesia resulted in best quality CVR maps, only 42% of studies without general anesthesia yielded best quality CVR maps. Finally, a previous study Shiino *et al.*<sup>[18]</sup> validated CO<sub>2</sub>BOLD CVR against acetazolamide SPECT CVR in 17 healthy subjects and 10 patients with severe ICA steno-occlusive disease, including 2 patients with moyamoya disease. In summary, these previous results indicate that CVR maps can reliably be assessed using tight facemasks while a simple breath-hold technique might not be sufficient to obtain high-quality CVR maps in all patients. With

respect to these previous investigations, the current study differs in two main aspects. First, we used a very simple nasal cannula for CO<sub>2</sub> stimulation to obtain a simple experimental setup which does not interfere with the other MR imaging sequences yet still allows reliable CVR map generation. While this approach evidently is not as accurate as the use of a computer-driven gas blender and a tight facemask, we consider this as a clinically acceptable compromise to obtain CVR maps with a simple and widely applicable setup, which does not interfere with patient comfort during the acquisition of the other MRI sequences. Second, we directly compare the surrogate CVR maps to PET/SPECT as references standard.

An alternative approach for the assessment of CVR in MRI is an acetazolamide challenge during ASL imaging, which was successfully applied in several recent investigations<sup>[21-25]</sup>. The advantage of ASL is the estimation of semi-quantitative relative cerebral blood flow (relCBF) maps. However, the intravenous injection of acetazolamide is more invasive than the inhalation of CO<sub>2</sub> via a nasal cannula in setup of the current CO<sub>2</sub>BOLD study. Advantages of CO<sub>2</sub>BOLD are the in general higher signal to noise ratio. Moreover, one BOLD sequence with ON-OFF CO<sub>2</sub> challenge is enough, while ASL usually requires two sequences before and after intravenous acetazolamide injection, and a delay between injection and image acquisition results in an overall longer exam time. Moreover, transit delay may interfere with ASL imaging notably in the context of significant vascular stenosis in moyamoya. Future head-to-head comparison of CO<sub>2</sub>BOLD vs acetazolamide ASL are required to determine which MRI technique has the better test performance.

### Limitations

One of the major limitations of the current investigation is the limited sample size of ten patients with 14 pre-surgical follow-up investigations. This sample size should however be considered in light of the very low prevalence of moyamoya syndrome of 3/1000000 in European countries<sup>[3]</sup>. Consequently, the previous related studies discussed above include 8<sup>[16]</sup>, 11<sup>[12]</sup>, 12<sup>[13]</sup> and 13 pediatric<sup>[15]</sup> patients with moyamoya. It is also important to note that the vasodilation induced by acetazolamide is stronger than the vasodilation induced by the inhalation of CO<sub>2</sub> via a simple nasal cannula. Another factor, which can be discussed, is the application of the CO<sub>2</sub> via a simple nasal cannula instead of the alternative approach of a tight face-mask that separates in-flow and out-flow. Such a tight face-mask allows for a much more precise application and monitoring of the applied CO<sub>2</sub> concentration, however at the cost of a significantly more complex experimental setup, reduced patient comfort during the entire scanning also including anatomic MR sequences and usually increased motion artifacts. As discussed in detail before<sup>[11,19]</sup>, such systems are undoubtedly more precise and appropriate

notably for research settings. For example, as we cannot precisely estimate the degree of hypercapnia achieved by the CO<sub>2</sub> challenge, which can vary from scan to scan, the current simple nasal cannula technique may not normalized CVR maps with respect to hypercapnia to reduce inter-scan variability during serial follow-up. However, the minimal experimental setup and patient comfort are in our opinion of paramount importance for potential widespread clinical applications of CO<sub>2</sub>BOLD CVR imaging and arguments in favor of the simple nasal cannula setup. As described above, the CVR assessment based on CO<sub>2</sub>BOLD was validated already in 2003<sup>[18]</sup> yet did not make the transition into widespread clinical use and instead remains limited to very few academic centers. This is probably at least in part due to fact that most previous studies use expensive and complicated computer-controlled gas blenders and tight facemasks reducing patient comfort. We deliberately take into account shortcomings with respect to the precision of CO<sub>2</sub> application and monitoring using the nasal cannula approach, yet still obtained a CVR map of diagnostic quality in all cases. This approach was already successfully applied to study patients with vascular stenosis of the internal carotid artery<sup>[11]</sup>.

The CO<sub>2</sub>BOLD technique using a simple nasal cannula approach can be used for pre-surgical assessment of surrogate CVR in patients with moyamoya syndrome and combines the advantages of absent irradiation, patient comfort, simple experimental setup, high availability of MRI and assessment of brain parenchyma, cerebral vessels and surrogate CVR in one stop.

## COMMENTS

### Background

Moyamoya disease may cause stroke due to a reduction in cerebral blood flow. In order to decide when and if an intervention is needed, it is necessary to assess the capacity of the brain to respond.

### Research frontiers

It is important to develop new MR based techniques to replace the currently performed nuclear medicine techniques such as positron emission tomography (PET) and single photon emission computed tomography (SPECT).

### Innovations and breakthroughs

The authors find that MR perfusion with COBOLD technique can reliably investigate cerebrovascular reserve (CVR).

### Applications

The use of MR based COBOLD will allow to easily test the CVR inpatients with moyamoya and other diseases.

### Peer-review

This is a useful study for assessing the patients with moyamoya disease.

## REFERENCES

1 **Wakai K**, Tamakoshi A, Ikezaki K, Fukui M, Kawamura T, Aoki R, Kojima M, Lin Y, Ohno Y. Epidemiological features of moyamoya disease in Japan: findings from a nationwide survey. *Clin Neurol Neurosurg* 1997; **99** Suppl 2: S1-S5 [PMID: 9409395]

2 **Scott RM**, Smith ER. Moyamoya disease and moyamoya syndrome. *N Engl J Med* 2009; **360**: 1226-1237 [PMID: 19297575 DOI: 10.1056/NEJMra0804622]

3 **Yonekawa Y**, Ogata N, Kaku Y, Taub E, Imhof HG. Moyamoya disease in Europe, past and present status. *Clin Neurol Neurosurg* 1997; **99** Suppl 2: S58-S60 [PMID: 9409407]

4 **Mesiwala AH**, Sviri G, Fatemi N, Britz GW, Newell DW. Long-term outcome of superficial temporal artery-middle cerebral artery bypass for patients with moyamoya disease in the US. *Neurosurg Focus* 2008; **24**: E15 [PMID: 18275291 DOI: 10.3171/FOC/2008/24/2/E15]

5 **Conklin J**, Fierstra J, Crawley AP, Han JS, Poublanc J, Mandell DM, Silver FL, Tymianski M, Fisher JA, Mikulis DJ. Impaired cerebrovascular reactivity with steal phenomenon is associated with increased diffusion in white matter of patients with Moyamoya disease. *Stroke* 2010; **41**: 1610-1616 [PMID: 20576954 DOI: 10.1161/STROKEAHA.110.579540]

6 **Kang KH**, Kim HS, Kim SY. Quantitative cerebrovascular reserve measured by acetazolamide-challenged dynamic CT perfusion in ischemic adult Moyamoya disease: initial experience with angiographic correlation. *AJNR Am J Neuroradiol* 2008; **29**: 1487-1493 [PMID: 18499785 DOI: 10.3174/ajnr.A1129]

7 **Schubert GA**, Weinmann C, Seiz M, Gerigk L, Weiss C, Horn P, Thomé C. Cerebrovascular insufficiency as the criterion for revascularization procedures in selected patients: a correlation study of xenon contrast-enhanced CT and PWI. *Neurosurg Rev* 2009; **32**: 29-35; discussion 35-36 [PMID: 18791753 DOI: 10.1007/s10143-008-0159-z]

8 **Cohen ER**, Ugurbil K, Kim SG. Effect of basal conditions on the magnitude and dynamics of the blood oxygenation level-dependent fMRI response. *J Cereb Blood Flow Metab* 2002; **22**: 1042-1053 [PMID: 12218410]

9 **Spano VR**, Mandell DM, Poublanc J, Sam K, Battisti-Charbonney A, Pucci O, Han JS, Crawley AP, Fisher JA, Mikulis DJ. CO<sub>2</sub> blood oxygen level-dependent MR mapping of cerebrovascular reserve in a clinical population: safety, tolerability, and technical feasibility. *Radiology* 2013; **266**: 592-598 [PMID: 23204541 DOI: 10.1148/radiol.12112795]

10 **Ziyeh S**, Rick J, Reinhard M, Hetzel A, Mader I, Speck O. Blood oxygen level-dependent MRI of cerebral CO<sub>2</sub> reactivity in severe carotid stenosis and occlusion. *Stroke* 2005; **36**: 751-756 [PMID: 15705935 DOI: 10.1161/01.STR.0000157593.03470.3d]

11 **Haller S**, Bonati LH, Rick J, Klarhöfer M, Speck O, Lyrer PA, Bilecen D, Engelter ST, Wetzel SG. Reduced cerebrovascular reserve at CO<sub>2</sub> BOLD MR imaging is associated with increased risk of periinterventional ischemic lesions during carotid endarterectomy or stent placement: preliminary results. *Radiology* 2008; **249**: 251-258 [PMID: 18796680 DOI: 10.1148/radiol.2491071644]

12 **Heyn C**, Poublanc J, Crawley A, Mandell D, Han JS, Tymianski M, terBrugge K, Fisher JA, Mikulis DJ. Quantification of cerebrovascular reactivity by blood oxygen level-dependent MR imaging and correlation with conventional angiography in patients with Moyamoya disease. *AJNR Am J Neuroradiol* 2010; **31**: 862-867 [PMID: 20075092 DOI: 10.3174/ajnr.A1922]

13 **Mandell DM**, Han JS, Poublanc J, Crawley AP, Stainsby JA, Fisher JA, Mikulis DJ. Mapping cerebrovascular reactivity using blood oxygen level-dependent MRI in Patients with arterial stenocclusive disease: comparison with arterial spin labeling MRI. *Stroke* 2008; **39**: 2021-2028 [PMID: 18451352 DOI: 10.1161/STROKEAHA.107.506709]

14 **Mikulis DJ**, Krolczyk G, Desal H, Logan W, Deveber G, Dirks P, Tymianski M, Crawley A, Vesely A, Kassner A, Preiss D, Somogyi R, Fisher JA. Preoperative and postoperative mapping of cerebrovascular reactivity in moyamoya disease by using blood oxygen level-dependent magnetic resonance imaging. *J Neurosurg* 2005; **103**: 347-355 [PMID: 16175867 DOI: 10.3171/jns.2005.103.2.0347]

15 **Han JS**, Mikulis DJ, Mardimae A, Kassner A, Poublanc J, Crawley AP, deVeber GA, Fisher JA, Logan WJ. Measurement of cerebrovascular reactivity in pediatric patients with cerebral vasculopathy using blood oxygen level-dependent MRI. *Stroke* 2011; **42**: 1261-1269 [PMID: 21493907 DOI: 10.1161/STROKEAHA.110.603225]

- 16 **Thomas B**, Logan W, Donner EJ, Shroff M. Assessment of cerebrovascular reactivity using real-time BOLD fMRI in children with moyamoya disease: a pilot study. *Childs Nerv Syst* 2013; **29**: 457-463 [PMID: 23132694 DOI: 10.1007/s00381-012-1952-0]
- 17 **Mandell DM**, Han JS, Poublanc J, Crawley AP, Fierstra J, Tymianski M, Fisher JA, Mikulis DJ. Quantitative measurement of cerebrovascular reactivity by blood oxygen level-dependent MR imaging in patients with intracranial stenosis: preoperative cerebrovascular reactivity predicts the effect of extracranial-intracranial bypass surgery. *AJNR Am J Neuroradiol* 2011; **32**: 721-727 [PMID: 21436343 DOI: 10.3174/ajnr.A2365]
- 18 **Shiino A**, Morita Y, Tsuji A, Maeda K, Ito R, Furukawa A, Matsuda M, Inubushi T. Estimation of cerebral perfusion reserve by blood oxygenation level-dependent imaging: comparison with single-photon emission computed tomography. *J Cereb Blood Flow Metab* 2003; **23**: 121-135 [PMID: 12500097]
- 19 **Richiardi J**, Monsch AU, Haas T, Barkhof F, Van de Ville D, Radu EW, Kressig RW, Haller S. Altered cerebrovascular reactivity velocity in mild cognitive impairment and Alzheimer's disease. *Neurobiol Aging* 2015; **36**: 33-41 [PMID: 25146454 DOI: 10.1016/j.neurobiolaging.2014.07.020]
- 20 **Pillai JJ**, Mikulis DJ. Cerebrovascular reactivity mapping: an evolving standard for clinical functional imaging. *AJNR Am J Neuroradiol* 2015; **36**: 7-13 [PMID: 24788129 DOI: 10.3174/ajnr.A3941]
- 21 **Goetti R**, O'Gorman R, Khan N, Kellenberger CJ, Scheer I. Arterial spin labelling MRI for assessment of cerebral perfusion in children with moyamoya disease: comparison with dynamic susceptibility contrast MRI. *Neuroradiology* 2013; **55**: 639-647 [PMID: 23404242 DOI: 10.1007/s00234-013-1155-8]
- 22 **Noguchi T**, Kawashima M, Irie H, Ootsuka T, Nishihara M, Matsushima T, Kudo S. Arterial spin-labeling MR imaging in moyamoya disease compared with SPECT imaging. *Eur J Radiol* 2011; **80**: e557-e562 [PMID: 21315533 DOI: 10.1016/j.ejrad.2011.01.016]
- 23 **Saida T**, Masumoto T, Nakai Y, Shiigai M, Matsumura A, Minami M. Moyamoya disease: evaluation of postoperative revascularization using multiphase selective arterial spin labeling MRI. *J Comput Assist Tomogr* 2012; **36**: 143-149 [PMID: 22261785 DOI: 10.1097/RCT.0b013e31824150dd]
- 24 **Sugino T**, Mikami T, Miyata K, Suzuki K, Houkin K, Mikuni N. Arterial spin-labeling magnetic resonance imaging after revascularization of moyamoya disease. *J Stroke Cerebrovasc Dis* 2013; **22**: 811-816 [PMID: 22721824 DOI: 10.1016/j.jstrokecerebrovasdis.2012.05.010]
- 25 **Zaharchuk G**, Do HM, Marks MP, Rosenberg J, Moseley ME, Steinberg GK. Arterial spin-labeling MRI can identify the presence and intensity of collateral perfusion in patients with moyamoya disease. *Stroke* 2011; **42**: 2485-2491 [PMID: 21799169 DOI: 10.1161/STROKEAHA.111.616466]

P- Reviewer: Li YZ S- Editor: Ji FF L- Editor: A  
E- Editor: Lu YJ



## Retrospective Study

**Radiological imaging findings of scheuermann disease**

Erkan Gokce, Murat Beyhan

Erkan Gokce, Department of Radiology, School of Medicine, Gaziosmanpaşa University, 60100 Tokat, Turkey

Murat Beyhan, Department of Radiology, Tokat State Hospital, 60100 Tokat, Turkey

**Author contributions:** Gokce E and Beyhan M collected and analyzed the data equally; Gokce E designed, supervised and statistical analysis the study; Gokce E and Beyhan M had taken part in literature research and manuscript preparation and had read and approved the final version.

**Institutional review board statement:** This study was reviewed and approved by the Ethics Committee of the Gaziosmanpaşa University School of Medicine (No: 15-KAEK-156).

**Informed consent statement:** Patients were not required to give informed consent to the study because the analysis of figures used picture archiving and communication system.

**Conflict-of-interest statement:** We have no financial relationships to disclose.

**Data sharing statement:** No additional data are available.

**Open-Access:** This article is an open-access article which was selected by an in-house editor and fully peer-reviewed by external reviewers. It is distributed in accordance with the Creative Commons Attribution Non Commercial (CC BY-NC 4.0) license, which permits others to distribute, remix, adapt, build upon this work non-commercially, and license their derivative works on different terms, provided the original work is properly cited and the use is non-commercial. See: <http://creativecommons.org/licenses/by-nc/4.0/>

**Manuscript source:** Invited manuscript

**Correspondence to:** Erkan Gokce, MD, Associate Professor, Department of Radiology, School of Medicine, Gaziosmanpaşa University, Kaleardi Quarter, Muhittin Fisunoglu Street, 60100 Tokat, Turkey. [erkangokce@mynet.com](mailto:erkangokce@mynet.com)  
Telephone: +90-542-3798986  
Fax: +90-362-2309105

Received: June 8, 2016

Peer-review started: June 13, 2016

First decision: July 11, 2016

Revised: July 23, 2016

Accepted: September 6, 2016

Article in press: September 8, 2016

Published online: November 28, 2016

**Abstract****AIM**

To find accompanying anomalies of typical and atypical Scheuermann's disease (SD) is reported in the present study.

**METHODS**

Study included 20 patients (16 men and 4 women) who had radiological imaging radiography, magnetic resonance imaging (MRI) and computed tomography, if available, due to back pain, curved back and low back pain in November 2011-February 2016 period. Patients were categorized into typical and atypical patterns based on the region involved. Thoracic kyphosis values were measured using real Cobb angle. Accompanying disc degeneration, herniations and spinal cord pathologies were studied using MRI.

**RESULTS**

Age of the patients ranged from 11.0 to 23.0 (mean  $17.2 \pm 3.0$ ). Typical pattern of SD were detected in 15 patients while atypical pattern were detected in 5 patients. Cobb angle range was 40.2-67.2 (mean  $55.5 \pm 8.7$ ) in typical Scheuermann's patients and 24.7-49.9 (mean  $36.7 \pm 10.8$ ) in atypical ones. Intervertebral level was affected and had the measures of 3-8 (mean  $5.3 \pm 1.6$ ) and 7-9 (mean  $8.2 \pm 0.8$ ) in typical and atypical Scheuermann's patients, respectively. Level of degenerative disc disease in MRI was 1-7 discs (mean  $4.1 \pm 1.7$ ) in typical patients and 5-10 discs (mean  $7.6 \pm 1.9$ ) in atypical patients.

**CONCLUSION**

SD can be seen in typical and atypical patterns, typical being more frequent. Because degenerative disc diseases,

herniations and cord pathologies such as syringomyelia can accompany SD (albeit more common in atypical pattern), it is necessary to evaluate these patients with plain radiography and MRI together.

**Key words:** Cobb angle; Magnetic resonance imaging; Juvenile kyphosis; Scheuermann's disease; Thoracic kyphosis

© **The Author(s) 2016.** Published by Baishideng Publishing Group Inc. All rights reserved.

**Core tip:** Scheuermann's disease (SD) is the most common cause of degenerative structural thoracic or thoracolumbar hyperkyphosis associated with back pain in adolescents and could be observed in typical and atypical patterns. It manifests itself with successive endplate irregularities and anterior vertebral wedging in radiography, and additionally as disc degenerations, herniations and syringomyelia in spinal cord in magnetic resonance imaging (MRI). Impairment in intervertebral distance and disc degeneration are more evident in SD with atypical pattern. When multiple endplate irregularities and anterior vertebral wedging are observed in MRI of patients thought to have thoracolumbar disc pathology, SD should be considered.

Gokce E, Beyhan M. Radiological imaging findings of scheuermann disease. *World J Radiol* 2016; 8(11): 895-901 Available from: URL: <http://www.wjgnet.com/1949-8470/full/v8/i11/895.htm> DOI: <http://dx.doi.org/10.4329/wjr.v8.i11.895>

## INTRODUCTION

Scheuermann's disease (SD) or juvenile kyphosis is the most common cause of progressive, structural thoracic or thoracolumbar hyperkyphosis associated with back pain in adolescents. It has a prevalence of 0.4%-8.0%<sup>[1-3]</sup>. Typical patients are 13-16 years old. Progression is slow in most cases<sup>[1-5]</sup>. Reports about their morbidity frequencies in different genders are varied<sup>[1,5,6]</sup>. In terms of radiological examinations, some authors consider the presence of wedging in at least three successive vertebra at an angle of over 5° as diagnosis criterion for SD<sup>[1]</sup>, while others<sup>[7]</sup> consider wedging in a vertebra along with irregular endplates enough as diagnosis criterion<sup>[8]</sup>. Radiological findings of SD are reported in the present study.

## MATERIALS AND METHODS

The present retrospective study included 20 patients (16 male and 4 female) who had radiological imaging taken at Radiology Department of Gaziosmanpaşa University Medical School due to back pain, curved back and low back pain complaints in November 2011-February 2016 period. After taking the approval of local ethic committee



Figure 1 Illustration of Cobb angle in lateral radiography (Patient no: 17). Cobb angle: 55.3°.

(No. 15-KAEK-156), radiological images of the patients were obtained from Picture Archiving and Communication System (PACS, GE). All patients had direct radiographies and eight of them had cervical, thoracic and lumbar magnetic resonance imaging (MRI), seven had thoracic MRI, two of which were contrasted, three had thoracic and lumbar MRI, one had cervical and lumbar MRI and one had thoracic MRI and lumbar CT. Based on Sørensen's definition in radiological examinations, wedging over an angle of 5° in three or more vertebrae, kyphosis over 40° in sagittal plane and irregularities in vertebra endplates were considered typical SD<sup>[1]</sup>. Level of thoracic curve was determined based on measurement of Cobb angle (real Cobb angle is the angle between upper and plate of the most curved vertebra at the top and lower endplates of the most curved vertebra at the bottom) (Figure 1). The cases with thoracic involvement only (including T12-L1 level) were considered typical, whereas ones with thoracolumbar or lumbar involvement were considered atypical. Level where the apex of kyphosis was exactly located was examined. MRI was used to study accompanying degenerative disc disease, herniations and spinal cord pathologies (syringomyelia, etc.). Signal reduction of more than 50% in T2 series of intervertebral discs in MRI was considered in favor of degenerative disc disease.

### Statistical analysis

The statistics were reviewed and analyzed by an author of this article. Descriptive analyses were made to gain information about general features of working groups. Data regarding continuous variable were given as mean ( $\pm$ ) SD but data regarding categorical variables were given as  $n$  (%). Statistical software was used in statistical analyses (IBM PASW Statistics 18, SPSS Inc., IBM Co., Somers, NY).

## RESULTS

Age of the patients ranged from 11.0 to 23.0 (mean 17.2  $\pm$  3.0). Typical pattern of SD were detected in 15 patients while atypical pattern were detected in 5

**Table 1** Demographic features, Scheuermann's disease patterns, involved intervertebral levels and their numbers, Cobb angle values, level of degenerative disc disease and accompanying magnetic resonance imaging findings of patients

Patient	Type	Gender	Age	Symptoms	No. of affected levels	Involved levels	Cobb Angle	Disc degeneration levels	Accompanying findings
1	T	Male	16	Back pain	3	T9-T12	44.1	T9-T12	T11-T12 diffuse bulging
2	T	Male	16	Low back pain	5	T7-T12	40.2	T7-T12	thoracic scoliosis
3	A	Male	18	Low back pain	9	T9-S1	49.9	T7-8,T9-S1	Bulging at all levels of lumbar spine
4	T	Male	17	Low back pain	5	T7-T12	63	T7-T11	Diffused bulging in T6-7, 8-9, 9-10, 11-12
5	T	Male	20	Curved back, low back pain	7	T5-T12	66.2	T5-T12	Bulging in T7-12, increase in lumbar lordosis
6	A	Male	14	Curved back	9	T5-L2	42.3	T5-L2	Thoracic syringomyelia, thoracic levoscoliosis, diffuse bulging in T11-T12
7	T	Male	23	Back pain	8	T5-L1	60.1	T5-T10 and T12-L1	Bulging in T5-6, T7-T10; syringomyelia from T2 to L1, lumbar levoscoliosis
8	T	Male	19	Low back pain	6	T7-L1	52	T7-T11 and T12-L1	Bulging in T8-9 and T10-11
9	T	Male	17	Back pain	6	T6-T12	61.7	T6-T12	Bulging in T10-11, L4-S1, syringomyelia at thoracic T9-10
10	T	Male	17	Curved back, kyphosis	7	T6-L1	62.1	T7-8 single level	Paramedian bulging in T7-8
11	T	Male	17	Scoliosis	7	T6-L1	55	None	None
12	T	Female	11	Kyphosis	4	T5-T9	67.2	T5-6, 7-8, 8-9, 11-12	Posterocentral protrusion in T11-12
13	A	Male	16	Low back pain	7	T7-L2	40.6	T4-5, T7-L1	Posterocentral protrusion in T4-5, syringomyelia at T3-T5 levels
14	T	Female	23	Back pain	3	T7-T10	50.5	T7-T10	Multiple bulging
15	A	Male	20	Low back pain	8	T7-L3	26.3	T3-4, 6-7-8-9, 11-12	Bulging in T7-8; Posterocentral protrusion in T8-9, 11-12
16	A	Male	14	Low back pain	8	T10-S1	24.7	T10-L5	None
17	T	Female	14	Low back pain, scoliosis	5	T6-T11	55.3	T6-9, L1-2	Diffused bulging in T12-L1, L1-L2
18	T	Male	16	Low back pain	4	T5-T9	43.3	T5-9	Posterocentral bulging in T9-10
19	T	Female	20	Back pain, scoliosis	3	T7-10	63.3	T7-10	Lumbar levoscoliosis
20	T	Female	16	Low back pain, scoliosis	7	T5-T12	48.5	T7-9	Posterior bulging in T7-8, T8-9

patients. Cobb angle varied from 24.7 to 67.2 (mean  $50.8 \pm 12.7$ ) in all patient population, while typical cases had Cobb angles from 40.2 to 67.2 (mean  $55.5 \pm 8.7$ ) and atypical ones from 24.7 to 49.9 (mean  $36.7 \pm 10.8$ ). Number of affected intervertebral levels in whole patient group varied from three to nine. In typical SD cases, range of affected levels was 3-8 (mean  $5.3 \pm 1.6$ ) and in atypical ones 7-9 (mean  $8.2 \pm 0.8$ ). Degenerative disc disease was at 1-7 level in typical SD cases (mean  $4.1 \pm 1.7$ ) and 5-10 (mean  $7.6 \pm 1.9$ ) in atypical ones. Demographic features of the patients, involvement levels and numbers, Cobb angles, degenerative disc disease and accompanying MRI findings were given in Table 1. Radiological images of SD patients with typical pattern were given in Figures 2-5, and those of SD patients with atypical pattern were given in Figures 6-10.

## DISCUSSION

SD has been defined by Holger Werfel Scheuermann, a radiologist, in 1920 and has also been known as osteochondritis juvenile dorsi or kyphosis dorsalis juvenilis<sup>[4,9]</sup>. In SD, which leads to rigid kyphosis of vertebra, lower thoracic and upper lumbar regions are affected. It could involve a few vertebra segments or the whole vertebra<sup>[4]</sup>. Two patterns have been defined in SD based on affected area of vertebra<sup>[10]</sup>. In more

typical pattern, thoracic region is frequently affected and is characterized by thoracic kyphosis increase and wedging in vertebra corpus. This pattern is accompanied by nonstructural hyperlordosis of cervical and lumbar spine<sup>[4,6,10]</sup>. SD of atypical pattern (thoracolumbar or lumbar) has been defined later and is distinguished from typical one by lack of thoracic kyphosis and evident wedging in corpus of vertebrae<sup>[11]</sup> which is considered to be more progressive in adulthood<sup>[6,10,12,13]</sup>. Apex of the kyphosis is lowered at the thoracolumbar junction (T11-T12) in atypical pattern of disease<sup>[8,12]</sup>. Such pathologies account for 25% to 80% of SD<sup>[8]</sup>. In the present study, 75% of the cases were of typical pattern and 25 were atypical. No cervical form of SD has been described so far, which could be due to immobile nature of uncus during puberty and thus could prevent vertebral endplate from mechanical stress<sup>[8]</sup>. SD of cervical form was not observed in the present study.

Thoracic kyphosis normally varies between 20 and 45° based on measurement by Cobb method on a standing lateral radiograph in which arms are kept in a position 60° below the horizontal<sup>[6,14]</sup>. Kyphosis normally progresses by age, and women have slightly higher kyphosis than men<sup>[6,14]</sup>. Thoracic kyphosis increase is one of the diagnostic criteria of typical SD<sup>[11]</sup>. In the present study, average value of thoracic kyphosis was 55.5° (range 40.2°-67.2°) in SD patients of typical pattern and it was

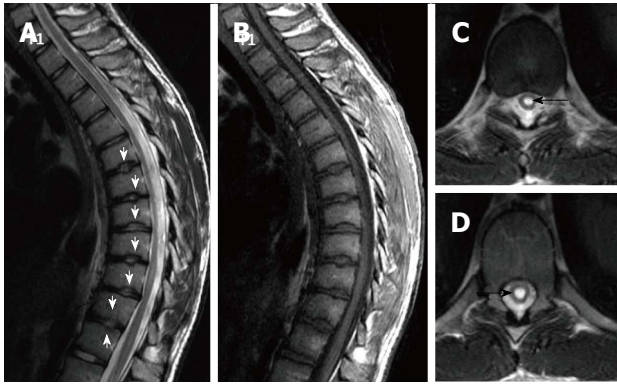


**Figure 2** Seventeen years old patient with typical Scheuermann's disease (Patient no: 9). Sagittal plane (A) T2 weighted (B) T1 weighted (C and D) axial plane T2 weighted magnetic resonance imaging A and B: Kyphosis with apex facing to T9 vertebra (Cobb angle 61.7°), irregularities more evident in central part of T6-T12 endplates (white arrows) and disc degeneration are shown at these levels; C and D: Syrinx in medulla spinalis at thoracic 9-10 levels (black arrows).

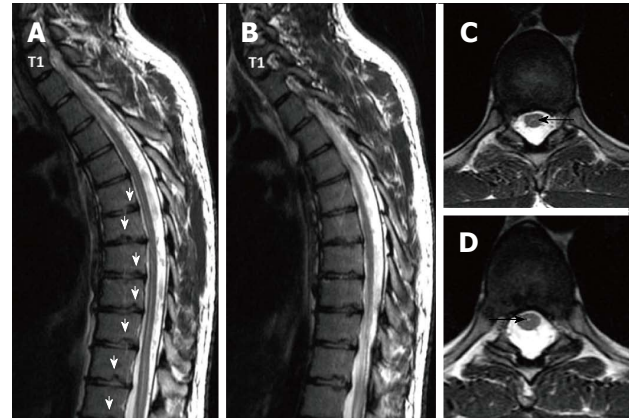


**Figure 5** Twenty three years old male patient with typical Scheuermann's disease (Patient no: 7). (A and B) Thoracic sagittal plane (C and D) axial plane T2 weighted magnetic resonance imaging. A and B: Irregularities in endplates (white arrows), degenerations in discs slight syringomyelia in spinal cords are shown; C and D: Hyperintensity due to syrinx (black arrows) in spinal cord and diffused bulging are shown.

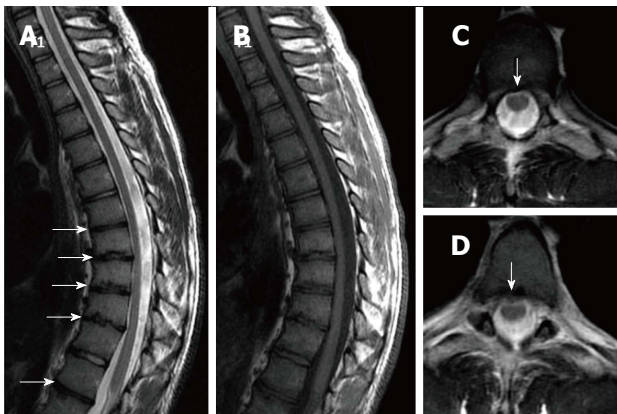


**Figure 3** Nineteen years old male patient with typical Scheuermann's disease (Patient no: 8). Sagittal plane (A) T2 weighted (B) T1 weighted (C and D) axial plane T2 weighted magnetic resonance imaging A and B: Kyphosis with apex facing to T9, irregularities in T7-L1 endplates and disc degeneration at these levels (except for T11-12) (white arrows) are shown; C and D: Bulging is demonstrated at thoracic 8-9 and 10-11 levels (white arrows).

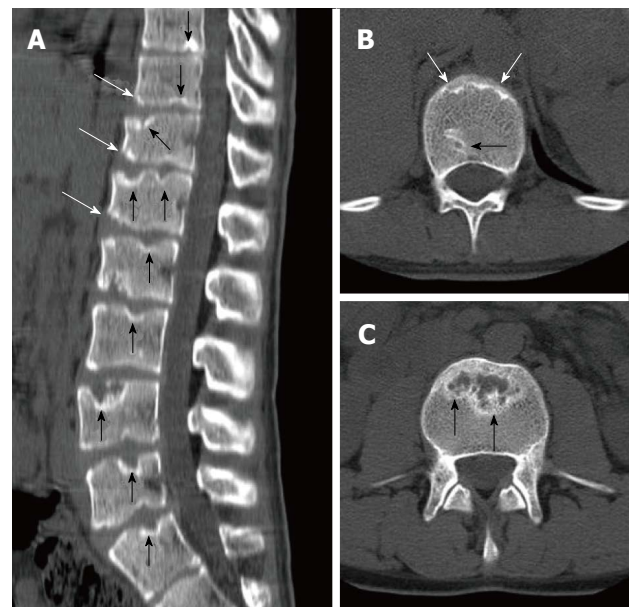


**Figure 6** Eighteen years old male patient with atypical Scheuermann's disease (Patient no: 3). (A) Sagittal reformatted (B and C) axial plane computerized tomography. A: Evident irregularities and Schmorl nodules in thoracic, lumbar and sacral endplate surfaces (black arrows), anterior wedging in vertebra corpuses (white arrows) are shown; B and C: Endplate irregularities in axial plane CT images (white arrows) and Schmorl nodules (black arrows) are shown.

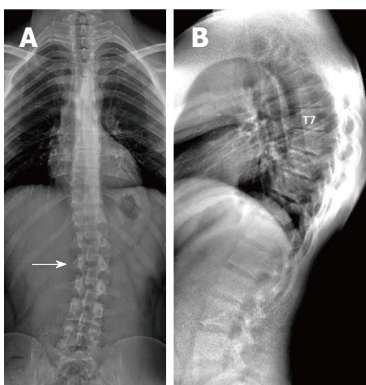


**Figure 4** Twenty-three years old male patient with typical Scheuermann's disease (Patient no: 7). A: A scoliosis radiography demonstrating scoliosis with opening facing to right (white arrow) in lumbar axis; B: Lateral radiography of kyphosis with apex facing to T7 vertebra in thoracic spinal axis (Cobb angle 60.1°) and irregularities in thoracic endplates are shown.

elevated. Average thoracic kyphosis value in SD patients of atypical pattern, on the other hand, was 36.7° and were within normal limits except for one patient who had elevated level (49.9°). Tyrakowski *et al*<sup>[10]</sup> reported that apex of kyphosis was between T6 and T9 in SD patients of typical pattern while between T10 and L2 levels in patients of atypical pattern. Similar to the findings of Tyrakowski *et al*<sup>[10]</sup>, apices of kyphosis in SD patients with typical pattern were between T6 and T9 in the present study. However, unlike their results, apices of kyphosis in

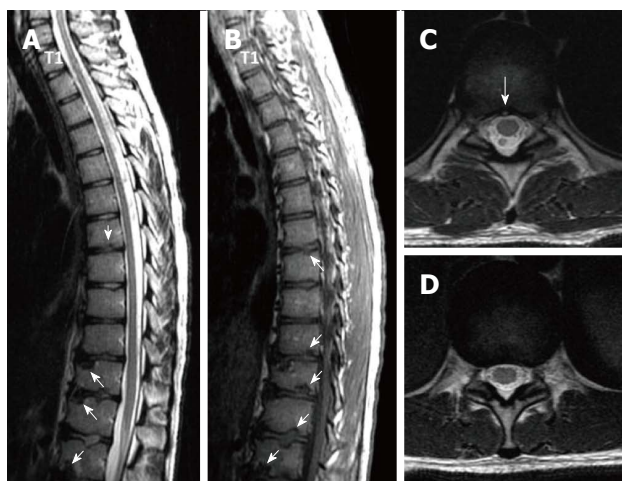


**Figure 7** Eighteen years old male patient with atypical Scheuermann's disease (Patient no: 3). Sagittal plane (A) T2 weighted (B) T1 weighted (C and D) axial plane T2 weighted magnetic resonance imaging A and B: Thoracic 7-8, T9-L2 endplate irregularities, Schmorl nodules (white arrows) and degeneration signals in discs are shown; C and D: Posterior central protrusion (white arrow) and diffused bulging are shown.

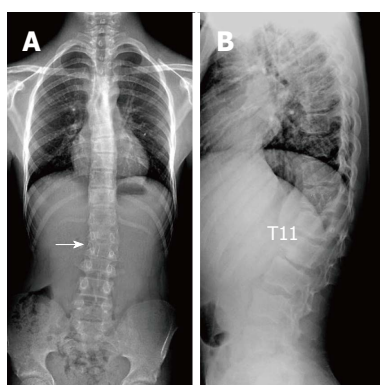


**Figure 8** Fourteen years old male patient with atypical Scheuermann's disease (Patient no: 6). A: Slight scoliosis with opening facing towards right in lumbar axis is shown in a scoliosis radiography (white arrow); B: Kyphosis with apex facing towards T11 level, and successive thoracic and lumbar endplate irregularities are demonstrated in a lateral radiography.

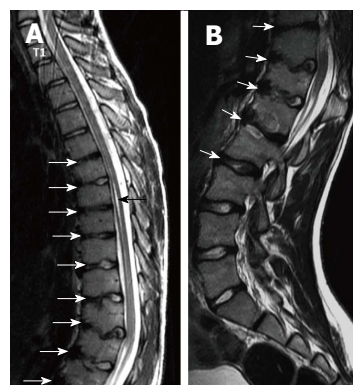


**Figure 9** Fourteen years old male patient with atypical Scheuermann's disease (Patient no: 6). (A) Thoracic (B) lumbar sagittal plane T2 weighted magnetic resonance imaging A: Elevated kyphosis at lower thoracic level, endplate irregularities and disc degenerations starting at T5 level (white arrows) and syringomyelia on thoracic spinal cord (black arrow) are demonstrated; B: Evident degenerative irregularities and disc degenerations (white arrows) in lower thoracic and upper lumbar endplates are shown.

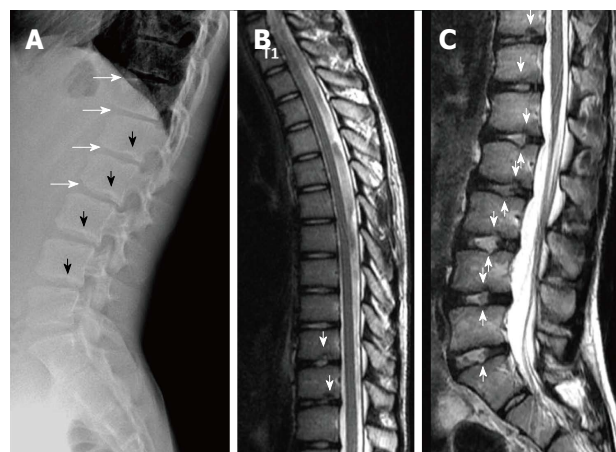


**Figure 10** Fourteen years old male patient with atypical Scheuermann's disease (Patient no: 16). (A) Lateral radiography (B) Thoracic and (C) Lumbar sagittal plane T2 weighted magnetic resonance imaging. A: Anterior wedging in corposes of lower thoracic and upper lumbar vertebrae (white arrows), and lower thoracic and lumbar endplate irregularities (black arrows) are shown; B and C: Lower thoracic and lumbar endplate irregularities (white arrows) and disc degenerations are demonstrated.

SD patients of atypical pattern were between T9 and L1 levels. In typical pattern SD cases in the present study, it was found that three to eight involvement were detected between T5 (inferior endplate) and L1 vertebra (superior endplate). SD cases of atypical pattern, on the other hand, had endplate involvements varying from seven to nine levels between T5 (inferior endplate) and S1 (superior endplate) of vertebra. Therefore, although our population was relatively small, it could be stated that a higher number of levels in a larger interval are affected in SD patients with atypical pattern compared to the ones with typical pattern.

Most SD patients get diagnosis towards the end of juvenile stage, around 8-12 years of age, when the disease has already caused more rigid and severe deformities depending upon age<sup>[15]</sup>. In our patient population, the youngest age of presentation was 11 and the oldest was 23 years. Despite the presence of some

studies reporting that prevalence of SD is about the same in both genders, there are also studies reporting higher incidence in males<sup>[1,5,6,16]</sup>. In the present study, male patients constituted the majority of the cases (80%).

Etiology of SD still remains largely unknown. Among the several theories proposed are elevated levels of growth hormone release, impaired collagen fibril formation and, as a consequence, weakening in vertebral endplates, juvenile osteoporosis, vitamin A deficiency, trauma, epiphysis and poliomyelitis<sup>[5,6,16,17]</sup>. Recent studies report major effects of genetic background for the disease<sup>[3,8,18,19]</sup>. Disorganized endochondral ossification, collagen decrease and mucopolisaccharide increase in vertebral endplates have been reported in histopathology of SD<sup>[6]</sup>. As secondary to these, intervertebral discs can be influenced due to low quality endplate development,

which could in turn pave the way for the degenerative disease<sup>[4,8]</sup>. SD frequently has a benign prognosis and can lead to small deformities and symptoms. Back pain and fatigue are the most common complaints during the development, which generally clears after skeletal maturity<sup>[6]</sup>. Disc impairment or inflammatory lesions of SD can cause pain especially at the apices of kyphosis. Muscular tension after long-term sitting or movement often induces lumbar pain. Lumbar pain may also be result of spine damage due to disc herniation or spondylolysis<sup>[4,8,20]</sup>. Deformities are usually noticed during school age. An increase can be seen in lumbar lordosis and cervical lordosis to offset the kyphosis occurred<sup>[4]</sup>. Treatment of patients with Scheuermann's kyphosis is decided based on the degree of kyphosis and maturity of the patient<sup>[4]</sup>. For patients with kyphosis between 55° and 80°, brace treatment is almost fully successful with diagnoses made before skeletal maturity. Symptomatic SD patients with kyphosis greater than 80° in the thoracic spine or 65° in the thoracolumbar spine cannot be treated successfully without surgery. Surgical treatment is needed in adolescents and young adults when there is deterioration, refractory pain, and loss of sagittal balance or neurologic involvement<sup>[6]</sup>. In adults, progressive kyphosis with pain has been reported to generally occur as a result of SD with thoracolumbar pattern rather than with thoracic pattern<sup>[6]</sup>. There are studies in the literature reporting increase in the prevalence of back pain in SD with classic thoracic pattern<sup>[5,21]</sup>. Ristolainen *et al.*<sup>[21]</sup> found that low back pain increased by 2.5-fold in SD patients compared to healthy controls. Similarly, Murray *et al.*<sup>[5]</sup> reported much higher frequency of thoracic back pain in SD patient population (28%) compared to healthy controls (3%). Both groups found no association between back pain and the degree or level of apex of kyphosis<sup>[5,21]</sup>.

Sørensen<sup>[1]</sup> described radiographic criteria for typical SD including anterior wedging greater than 5° in at least three adjacent vertebral bodies. Schmorl's nodes, irregularity and flattened vertebral endplates, narrowed intervertebral disc spaces and anteroposterior elongation of the apical vertebral bodies are other associated radiological features of SD. Blumenthal *et al.*<sup>[13]</sup>, on the other hand, described the criteria for atypical SD, including wedging in one or two vertebral bodies, changes in vertebral endplate, narrowed disc space and anterior Schmorl nodes. MRI features of atypical SD have been described by Heithoff *et al.*<sup>[11]</sup>, and they include narrowed disc space, disc dehydration, endplate irregularity, wedging in edges of anterior vertebral body and appearance of Schmorl nodes. The authors concluded that at least three of these criteria are needed to make SD diagnosis. Some studies reported associations between variations in SD types in vertebra and degenerative lumbar disease in younger patients<sup>[11,22,23]</sup>. In the study by Paaajanen *et al.*<sup>[22]</sup>, 55% of the SD patients had thoracolumbar disc disease based on MRI findings. The finding in the present study that 93.3% of SD patients with typical pattern (Figures 2, 3 and 5) and 100% of patients with atypical pattern (Figures 7, 9

and 10) had degenerative disc disease suggests that SD paves the way for degenerative changes.

Disc degeneration was observed at all levels affected by the disease with both typical and atypical patterns in the present study. In addition, other levels also had disc degeneration to some extent. It seems that compared to SD with typical pattern, SD with atypical pattern affects more levels and facilitates degenerative disc disease to a higher degree. This fact implies that in younger patients for whom thoracolumbar MRI is required for degenerative disc disease especially when endplate irregularities are detected in a number of successive levels, SD should be strongly considered in differential diagnosis.

About one third of SD patients have scoliosis at varying degrees. It is known that spondylolysis or spondylolisthesis are more frequent in SD patients, a fact which might account for their low back pain. Some degree of degenerative spondylosis is observed mainly in apex of kyphosis in adults and is the cause of most back pain in these patients<sup>[6,22]</sup>. In untreated Scheuermann's kyphosis, secondary complications such as neurological problems, dural cysts or thoracic disc herniation have been described though in limited number of patients<sup>[6,16,24,25]</sup>. In the present study, on the other hand, only a quarter of the patients had scoliosis (Figures 4 and 8) and none had spondylolysis or spondylolisthesis. MRI had been requested in 80% of our cases due to upper or lower back pain. Disc herniation (mostly bulging) was detected at levels ranging from 1 to 5 in 80% of cases. Average number of herniations was roughly the same in SD patients of typical and atypical pattern (2.4 ± 1.3 and 2.5 ± 1.9, respectively). No neurological complications secondary to herniations were detected in any patients.

The major limitations of the present study were limited number of cases studied retrospectively, unequal number of typical and atypical cases, relatively limited length of study, and use of only radiological evaluations.

In conclusion, SD could be seen in typical and atypical patterns. Since degenerative diseases accompany SD, especially atypical pattern, when irregularities are detected in successive endplates in patients for whom spinal MRI is requested for disc pathology pre-diagnoses, radiologists should consider SD.

## COMMENTS

### Background

Scheuermann's disease (SD) is a progressive disease associated with back pain or low back pain in adolescents. It is the most common cause of structural thoracic or thoracolumbar hyperkyphosis, and could be seen in typical or atypical patterns. Diagnosis of SD is made by radiological methods along with clinical findings. Magnetic resonance imaging (MRI), on the other hand, is useful to indicate accompanying disc and spinal cord pathologies. In the present study, radiological findings of typical and atypical pattern Scheuermann's patients were reported.

### Research frontiers

Since SD is frequently accompanied by degenerative disc diseases especially in atypical pattern, SD should be considered when successive endplate irregularities are observed in patients for whom spinal MRI is requested with disc pathology pre-diagnosis.

### Innovations and breakthroughs

The present study revealed that more intervertebral levels were affected in SD with atypical pattern compared to SD with typical pattern [7-9 (mean  $8.2 \pm 0.8$ ) and 3-8 (mean  $5.3 \pm 1.6$ ), respectively]. Similarly, degenerative disc disease also affected more levels in SD with atypical pattern [5-10 (mean  $7.6 \pm 1.9$ )] compared to SD with typical one [1-7 (mean  $4.1 \pm 1.7$ )].

### Applications

In addition to radiography findings, spinal pathologies such as discal degenerations, herniations and syringomyelia could be evaluated using MRI.

### Terminology

Typical SD: It is a progressive disease of unknown cause accompanied by juvenile dorsal kyphosis, and is characterized by successive endplate irregularities in thoracic vertebrae and anterior vertebral wedging; atypical SD: It is the pattern of SD lacking evident thoracic kyphosis and vertebral wedging, characterized by successive endplate irregularities in lower thoracic and lumbar vertebrae, Schmorl nodules and disc degeneration.

### Peer-review

This manuscript reported the imaging findings of patients having the Scheuermann's diseases. There are 20 patients in the study and both MRI and CT images were investigated. This is a serious work with detailed description.

## REFERENCES

- 1 **Sørensen KH.** Scheuermann's juvenile kyphosis: clinical appearances, radiography, etiology and prognosis. Copenhagen: Munksgaard, 1964
- 2 **Gavin TM.** The Etiology and Natural History of Scheuermann's Kyphosis. *Prost Orth* 2003; **15**: 11-14 [DOI: 10.1097/00008526-200310001-00003]
- 3 **Damborg F, Engell V, Andersen M, Kyvik KO, Thomsen K.** Prevalence, concordance, and heritability of Scheuermann kyphosis based on a study of twins. *J Bone Joint Surg Am* 2006; **88**: 2133-2136 [PMID: 17015588 DOI: 10.2106/JBJS.E.01302]
- 4 **Yaman O, Dalbayrak S.** Kyphosis and review of the literature. *Turk Neurosurg* 2014; **24**: 455-465 [PMID: 25050667 DOI: 10.5137/1019-5149.JTN.8940-13.0]
- 5 **Murray PM, Weinstein SL, Spratt KF.** The natural history and long-term follow-up of Scheuermann kyphosis. *J Bone Joint Surg Am* 1993; **75**: 236-248 [PMID: 8423184]
- 6 **Lowe TG.** Scheuermann's kyphosis. *Neurosurg Clin N Am* 2007; **18**: 305-315 [PMID: 17556132 DOI: 10.1016/j.nec.2007.02.011]
- 7 **Bradford DS.** Vertebral osteochondrosis (Scheuermann's kyphosis). *Clin Orthop Relat Res* 1981; **158**: 83-90 [PMID: 7273530]
- 8 **Palazzo C, Sailhan F, Revel M.** Scheuermann's disease: an update. *Joint Bone Spine* 2014; **81**: 209-214 [PMID: 24468666 DOI: 10.1016/j.jbspin.2013.11.012]
- 9 **Scheuermann HW.** Kyphosis dorsalis juvenilis. *Ugeskr Laeger* 1920; **82**: 385-393
- 10 **Tyrakowski M, Mardjetko S, Siemionow K.** Radiographic spinopelvic parameters in skeletally mature patients with Scheuermann disease. *Spine (Phila Pa 1976)* 2014; **39**: E1080-E1085 [PMID: 24921842 DOI: 10.1097/BRS.0000000000000460]
- 11 **Heithoff KB, Gundry CR, Burton CV, Winter RB.** Juvenile discogenic disease. *Spine (Phila Pa 1976)* 1994; **19**: 335-340 [PMID: 8171367 DOI: 10.1097/00007632-199402000-00014]
- 12 **Edgren W, Vainio S.** Osteochondrosis juvenilis lumbalis. *Acta Chir Scand Suppl* 1957; **227**: 1-47 [PMID: 13497500]
- 13 **Blumenthal SL, Roach J, Herring JA.** Lumbar Scheuermann's. A clinical series and classification. *Spine (Phila Pa 1976)* 1987; **12**: 929-932 [PMID: 3441839 DOI: 10.1097/00007632-198711000-00015]
- 14 **Fon GT, Pitt MJ, Thies AC.** Thoracic kyphosis: range in normal subjects. *AJR Am J Roentgenol* 1980; **134**: 979-983 [PMID: 6768276 DOI: 10.2214/ajr.134.5.979]
- 15 **Tomé-Bermejo F, Tzirikos AI.** [Current concepts on Scheuermann kyphosis: clinical presentation, diagnosis and controversies around treatment]. *Rev Esp Cir Ortop Traumatol* 2012; **56**: 491-505 [PMID: 23594948 DOI: 10.1016/j.recot.2012.07.002]
- 16 **Lowe TG, Line BG.** Evidence based medicine: analysis of Scheuermann kyphosis. *Spine (Phila Pa 1976)* 2007; **32**: S115-S119 [PMID: 17728677 DOI: 10.1097/BRS.0b013e3181354501]
- 17 **Fotiadis E, Kenanidis E, Samoladas E, Christodoulou A, Akritopoulos P, Akritopoulou K.** Scheuermann's disease: focus on weight and height role. *Eur Spine J* 2008; **17**: 673-678 [PMID: 18301929 DOI: 10.1007/s00586-008-0641-x]
- 18 **Damborg F, Engell V, Nielsen J, Kyvik KO, Andersen MØ, Thomsen K.** Genetic epidemiology of Scheuermann's disease. *Acta Orthop* 2011; **82**: 602-605 [PMID: 21895506 DOI: 10.3109/17453674.2011.618919]
- 19 **McKenzie L, Sillence D.** Familial Scheuermann disease: a genetic and linkage study. *J Med Genet* 1992; **29**: 41-45 [PMID: 1552543 DOI: 10.1136/jmg.29.1.41]
- 20 **Ogilvie JW, Sherman J.** Spondylolysis in Scheuermann's disease. *Spine (Phila Pa 1976)* 1987; **12**: 251-253 [PMID: 3589821 DOI: 10.1097/00007632-198704000-00010]
- 21 **Ristolainen L, Kettunen JA, Heliövaara M, Kujala UM, Heinonen A, Schlenzka D.** Untreated Scheuermann's disease: a 37-year follow-up study. *Eur Spine J* 2012; **21**: 819-824 [PMID: 22101868 DOI: 10.1007/s00586-011-2075-0]
- 22 **Paajanen H, Alanen A, Erkintalo M, Salminen JJ, Katevuo K.** Disc degeneration in Scheuermann disease. *Skeletal Radiol* 1989; **18**: 523-526 [PMID: 2588031 DOI: 10.1007/BF00351753]
- 23 **Tertti MO, Salminen JJ, Paajanen HE, Terho PH, Kormanen MJ.** Low-back pain and disk degeneration in children: a case-control MR imaging study. *Radiology* 1991; **180**: 503-507 [PMID: 1829844 DOI: 10.1148/radiology.180.2.1829844]
- 24 **Chiu KY, Luk KD.** Cord compression caused by multiple disc herniations and intraspinal cyst in Scheuermann's disease. *Spine (Phila Pa 1976)* 1995; **20**: 1075-1079 [PMID: 7631238 DOI: 10.1097/00007632-199505000-00016]
- 25 **Kapetanios GA, Hantzidis PT, Anagnostidis KS, Kirkos JM.** Thoracic cord compression caused by disk herniation in Scheuermann's disease: a case report and review of the literature. *Eur Spine J* 2006; **15** Suppl 5: 553-558 [PMID: 16421745 DOI: 10.1007/s00586-005-0053-0]

P- Reviewer: Chen F, Chow J, Shen J S- Editor: Qiu S

L- Editor: A E- Editor: Lu YJ





Published by **Baishideng Publishing Group Inc**

8226 Regency Drive, Pleasanton, CA 94588, USA

Telephone: +1-925-223-8242

Fax: +1-925-223-8243

E-mail: [bpgoffice@wjgnet.com](mailto:bpgoffice@wjgnet.com)

Help Desk: <http://www.wjgnet.com/esps/helpdesk.aspx>

<http://www.wjgnet.com>

